

# Why the Counterintuitive Phenomenon of Likelihood

## Rarely Appears in Tabular Anomaly Detection with Deep Generative Models?

Donghwan Kim<sup>1</sup> Junghun Phee<sup>2</sup> Hyunsoo Yoon<sup>1</sup>

### Abstract

Deep generative models with tractable and analytically computable likelihoods, exemplified by normalizing flows, offer an effective basis for anomaly detection through likelihood-based scoring. We demonstrate that, unlike in the image domain where deep generative models frequently assign higher likelihoods to anomalous data, such counterintuitive behavior occurs far less often in tabular settings. We first introduce a domain-agnostic formulation that enables consistent detection and evaluation of the counterintuitive phenomenon, addressing the absence of precise definition. Through extensive experiments on 47 tabular datasets and 10 CV/NLP embedding datasets in ADBench, benchmarked against 13 baseline models, we demonstrate that the phenomenon, as defined, is consistently rare in general tabular data. We further investigate this phenomenon from both theoretical and empirical perspectives, focusing on the roles of data dimensionality and difference in feature correlation. Our results suggest that likelihood-only detection with normalizing flows offers a practical and reliable approach for anomaly detection in tabular domains.

### 1. Introduction

Generative models, including variational autoencoders (VAEs) (Kingma & Welling, 2014), normalizing flows (NFs) (Dinh et al., 2015), and generative adversarial networks (GANs) (Goodfellow et al., 2014), are widely used to model complex data distributions across diverse applications such as industrial diagnostics, medical imaging, and financial risk assessment. Among these, normalizing flows are particularly well-suited for anomaly detection due to their ability to

<sup>1</sup>Department of Industrial Engineering, University of Yonsei, Republic of Korea, Seoul <sup>2</sup>H. Milton Stewart School of Industrial and Systems Engineering (ISyE), Georgia Institute of Technology, USA, GA. Correspondence to: Hyunsoo Yoon <hs.yoon@yonsei.ac.kr>.

Preprint. February 11, 2026.

compute estimated likelihoods, providing a straightforward mechanism for detecting out-of-distribution (OOD) samples.

<sup>1</sup> The simplest anomaly detection approach with normalizing flows is to assume that normal data  $\mathbf{x} \in \mathbb{R}^d$  follows the distribution  $P$  of normal data, and anomalous data  $\mathbf{x}' \in \mathbb{R}^d$  follows a distribution  $Q \neq P$ , and to determine that a given data  $\mathbf{x}_{\text{test}} \in \mathbb{R}^d$  is an anomaly if its likelihood  $\phi_P(\mathbf{x}_{\text{test}})$  is lower than a predefined threshold  $\alpha$  when tested. We refer to this method as NF-SLT (Normalizing Flow with Simple Likelihood Test).

This methodology is based on the intuition that anomalous data are less likely to be observed in the distribution of normal data. However, in the image domain, models such as normalizing flows often assign similar or even lower likelihoods to in-distribution data than to OOD data. In other words, data used for training can receive lower likelihoods than anomalous samples. Nalisnick et al. (2019a) demonstrate that when CIFAR-10 (Alex, 2009) is used as training data (In-distribution) and SVHN (Netzer et al., 2011) is used as the test data (Out-of-distribution) of a model that can obtain the likelihood of input data, SVHN has a higher likelihood than CIFAR-10. This is counterintuitive because the likelihood of OOD data is higher than that of in-distribution data. Therefore, it can be inferred that if anomaly detection is performed using only the likelihood of the input data, detection may fail in certain cases (i.e., occurrence of a counterintuitive phenomenon). Refer to Section 2.2 for more details about counterintuitive phenomenon.

However, the following question arises: does this phenomenon also occur in tabular data anomaly detection? Kirichenko et al. (2020) demonstrates that although the likelihood of in-distribution/OOD data overlaps for the normalizing flow in the tabular anomaly detection, it is limited by the fact that only two datasets are shown by setting each as in-distribution data/OOD data. In addition, there is no comparison with other tabular AD baseline models. A common argument is that assigning likelihoods higher than that of normal data to anomalies is sufficient to demonstrate a

<sup>1</sup>Although the two tasks slightly differ, we consider OOD detection and anomaly detection to be the same task, and we will utilize the term anomaly detection. Task definitions are presented in Appendix A.

counterintuitive phenomenon. Regardless, the interpretation has its limitations. First, the view is contradictory since the argument would consider any result outside 100% AUROC as counterintuitive. Second, likelihood inversion can arise from intrinsic dataset difficulty, for example, when normal and abnormal samples are hard to distinguish, rather than from the phenomenon itself.

This calls for a more sophisticated way to determine whether a counterintuitive phenomenon occurs, for example by comparing the generative model’s performance with that of other models (e.g., DeepSVDD, OCSVM), since simple approaches such as directly comparing the likelihoods of normal and abnormal data have inherent limitations. Hence, it remains unclear whether the counterintuitive likelihood phenomenon occurs in the tabular domain. To address this gap, we first propose a clearer definition of the currently vaguely defined counterintuitive phenomenon based on the observation in likelihood-based tests for models with estimated likelihoods, allowing the concept to be applied across different domains. Building on this definition, we conduct an extensive set of experiments to examine whether the simple likelihood test, previously criticized for its limitations in image anomaly detection, remains effective in the context of tabular anomaly detection. Consequently, we empirically demonstrate that almost all datasets in ADBench (Han et al., 2022), a tabular AD benchmark dataset, do not exhibit counterintuitive phenomena in the tabular domain, and even NF-SLT outperforms comparison models in simple likelihood tests. Furthermore, we demonstrate its success in the tabular domain theoretically and empirically from the perspective of dimensionality and feature correlation.

To explain why this counterintuitive phenomenon does not occur in the tabular domain, we use the following two facts:

**Fact 1.1** (Lower Dimension). *Images typically have three dimensions: height, width, and channel, while tabular data generally have lower dimensionality, consisting of a single feature vector without spatial structure.*

**Fact 1.2** (Correlation of Features). *Images exhibit strong local pixel correlations, which allows models like CNN to effectively capture spatial relationships between neighboring pixels. In contrast, tabular data does not assume any specific structural relationship between features.*

Taking ADBench as an example, most datasets have fewer than 100 features. However, CIFAR-10, one of the image datasets with small dimensions, has a dimension of 3072. This shows that the curse of dimensionality may be more severe in the image domain than in the tabular domain, and we analyze how this affects likelihood tests using normalizing flows. Additionally, Kirichenko et al. (2020) argued that in image OOD detection, normalizing flows fail to capture semantic information effectively because images exhibit local pixel correlations. Based on Fact 1.2, we extend this

discussion to the tabular domain and claim that normalizing flows are less affected by feature correlation in this setting. To justify this claim, we quantify overall feature correlation by measuring the reduction of intrinsic dimension (ID) relative to the ambient dimension. We then explain why this reduction reflects the effect of correlation, and compare the degree of ID reduction observed in tabular and image data. Although there are datasets in the tabular domain that have higher dimensions than images or strong correlation (e.g., genomics, see Appendix C.4), these have very different characteristics from typical tabular datasets, so it is reasonable to assume that the overall trends in the two domains are well represented by the examples above.

In conclusion, the contribution of our study can be described as threefold.

- We provide a **domain-agnostic definition of the counterintuitive phenomenon** in simple likelihood tests and empirically show that simple likelihood testing with normalizing flows in the tabular domain rarely leads to this phenomenon, outperforms comparison models.
- We verify our results using all **47 tabular datasets and 10 CV/NLP embedding datasets** from ADBench without selection bias (Shwartz-Ziv & Armon, 2022) and compare against 13 anomaly detection baselines.
- We provide a **theoretical and empirical analysis** of why the counterintuitive phenomenon does not occur in the tabular domain, unlike in images, by linking it to the difference in dimension and feature correlation.

## 2. Related Work

### 2.1. Normalizing Flow

Normalizing flow is one of the generative models that converts input data  $\mathbf{x} \in \mathbb{R}^d$ , which follows an unknown distribution with density  $p_{\mathbf{x}}$ , into  $\mathbf{z} \in \mathbb{R}^d$ ; in addition, it follows a simple distribution  $p_{\mathbf{z}}$  that is typically chosen as standard Gaussian  $\mathcal{N}(0, I_d)$  (Dinh et al., 2017), using an invertible function  $f: \mathbb{R}^d \rightarrow \mathbb{R}^d$  that consists of complex functions such as neural networks (Dinh et al., 2015), such that  $p_{\mathbf{x}}$  can be written as a formula in terms of  $p_{\mathbf{z}}$ . At this point,  $p_{\mathbf{x}}$  can be written in terms of  $p_{\mathbf{z}}$  and the Jacobian determinant via the change-of-variables formula, as in Equation 1.

$$\log p_{\mathbf{x}}(\mathbf{x}) = \log p_{\mathbf{z}}(\mathbf{z}) + \log |J|, J = \det \frac{\partial \mathbf{z}}{\partial \mathbf{x}} \quad (1)$$

In general, the model is trained to maximize the log-likelihood  $\log p_{\mathbf{x}}(\mathbf{x})$  of the training data, and approximates the distribution of the input data (Caterini & Loaiza-Ganem,

2022). Normalizing flows can be categorized by whether the determinant of the Jacobian (i.e., the volume term) is fixed (Dinh et al., 2015) or varies with the input (Rezende & Mohamed, 2015; Dinh et al., 2017; Kingma & Dhariwal, 2018; Behrmann et al., 2019; Chen et al., 2019; Durkan et al., 2019). When sampling new data, sampling is performed by extracting it from the pre-defined  $p_z$  and inputting it as the input of  $f^{-1}$ . The normalizing flow has the advantage of being able to obtain the estimated likelihood of the input data, unlike models such as variational autoencoder and generative adversarial network. Additionally, normalizing flows have the advantage of not requiring approximate likelihood inference techniques (Nalisnick et al., 2019a). However, normalizing flow has two constraints: (1) the computational cost of the Jacobian determinant must remain reasonable, and (2) the inverse of  $f$  must exist. Therefore, the following methodologies were utilized to ensure the ease of Jacobian calculation and the existence of the inverse  $f^{-1}$ : methods such as a coupling layer (Dinh et al., 2015; 2017; Kingma & Dhariwal, 2018), special-form transformations (Rezende & Mohamed, 2015), and power-series approximations with Lipschitz constraint (Behrmann et al., 2019; Chen et al., 2019) are commonly used.

## 2.2. Counterintuitive Phenomenon of Likelihood

Nalisnick et al. (2019a) reported that a counterintuitive phenomenon regarding likelihood assignment occurs in models that can obtain estimated likelihood, such as normalizing flow, in the image domain. This study lays the foundation for identifying the cause of this phenomenon or suggesting solutions. Kirichenko et al. (2020); Schirrmeister et al. (2020) improved anomaly detection performance by modifying flow architectures. In particular, the latter introduced an approach that reflects the hierarchical data structure, thereby improving detection performance. Serrà et al. (2020) quantified complexity through a general compression algorithm such as PNG, based on experimental results, demonstrating that simple images exhibit higher likelihood, and presented an anomaly score combining the likelihood and complexity terms. Kamkari et al. (2024) used Local Intrinsic Dimension (LID) to measure an image's simplicity and proposed a dual thresholding method for LID and likelihood to improve anomaly detection performance. Morningstar et al. (2021); Osada et al. (2024); Ahmadian et al. (2021) mitigated the drawback of using only a single likelihood score by estimating the density of a vector that combines the likelihood with several auxiliary statistics (e.g., complexity, the log-determinant of the Jacobian). Nalisnick et al. (2019b) demonstrated the perspective that detection may fail because in-distribution data are located in the typicality set (Cover, 1999) and OOD data is in the high density set. Zhang et al. (2021) presented the view that the counterintuitive phenomenon occurs due to misestimation of the model.

Le Lan & Dinh (2021) demonstrated that even with a perfect model, simple likelihood-based methods can fail due to variants in the representation. Ren et al. (2019) improved detection performance by using the likelihood ratio between the background and semantic models and Caterini & Loaiza-Ganem (2022) explained the cause of this phenomenon from an entropic perspective and why the likelihood ratio model works well.

However, these works primarily focus on image-domain mechanisms or remedies and do not establish a domain-agnostic criterion for counterintuitive failures, nor do they quantify how often such failures occur across a broad suite of tabular benchmarks. Our work fills this gap with Definition 3.3 and large-scale tabular evaluation, complemented by a dimension- and correlation-based analysis of when likelihood-only testing becomes fragile.

## 3. Definition of Counterintuitive Phenomenon

Earlier research (Kirichenko et al., 2020) noted instances where in-distribution and OOD data had overlapping likelihoods in tabular datasets, but these findings were limited to only a few datasets and lacked comprehensive comparisons with other anomaly detection models. To address limitations in prior work's explanations of the counterintuitive phenomenon, we propose a generalized definition of the counterintuitive phenomenon that applies to diverse domains. To formalize this phenomenon, we begin by establishing two core assumptions:

**Assumption 3.1** (Relatively Low Performance). *If a counterintuitive phenomenon occurs, most comparison models should outperform the generative model on an anomaly detection task.*

**Assumption 3.2** (High Performance Gap). *Even if the above condition is satisfied, the performance gap between the generative model and comparison models must be significant to qualify as a counterintuitive phenomenon. If the gap is small, it cannot be considered counterintuitive.*

We now formalize this phenomenon using these assumptions.

**Definition 3.3** (Occurrence of Counterintuitive Phenomenon, Informal). *Let  $\text{AUROC}_0$  denote the AUROC of the likelihood-only test using the generative model  $P_{\theta_0}$  on a normal/abnormal dataset pair  $(P, Q)$ , and let  $\text{AUROC}_i$  denote that of the  $i$ -th comparison model for  $i = 1, \dots, k$ . We say that a counterintuitive phenomenon occurs if both conditions hold:*

$$\frac{1}{k} \sum_{i=1}^k \mathbb{1}\{\text{AUROC}_i > \text{AUROC}_0\} > \beta, \quad (2)$$

$$\min_{i: \text{AUROC}_i > \text{AUROC}_0} (\text{AUROC}_i - \text{AUROC}_0) > \gamma. \quad (3)$$

Definition 3.3 states that a counterintuitive phenomenon occurs when the proportion of comparison models whose AUROC exceeds that of the generative model  $P_{\theta_0}$  is greater than  $\beta$ , and the minimum AUROC difference between  $P_{\theta_0}$  and the models that outperform  $P_{\theta_0}$  is greater than  $\gamma$ . Consequently, Definition 3.3 enables performance comparisons using relative AUROC, allowing us to determine whether a counterintuitive phenomenon has occurred, rather than merely inferring its presence from a low AUROC. Importantly, Definition 3.3 is modality-agnostic: it does not encode domain-specific patterns, but operationalizes counterintuitiveness as a relative failure (a non-trivial performance gap against baselines), separating it from intrinsic dataset difficulty. The fully rigorous formulation of Definition 3.3 is provided in Appendix B.

Consider the CIFAR-10 (in-distribution) vs. SVHN (out-of-distribution). According to Morningstar et al. (2021), a simple likelihood test using the Glow (Kingma & Dhariwal, 2018) yielded an AUROC of 6.4%. In contrast, Sun et al. (2022) achieved AUROC scores exceeding 90% with their proposed method and comparison models. Based on Definition 3.3, this case clearly demonstrates a counterintuitive phenomenon, as the generative model performs significantly worse than the comparison models. To explore whether this phenomenon occurs in tabular data, we conducted experiments to test if a counterintuitive phenomenon, as defined in Definition 3.3, appears in tabular anomaly detection datasets.

## 4. Experiment

**Dataset and Preprocessing** The experiment was conducted using the data split protocol in Zong et al. (2018). Under this protocol, 50% of the normal data is used for training, and the remaining 50% of the normal and abnormal data are used for testing. We used **all 47 tabular and 10 CV/NLP embedding datasets** presented in ADBench. Using the entire dataset was motivated by Shwartz-Ziv & Armon (2022), who criticized that researchers often introduce selection bias by choosing specific datasets to inflate performance. To address this, we included all proposed benchmark datasets without exclusion. All models utilized the RobustScaler provided by the Python library Scikit-learn (Pedregosa et al., 2011) to standardize the input data, except for NeuTraLAD and DRL. NeuTraLAD was trained without feature scaling, as applying RobustScaler led to a noticeable degradation in performance in our preliminary experiments. In contrast, DRL employed the StandardScaler, following the preprocessing configuration specified in the official implementation. This choice was made to ensure consistency with the original experimental setup and to enable a fair comparison with the reported results.

**Models** We compared the performance of 6 shallow AD

models and 7 deep AD models. We implemented the shallow models using PyOD (Zhao et al., 2019) and Scikit-learn (Pedregosa et al., 2011). The compared shallow models are PCA (Shyu et al., 2003), LOF (Breunig et al., 2000), IF (Liu et al., 2008), OCSVM (Schölkopf et al., 1999), CO-POD (Li et al., 2020), and ECOD (Li et al., 2022). The compared deep models are DAGMM (Zong et al., 2018), DeepSVDD (Ruff et al., 2018), GOAD (Bergman & Hoshen, 2020), NeuTraLAD (Qiu et al., 2021), ICL (Shenkar & Wolf, 2022), MCM (Yin et al., 2024), DRL (Ye et al., 2025) and NF-SLT with NICE (Dinh et al., 2015). For NF-SLT with NICE, we used 10 coupling layers and trained the model for 200 epochs with weight decay 1e-4. We optimized the negative log-likelihood of the latent variables using AdamW (Loshchilov & Hutter, 2019) with a CosineAnnealingWarmRestarts learning rate scheduler (Loshchilov & Hutter, 2017). The batch size was set to 512, and the latent prior was fixed to  $\mathcal{N}(0, I_d)$ . Overall hyperparameter settings and implementation details are provided in Appendix G.

**Evaluation** We evaluate all AD models using AUROC and AUPRC. For tabular datasets, we run 10 repeated trials and report the mean AUROC and the relative rank of each method in Table 1. For the main results in Table 1, we adopt a single global hyperparameter configuration per model, selected to maximize the AUROC averaged across all tabular datasets. Since default hyperparameters are not directly comparable across heterogeneous AD models, we tune each method over its predefined search space and fix one global configuration to avoid per-dataset oracle tuning. Specifically, each candidate configuration is evaluated with 10 trials, and we select the one that achieves the best aggregated mean AUROC. We additionally report (i) the standard deviation across the 10 trials and (ii) per-dataset performance under the selected global configurations in Appendix J. Appendix G provides the hyperparameter search spaces for all models and includes a sensitivity analysis. Finally, additional flow variants for NF-SLT are reported in Appendix H.

**Experiment Result** Consider Definition 3.3. If the counterintuitive phenomenon were also prevalent in the tabular domain, we would expect a method to exhibit a high fail ratio even if it performs well on some datasets, and the combination of a high top-2 ratio with many failures would indicate such behavior. Moreover, for any failed dataset, the minimum performance gap relative to competing models should be large. However, as shown in Table 1, NF-SLT exhibits a lower fail ratio than both shallow and deep baselines and outperforms the other metrics overall. On the ‘yeast’ dataset, where NF-SLT shows relatively low performance, the minimum performance difference between MCM and NF-SLT in AUROC is only 0.02. Thus, this case does not satisfy the second condition in Definition 3.3 and cannot be attributed to a counterintuitive phenomenon. NF-SLT also outperforms

Table 1. (Top): Evaluation performance on 47 tabular datasets. (Bottom): Evaluation performance on 10 CV/NLP embedding datasets. Top2 Ratio indicates the proportion of datasets where a method ranks within the top-2 in AUROC, and Fail Ratio indicates the proportion where it ranks 9th or lower.

Method	AUROC $\uparrow$	AUPRC $\uparrow$	Avg. Rank $\downarrow$	Top2 Ratio $\uparrow$	Fail Ratio $\downarrow$
PCA	0.7715	0.5209	7.13	0.15	0.45
LOF	0.8169	0.5606	6.11	0.17	0.26
IF	0.8014	0.5060	6.23	0.19	0.21
OCSVM	0.6562	0.3833	10.34	0.06	0.77
COPOD	0.7471	0.4419	8.40	0.11	0.57
ECOD	0.7425	0.4530	8.74	0.06	0.68
DAGMM	0.6467	0.3468	11.45	0.00	0.89
DeepSVDD	0.7687	0.5388	7.74	0.02	0.49
GOAD	0.6086	0.4114	10.60	0.04	0.62
NeuTraLAD	0.8081	0.5694	6.17	0.26	0.30
ICL	0.8208	0.6170	5.70	0.30	0.26
MCM	0.7864	0.5383	7.34	0.11	0.36
DRL	0.8363	0.6124	5.04	0.21	0.09
NF-SLT	<b>0.8575</b>	<b>0.6398</b>	<b>3.74</b>	<b>0.40</b>	<b>0.06</b>

Dataset	DeepSVDD	GOAD	NeuTraLAD	ICL	MCM	DRL	NF-SLT
CIFAR-10	0.9103	0.9334	0.9405	0.9254	0.9381	0.8416	<b>0.9527</b>
FashionMNIST	0.9117	0.9060	0.9360	0.9266	0.9380	0.8240	<b>0.9455</b>
MNIST-C	0.8348	0.7741	0.8519	0.8257	0.8836	0.7312	<b>0.8950</b>
MVTecAD	0.7542	0.7960	0.8874	0.8874	0.8408	0.7093	<b>0.9100</b>
SVHN	0.5466	0.5366	0.5774	0.5626	0.5771	0.5251	<b>0.5842</b>
20news	0.5547	0.5438	0.6001	0.6087	0.5995	0.5457	<b>0.6547</b>
agnews	0.6630	0.5857	0.6509	0.6697	0.7252	0.5817	<b>0.7591</b>
amazon	0.5833	0.5613	0.6010	0.6022	0.6049	0.5424	<b>0.6194</b>
imdb	0.5090	<b>0.5398</b>	0.5393	0.5098	0.5090	0.4666	0.5013
yelp	0.6490	0.6138	0.6620	0.6690	0.6750	0.5705	<b>0.6971</b>

deep models on ADBench’s CV/NLP embedding datasets, except for the ‘imdb’ dataset. Although NF-SLT underperforms the best baseline on ‘imdb’, the performance gap is marginal and again fails to satisfy the second condition of Definition 3.3, so we do not regard it as a counterintuitive case. To assess the sensitivity of Definition 3.3, we set the competitor pool to the full set of comparison models and swept thresholds over  $\beta \in \{\frac{8}{13}, \frac{9}{13}, \frac{10}{13}, \frac{11}{13}, \frac{12}{13}, 1\}$  and  $\gamma \in \{0.3, 0.4, 0.5, 0.6\}$ , evaluating all possible  $(\beta, \gamma)$  combinations. Across this entire grid, no tabular dataset was classified as counterintuitive, so no decision flips occurred; the flip frequency is therefore 0% within the tested ranges. We further repeated this analysis with alternative competitor pools: (i) shallow-model competitors only and (ii) deep-model competitors only, adjusting  $\beta$  appropriately to reflect the pool size. Under both alternative pools and the same  $\gamma$  sweep, we again observed no counterintuitive cases and hence no decision flips. Additionally, we report detection performance on datasets dominated by categorical features and diverse anomaly types in Appendix E, where NF-SLT again shows superior performance. For an additional consistency check, we also compared NF-SLT against other test methodologies such as the typicality test (Nalisnick et al., 2019b); the corresponding results are summarized in Appendix I.

## 5. Why Is The Simple Likelihood Test Successful in Tabular Data?

### 5.1. High Dimension Perspective

Based on Fact 1.1, we explain why likelihood testing can succeed on tabular data due to their lower dimensionality.

It has been reported that the case where the likelihood of normal and anomaly data is inverted in the image domain usually occurs when the normal data has a more complex texture than the anomaly data, that is, when the complexity of the normal data is higher than that of the anomaly data (Serrà et al., 2020). Additionally, we can interpret high data complexity as indicating high entropy of the underlying distribution. Hence, to explain why the counterintuitive phenomenon rarely occurs in the tabular domain, we extend the likelihood-gap expression of Caterini & Loaiza-Ganem (2022), which characterizes the expected likelihood difference between normal and abnormal data in terms of entropy, and link it to Fact 1.1.

Let the distribution of normal data be  $P$ , the distribution of abnormal data be  $Q$ , and let  $P_\theta$  be a model such as normalizing flow that estimates the density of  $P$ . Then, the gap of the likelihood of each distribution estimated by  $P_\theta$  can be expressed as follows:

$$\begin{aligned} & \mathbb{E}_{\mathbf{x} \sim P} [\log P_\theta(\mathbf{x})] - \mathbb{E}_{\mathbf{x} \sim Q} [\log P_\theta(\mathbf{x})] \\ &= D_{KL}(Q||P_\theta) - D_{KL}(P||P_\theta) + \mathbb{H}(Q) - \mathbb{H}(P) \end{aligned} \quad (4)$$

where  $\mathbb{H}(P)$  is entropy of distribution  $P$ , and  $D_{KL}(Q||P_\theta)$  is the KL-divergence of distribution  $Q$  and density estimation model like normalizing flow  $P_\theta$ . In Equation 4, if the difference in entropy between the two distributions  $\mathbb{H}(Q) - \mathbb{H}(P)$  is a very small negative number, the expectation gap of the likelihood can become negative. However, in the previous study by Caterini & Loaiza-Ganem (2022), the effect of the dimension in expectation of likelihood gap was not analyzed, so we analyzed how the dimension can affect the expectation of likelihood gap and included it in Theorem 5.4 and the proof of this is reported in Appendix D.

**Theorem 5.4** (Impact of Dimensionality on Likelihood Gap). *Let  $P = \prod_{i=1}^d p_i(x_i)$  and  $Q = \prod_{i=1}^d q_i(x_i)$  be independent  $d$ -dimensional continuous probability density models in  $\mathbb{R}^d$  with same conditions as Lemma 5.1. Let  $P_\theta$  be a well-trained density estimation model approximates  $P$  (i.e.,  $p_\theta(x) \rightarrow p(x)$  pointwisely as  $\theta \rightarrow \theta_0$ ). If  $\mathbb{H}(P) - \mathbb{H}(Q) > D_{KL}(Q||P)$ , the lower bound of gap between the expectation of the likelihood for  $P$  and  $Q$  decreases linearly with respect to  $d$ .*

According to Theorem 5.4, even when  $P_\theta$  is an almost perfect model, if  $P$  and  $Q$  are  $d$ -dimensional independent distributions and the difference in entropy between the two distributions is greater than  $D_{KL}(Q||P)$ , it can be verified that the lower bound of gap between the expectation of the likelihood for  $P$  and  $Q$  is negative and decreases linearly with the dimension. This shows that as the dimension increases, the phenomenon of inversion of the likelihood expectation of data sampled from each distribution can become more severe. Additionally, we show in Corollary 5.6

that under additional assumptions on the entropy of the distribution, not only the likelihood gap but also the upper bound of the AUROC, which is a practical and widely used evaluation metric, is inversely proportional to the dimension. The proof of this result is provided in Appendix D.

**Corollary 5.6** (Dimensionality and AUROC Upper Bound). *Building on the assumptions of Corollary 5.5, suppose the  $n$ -th absolute central moment of the log-likelihood difference,  $\log p_\theta(Y) - \log p_\theta(X)$ , scales as  $\mathcal{O}(d^k)$  for some  $n > 1$  and  $k < n$ . In this case, if the average log-likelihood gap becomes negative, the maximum achievable AUROC for distinguishing samples from  $P$  and  $Q$  is inversely related to the dimensionality  $d$ . This indicates that as the dimension increases, the likelihood test becomes fundamentally less effective at separating normal and abnormal samples.*

According to Corollary 5.6, the upper bound on the achievable AUROC decreases as the dimensionality increases. In turn, a tighter AUROC upper bound for NF-SLT increases the chance that it underperforms other models by a non-trivial margin, making the counterintuitive criterion in Definition 3.3 more likely to be satisfied. To validate this prediction, we conducted dimensionality-reduction experiments. Specifically, we applied ICA (Hyvärinen & Oja, 2000) to high-dimensional image data and retained a varying number of independent components. Using RealNVP, we then measured the AUROC as a function of the retained dimension, as reported in Table 2. This setup isolates the effect of dimensionality on likelihood ranking and provides empirical support for our theoretical claims.

*Table 2.* AUROC scores for likelihood tests as a function of dimensionality (number of PCs) using RealNVP with MLP (image preprocessed by ICA). The upper block corresponds to cases where  $\mathbb{H}(P) > \mathbb{H}(Q)$ , and the lower block corresponds to  $\mathbb{H}(P) < \mathbb{H}(Q)$ .

In-dist ( $P$ ) / Out-dist ( $Q$ )	1024	512	256	30
CIFAR-10 / SVHN	0.2311	0.2924	0.2984	0.3143
CIFAR-100 / SVHN	0.0843	0.1160	0.2036	0.3490
CelebA / SVHN	0.1207	0.1782	0.2745	0.4711
SVHN / CIFAR-10	0.9917	0.9843	0.9486	0.8520
SVHN / CIFAR-100	0.9933	0.9536	0.9137	0.8622
SVHN / CelebA	0.9976	0.9811	0.9722	0.9481

The results in Table 2 show that, when  $\mathbb{H}(P) > \mathbb{H}(Q)$  holds, the AUROC increases as the dimensionality decreases. Notably, the improvement remains substantial even when the dimensionality is reduced to almost 1% of the original dimension. In contrast, the cases to the right of the bold vertical line show decreasing AUROC as the dimension decreases. This matches the trivial behavior obtained by reversing the entropy condition, i.e.,  $\mathbb{H}(P) < \mathbb{H}(Q)$ , in Theorem 5.4 and Corollary 5.6. Therefore, even if the  $\mathbb{H}(P) > \mathbb{H}(Q)$  condition is satisfied, tabular data can be considered more advantageous in the simple likelihood test because they are

less exposed to the problems that arise in high dimensions, as indicated by Fact 1.1.

We reported the experimental setting of Table 2 and examined the impact of dimensionality by simply applying PCA to assess how AUROC behaves when the independence assumption is violated, observing a trend consistent with Table 2, with results reported in Appendix C.4. Furthermore, in the same appendix we provide additional results on the effect of dimension in real tabular data. Specifically, we find that applying PCA to reduce dimension can improve NF-SLT on the highest-dimensional tabular dataset in AD-Bench (InternetAds), consistent with our dimensionality analysis. In addition, we conducted an experiment to distinguish between two Gaussian distributions with different means using a likelihood test using a NICE and RealNVP consisting of ReLU-like functions, and found that as the dimension increases, the AUROC approaches 0.5. Since this phenomenon is also a case where AUROC seriously decreases simply as the dimension increases, we present experiments and our theoretical analysis about flow's latent vector in high dimensional space in Appendix C.

## 5.2. Feature Correlation Perspective

In prior work, Kirichenko et al. (2020) showed that likelihood inversion can arise in normalizing flows on image data due to strong local pixel correlations. Meanwhile, Schirrmeister et al. (2020) reported that, in the image domain, OOD detection performance can improve when flow architectures use multi-layer perceptrons (MLP) rather than convolutional neural network (CNN) in certain settings. As noted by Battaglia et al. (2018), CNNs exhibit an inductive bias known as locality, making them particularly effective for image data where local pixel correlations are strong. In contrast, MLPs have a weaker inductive bias and are therefore more suitable for tabular data, where strong structural correlations between features are not assumed.

Leveraging Fact 1.2 and noting that architectural inductive bias is shaped by domain-specific characteristics, we argue that the counterintuitive phenomenon is rare in tabular data. This is because tabular features are inherently heterogeneous, unlike the homogeneous features of image data. Images are homogeneous because all features are of the same type (pixels), take values in the same range (e.g., 0–255), and exhibit strong local correlations. By contrast, tabular features are heterogeneous: they include many types (e.g., continuous, discrete, categorical), their ranges or categories are defined independently, and no specific structural relationships between features are assumed.

Hence, we use overall feature correlation as a proxy to interpret the differences between the two domains in terms of heterogeneity versus homogeneity. To quantify feature heterogeneity and homogeneity, we measure overall feature

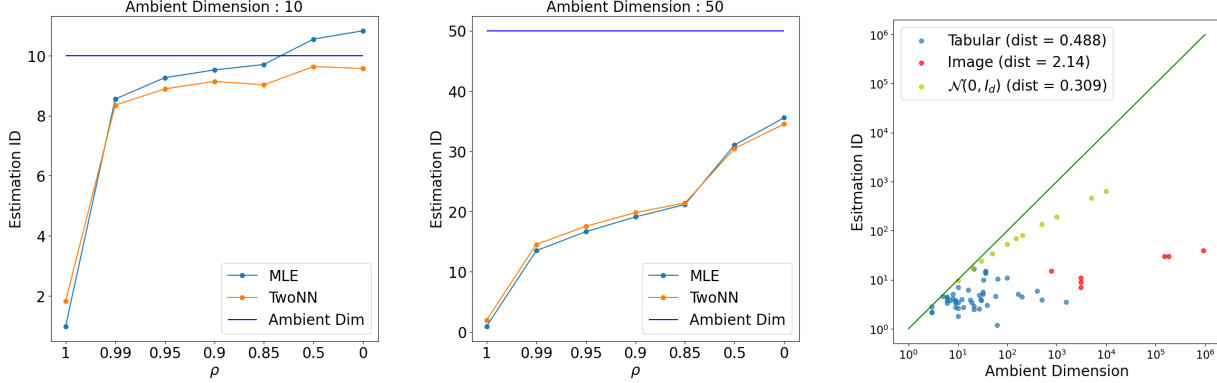


Figure 1. (Left, Center) : Estimation of ID according to changes in  $\rho$ . The x-axis represents the value of  $\rho$  and the y-axis represents dimension. The horizontal line represents the ambient dimension. (Right) : Log-scale scatter plot for ID estimate and ambient dimension using the TwoNN method of real dataset and synthetic dataset sampled by  $\mathcal{N}(0, I_d)$ . The estimated ID for the image dataset are from Table 1 in Pope et al. (2021). The distance recorded in the legend represents the average value of the distance between each point and the green line indicating when the ID estimate and ambient dimension are the same. Each blue/red point corresponds to one ADBench/image dataset.

correlation, which captures the strength of relationships between features. This is because correlation indicates the strength of the relationship between features, and if this strength is high, it can be interpreted as a strong tendency to follow a specific pattern (e.g., non-linear relationship), making it possible to determine whether the features are heterogeneous or homogeneous. However, common correlation measures (e.g., the Pearson correlation coefficient) are based on pairwise relationships and do not capture the global correlation structure. Hence, we quantify correlation indirectly by considering data  $\mathbf{x} \in \mathbb{R}^d$  and showing that, as the strength of the correlation increases, the intrinsic dimension (ID)  $d'$  becomes smaller relative to the ambient dimension  $d$ . Please refer to Camastra & Stajano (2016) for a definition of ID. Since the exact ID is unknown, we estimate it using MLE (Levina & Bickel, 2004) and TwoNN (Facco et al., 2017), two popular estimators based on fractal-theoretic arguments.

First, we illustrate the relationship between correlation and ID using a toy example based on Gaussian random variables. Let  $X \sim \mathcal{N}(0, \Sigma)$ , where  $\Sigma$  has a  $d$ -dimensional autoregressive covariance structure given by

$$\Sigma = \begin{bmatrix} 1 & \rho & \rho^2 & \dots & \rho^{d-1} \\ \rho & 1 & \rho & \dots & \rho^{d-2} \\ \vdots & & & & \\ \rho^{d-1} & \rho^{d-2} & \rho^{d-3} & \dots & 1 \end{bmatrix}, \rho \in [0, 1]. \quad (5)$$

We set the covariance  $\Sigma$  as in Equation 5 so that adjusting  $\rho$  controls the strength of correlations among variables. As  $\rho$  approaches 1, the correlations among variables become stronger. We then use the TwoNN and MLE ( $k = 10$ ) ID estimators to compute the ID of  $X$  for ambient dimensions 10 and 50 and plot the resulting values as a function of  $\rho$  in the

left and center subplots of Figure 1. Through left and center subplot of Figure 1, we can interpret that both ID estimators estimate smaller ID values when  $\rho$  increases. Therefore, it can be seen that stronger correlation between variables leads the ID to take values considerably smaller than the ambient dimension. The center plot of Figure 1 shows that, even when  $\rho = 0$ , the estimators underestimate the ID. This is consistent with prior observations that these estimators tend to underestimate when the true ID is large (Ansuni et al., 2019; Sharma & Kaplan, 2022). In such cases, it is reasonable to interpret the estimate as a lower bound on the true ID. In addition, we report in Appendix F a robustness study of ID estimates on tabular datasets, comparing TwoNN and MLE under various experimental settings. Our analysis places particular emphasis on TwoNN, for which we observe strong robustness to common experimental choices, including sub-sampling and feature scaling.

Based on these results, we define the ratio of the intrinsic dimension to the ambient dimension, which we call the  $d$  Ratio, as a measure of overall feature correlation. A higher degree of feature correlation results in a lower intrinsic dimension estimate, and thus a smaller  $d$  Ratio, whereas weaker correlation yields a larger  $d$  Ratio.

Subsequently, to validate the findings from synthetic data experiments on real datasets, we estimate the ID of real-world image and tabular datasets and compare these estimates to their corresponding ambient dimensions. To compare real-world datasets, we report ID estimates in Table 3 for four standard image benchmarks (MNIST, CIFAR-10, CIFAR-100, SVHN) and for the ADBench tabular datasets, using MLE ( $k = 20$ ) and TwoNN. According to Table 3, all four image datasets have a  $d$  Ratio of about 1%, whereas the tabular datasets exhibit substantially higher  $d$  Ratio values

compared to the images.

Additionally, we recorded a log-scale plot with each dimension as the axis in Figure 1 to check the tendency of the ID estimation values and ambient dimensions of the tabular and image datasets. In Figure 1, the average distance from each point to the green line (where the ID equals the ambient dimension) is larger for image datasets than for tabular datasets. Visually, the blue points (tabular datasets) lie much closer to the green line than the red points (image datasets). The yellow points, corresponding to samples from  $\mathcal{N}(0, I_d)$ , represent theoretically uncorrelated data and also cluster near the green line. These results indicate that tabular datasets have IDs closer to their ambient dimensions than image datasets, implying that tabular features exhibit weaker overall correlation.

*Table 3.* (Top): ID estimates for real datasets. (Bottom): The ratio of datasets whose AUROC rank is  $\geq 3$  as a function of the  $d$ -Ratio threshold, where the  $d$  Ratio denotes the ratio of the intrinsic dimension (estimated by TwoNN) to the ambient dimension. Image-dataset results are reported with reference to [Pope et al. \(2021\)](#).

Dataset	MNIST	CIFAR-10	CIFAR-100	SVHN
MLE	13	26	23	19
TwoNN	15	11	9	7
$d$ Ratio	0.019	0.003	0.002	0.002
Dataset	magicgamma	satellite	landsat	waveform
MLE	7	12	11	16
TwoNN	7	15	14	17
$d$ Ratio	0.700	0.417	0.389	0.810
$d$ Ratio Threshold	0.1	0.2	0.3	0.4
Rank $\geq 3$ Dataset Ratio	0.160	0.440	0.640	0.760
$d$ Ratio Threshold	0.5	0.6	0.7	0.8
Rank $\geq 3$ Dataset Ratio	0.840	0.840	0.92	1.000

Furthermore, for the 25 datasets on which NF-SLT does not achieve top performance (rank  $\geq 3$ ), Table 3 reports the fraction whose  $d$  Ratio falls below a given threshold. These results indicate that NF-SLT fails to achieve high performance on most datasets with a low  $d$  Ratio, even within the tabular domain. Therefore, we conclude that one factor behind the high detection performance of tabular data is the heterogeneous nature of its features. We further argue that this effect may act in combination with the improvement in anomaly detection performance obtained using MLPs, as reported in [Schirrmeister et al. \(2020\)](#).

Moreover, to account for the absence of counterintuitive phenomena on CV/NLP embeddings in Section 4, we estimate the intrinsic dimension of the ADBench CIFAR-10 and SVHN embedding representations using TwoNN. The estimated intrinsic dimensions are 23 and 18, respectively, whereas the ambient embedding dimension is 1000 (smaller than the 3072-dimensional raw pixel space). Despite the

reduced ambient dimension, the embeddings exhibit higher intrinsic dimensionality than the original images, implying a larger  $d$  Ratio. This suggests that the embedding features are less strongly correlated and, according to the TwoNN ID estimates, behave as if they lay on a higher-dimensional manifold than the raw pixels. Consequently, the effects of high dimensionality and strong feature correlations that degrade likelihood-based ranking are substantially reduced, allowing NF-SLT to perform effectively on these embeddings. This explanation is consistent with [Kirichenko et al. \(2020\)](#), which reported that the counterintuitive phenomenon is alleviated when using semantic embedding representations instead of raw pixels. Hence, unlike images, tabular data generally exhibit low feature correlation, which contributes to their heterogeneous nature and makes it difficult to satisfy the criterion in Definition 3.3 that the density model attains low relative AUROC, being worse than a large fraction of baselines by a non-trivial margin.

## 6. Conclusion

This paper examined whether the counterintuitive phenomenon in image anomaly detection also appears in tabular data. We first provided a domain-agnostic definition of this phenomenon, allowing it to be analyzed consistently across different data types. Using theoretical and empirical analyses with extensive experiments, we showed that this phenomenon rarely occurs in tabular data when using simple likelihood tests with normalizing flows. Our results show that flow-based likelihood tests effectively detect tabular anomalies, outperforming traditional models without facing the challenges observed in the image domain. For future work, we hope to see the development of flow architectures that better capture semantic information in tabular data, as well as theoretical and empirical studies that extend these methods to high-dimensional tabular datasets with correlation structures comparable to those in image data.

## Impact Statement

This work contributes to a clearer understanding of when likelihood-based anomaly detection with deep generative models is reliable. By demonstrating that the counterintuitive likelihood phenomenon observed in image domains rarely arises in general tabular settings, our findings may help practitioners better assess the applicability of simple likelihood tests in real-world anomaly detection tasks, such as monitoring and risk detection in structured data. We do not anticipate direct negative societal impacts from this work; however, as with other anomaly detection methods, care should be taken when deploying likelihood-based models in high-stakes settings, particularly when data distributions exhibit high dimensionality or strong feature correlations.

## References

Aas, K., Czado, C., Frigessi, A., and Bakken, H. Pair-copula constructions of multiple dependence. *Insurance: Mathematics and economics*, 44(2):182–198, 2009.

Ahmadian, A., Lindsten, F., and Zhou, Z.-H. Likelihood-free out-of-distribution detection with invertible generative models. In *IJCAI*, pp. 2119–2125, 2021.

Alex, K. Learning multiple layers of features from tiny images. <https://www.cs.toronto.edu/kriz/learning-features-2009-TR.pdf>, 2009.

Ansuini, A., Laio, A., Macke, J. H., and Zoccolan, D. Intrinsic dimension of data representations in deep neural networks. *Advances in Neural Information Processing Systems*, 32, 2019.

Anttila, M., Ball, K., and Perissinaki, I. The central limit problem for convex bodies. *Transactions of the American Mathematical Society*, 355(12):4723–4735, 2003.

Battaglia, P. W., Hamrick, J. B., Bapst, V., Sanchez-Gonzalez, A., Zambaldi, V., Malinowski, M., Tacchetti, A., Raposo, D., Santoro, A., Faulkner, R., et al. Relational inductive biases, deep learning, and graph networks. arxiv 2018. *arXiv preprint arXiv:1806.01261*, 2018.

Behrmann, J., Grathwohl, W., Chen, R. T., Duvenaud, D., and Jacobsen, J.-H. Invertible residual networks. In *International conference on machine learning*, pp. 573–582. PMLR, 2019.

Bergman, L. and Hoshen, Y. Classification-based anomaly detection for general data. In *International Conference on Learning Representations*, 2020. URL [https://openreview.net/forum?id=H11K\\_1BtvS](https://openreview.net/forum?id=H11K_1BtvS).

Breunig, M. M., Kriegel, H.-P., Ng, R. T., and Sander, J. Lof: identifying density-based local outliers. In *Proceedings of the 2000 ACM SIGMOD international conference on Management of data*, pp. 93–104, 2000.

Camastra, F. and Staiano, A. Intrinsic dimension estimation: Advances and open problems. *Information Sciences*, 328: 26–41, 2016.

Caterini, A. L. and Loaiza-Ganem, G. Entropic issues in likelihood-based ood detection. In *I (Still) Can't Believe It's Not Better! Workshop at NeurIPS 2021*, pp. 21–26. PMLR, 2022.

Chen, R. T., Behrmann, J., Duvenaud, D. K., and Jacobsen, J.-H. Residual flows for invertible generative modeling. *Advances in Neural Information Processing Systems*, 32, 2019.

Chen, Y. An almost constant lower bound of the isoperimetric coefficient in the kls conjecture. *Geometric and Functional Analysis*, 31:34–61, 2021.

Cover, T. M. *Elements of information theory*. John Wiley & Sons, 1999.

Dinh, L., Krueger, D., and Bengio, Y. Nice: Non-linear independent components estimation. In *International Conference on Learning Representations (ICLR) Workshop*, 2015. URL <https://arxiv.org/abs/1410.8516>.

Dinh, L., Sohl-Dickstein, J., and Bengio, S. Density estimation using real nvp. In *International Conference on Learning Representations*, 2017.

Draxler, F., Wahl, S., Schnoerr, C., and Koethe, U. On the universality of volume-preserving and coupling-based normalizing flows. In *International Conference on Machine Learning*, pp. 11613–11641. PMLR, 2024.

Durkan, C., Bekasov, A., Murray, I., and Papamakarios, G. Neural spline flows. *Advances in neural information processing systems*, 32, 2019.

Eldan, R. Thin shell implies spectral gap up to polylog via a stochastic localization scheme. *Geometric and Functional Analysis*, 23(2):532–569, 2013.

Facco, E., d’Errico, M., Rodriguez, A., and Laio, A. Estimating the intrinsic dimension of datasets by a minimal neighborhood information. *Scientific reports*, 7(1):12140, 2017.

Fan, M., Gu, N., Qiao, H., and Zhang, B. Intrinsic dimension estimation of data by principal component analysis. *arXiv preprint arXiv:1002.2050*, 2010.

Fleury, B., Guédon, O., and Paouris, G. A stability result for mean width of  $l_p$ -centroid bodies. *Advances in Mathematics*, 214(2):865–877, 2007.

Golan, I. and El-Yaniv, R. Deep anomaly detection using geometric transformations. *Advances in neural information processing systems*, 31, 2018.

Goodfellow, I. J., Pouget-Abadie, J., Mirza, M., Xu, B., Warde-Farley, D., Ozair, S., Courville, A., and Bengio, Y. Generative adversarial nets. *Advances in neural information processing systems*, 27, 2014.

Guédon, O. Concentration phenomena in high dimensional geometry. In *ESAIM: Proceedings*, volume 44, pp. 47–60. EDP Sciences, 2014.

Guédon, O. and Milman, E. Interpolating thin-shell and sharp large-deviation estimates for isotropic log-concave measures. *Geometric and Functional Analysis*, 21(5): 1043–1068, 2011.

Han, S., Hu, X., Huang, H., Jiang, M., and Zhao, Y. Ad-bench: Anomaly detection benchmark. *Advances in Neural Information Processing Systems*, 35:32142–32159, 2022.

Hänelmann, S., Castelo, R., and Guinney, J. Gsva: gene set variation analysis for microarray and rna-seq data. *BMC bioinformatics*, 14:1–15, 2013.

Hastie, T. The elements of statistical learning: data mining, inference, and prediction, 2009.

Hyvärinen, A. and Oja, E. Independent component analysis: algorithms and applications. *Neural networks*, 13(4-5): 411–430, 2000.

Kamkari, H., Ross, B. L., Cresswell, J. C., Caterini, A. L., Krishnan, R., and Loaiza-Ganem, G. A geometric explanation of the likelihood OOD detection paradox. In *Forty-first International Conference on Machine Learning*, 2024. URL <https://openreview.net/forum?id=EVMzCKLpdD>.

Kingma, D. P. and Dhariwal, P. Glow: Generative flow with invertible 1x1 convolutions. *Advances in neural information processing systems*, 31, 2018.

Kingma, D. P. and Welling, M. Auto-encoding variational bayes. In *International Conference on Learning Representations (ICLR), Conference Track Proceedings*, 2014. URL <https://arxiv.org/abs/1312.6114>.

Kirichenko, P., Izmailov, P., and Wilson, A. G. Why normalizing flows fail to detect out-of-distribution data. *Advances in neural information processing systems*, 33: 20578–20589, 2020.

Klartag, B. A central limit theorem for convex sets. *Inventiones mathematicae*, 168(1):91–131, 2007.

Le Lan, C. and Dinh, L. Perfect density models cannot guarantee anomaly detection. *Entropy*, 23(12):1690, 2021.

Levina, E. and Bickel, P. Maximum likelihood estimation of intrinsic dimension. *Advances in neural information processing systems*, 17, 2004.

Li, Z., Zhao, Y., Botta, N., Ionescu, C., and Hu, X. Copod: copula-based outlier detection. In *2020 IEEE international conference on data mining (ICDM)*, pp. 1118–1123. IEEE, 2020.

Li, Z., Zhao, Y., Hu, X., Botta, N., Ionescu, C., and Chen, G. H. Ecod: Unsupervised outlier detection using empirical cumulative distribution functions. *IEEE Transactions on Knowledge and Data Engineering*, 35(12): 12181–12193, 2022.

Liu, F. T., Ting, K. M., and Zhou, Z.-H. Isolation forest. In *2008 eighth ieee international conference on data mining*, pp. 413–422. IEEE, 2008.

Loshchilov, I. and Hutter, F. SGDR: Stochastic gradient descent with warm restarts. In *International Conference on Learning Representations*, 2017. URL <https://openreview.net/forum?id=Skq89Scxx>.

Loshchilov, I. and Hutter, F. Decoupled weight decay regularization. In *International Conference on Learning Representations*, 2019. URL <https://openreview.net/forum?id=Bkg6RiCqY7>.

Marcel, S. and Rodriguez, Y. Torchvision the machine-vision package of torch. In *Proceedings of the 18th ACM international conference on Multimedia*, pp. 1485–1488, 2010.

Milligan, G. W. An algorithm for generating artificial test clusters. *Psychometrika*, 50:123–127, 1985.

Morningstar, W., Ham, C., Gallagher, A., Lakshminarayanan, B., Alemi, A., and Dillon, J. Density of states estimation for out of distribution detection. In *International Conference on Artificial Intelligence and Statistics*, pp. 3232–3240. PMLR, 2021.

Nalisnick, E., Matsukawa, A., Teh, Y. W., Gorur, D., and Lakshminarayanan, B. Do deep generative models know what they don’t know? In *International Conference on Learning Representations*, 2019a. URL <https://openreview.net/forum?id=H1xwNhCcYm>.

Nalisnick, E., Matsukawa, A., Teh, Y. W., and Lakshminarayanan, B. Detecting out-of-distribution inputs to deep generative models using typicality. *arXiv preprint arXiv:1906.02994*, 2019b.

Netzer, Y., Wang, T., Coates, A., Bissacco, A., Wu, B., Ng, A. Y., et al. Reading digits in natural images with unsupervised feature learning. In *NIPS workshop on deep learning and unsupervised feature learning*, volume 2011, pp. 4. Granada, 2011.

Osada, G., Takahashi, T., and Nishide, T. Understanding likelihood of normalizing flow and image complexity through the lens of out-of-distribution detection. In *Proceedings of the AAAI Conference on Artificial Intelligence*, volume 38, pp. 21492–21500, 2024.

Papamakarios, G., Pavlakou, T., and Murray, I. Masked autoregressive flow for density estimation. *Advances in neural information processing systems*, 30, 2017.

Pedregosa, F., Varoquaux, G., Gramfort, A., Michel, V., Thirion, B., Grisel, O., Blondel, M., Prettenhofer, P., Weiss, R., Dubourg, V., et al. Scikit-learn: Machine

learning in python. *the Journal of machine Learning research*, 12:2825–2830, 2011.

Pope, P., Zhu, C., Abdelkader, A., Goldblum, M., and Goldstein, T. The intrinsic dimension of images and its impact on learning. In *International Conference on Learning Representations*, 2021. URL <https://openreview.net/forum?id=XJk19XzGq2J>.

Qiu, C., Pfrommer, T., Kloft, M., Mandt, S., and Rudolph, M. Neural transformation learning for deep anomaly detection beyond images. In *International conference on machine learning*, pp. 8703–8714. PMLR, 2021.

Rayana, S. Odds library. *Stony Brook University, Department of Computer Sciences*, 2016.

Ren, J., Liu, P. J., Fertig, E., Snoek, J., Poplin, R., Depristo, M., Dillon, J., and Lakshminarayanan, B. Likelihood ratios for out-of-distribution detection. *Advances in neural information processing systems*, 32, 2019.

Rezende, D. and Mohamed, S. Variational inference with normalizing flows. In *International conference on machine learning*, pp. 1530–1538. PMLR, 2015.

Ruff, L., Vandermeulen, R., Goernitz, N., Deecke, L., Siddiqui, S. A., Binder, A., Müller, E., and Kloft, M. Deep one-class classification. In *International conference on machine learning*, pp. 4393–4402. PMLR, 2018.

Schirrmeyer, R., Zhou, Y., Ball, T., and Zhang, D. Understanding anomaly detection with deep invertible networks through hierarchies of distributions and features. *Advances in Neural Information Processing Systems*, 33: 21038–21049, 2020.

Schölkopf, B., Williamson, R. C., Smola, A., Shawe-Taylor, J., and Platt, J. Support vector method for novelty detection. *Advances in neural information processing systems*, 12, 1999.

Serrà, J., Álvarez, D., Gómez, V., Slizovskaia, O., Núñez, J. F., and Luque, J. Input complexity and out-of-distribution detection with likelihood-based generative models. In *International Conference on Learning Representations*, 2020. URL <https://openreview.net/forum?id=SyxIWpVYvr>.

Sharma, U. and Kaplan, J. Scaling laws from the data manifold dimension. *Journal of Machine Learning Research*, 23(9):1–34, 2022.

Shenkar, T. and Wolf, L. Anomaly detection for tabular data with internal contrastive learning. In *International conference on learning representations*, 2022.

Shwartz-Ziv, R. and Armon, A. Tabular data: Deep learning is not all you need. *Information Fusion*, 81:84–90, 2022.

Shyu, M.-L., Chen, S.-C., Sarinnapakorn, K., and Chang, L. A novel anomaly detection scheme based on principal component classifier. In *Proceedings of the IEEE foundations and new directions of data mining workshop*, pp. 172–179. IEEE Press Piscataway, NJ, USA, 2003.

Steinbuss, G. and Böhm, K. Benchmarking unsupervised outlier detection with realistic synthetic data. *ACM Transactions on Knowledge Discovery from Data (TKDD)*, 15(4):1–20, 2021.

Stimper, V., Liu, D., Campbell, A., Berenz, V., Ryll, L., Schölkopf, B., and Hernández-Lobato, J. M. normflows: A pytorch package for normalizing flows. *Journal of Open Source Software*, 8(86):5361, 2023a.

Stimper, V., Liu, D., Campbell, A., Berenz, V., Ryll, L., Schölkopf, B., and Hernández-Lobato, J. M. normflows: A pytorch package for normalizing flows. *Journal of Open Source Software*, 8(86):5361, 2023b. doi: 10.21105/joss.05361. URL <https://doi.org/10.21105/joss.05361>.

Sun, Y., Ming, Y., Zhu, X., and Li, Y. Out-of-distribution detection with deep nearest neighbors. In *International Conference on Machine Learning*, pp. 20827–20840. PMLR, 2022.

Thimonier, H., Popineau, F., Rimmel, A., and DOAN, B.-L. Beyond individual input for deep anomaly detection on tabular data. In *Forty-first International Conference on Machine Learning*, 2024. URL <https://openreview.net/forum?id=chDpBp2P6b>.

Wang, H., Argenziano, M. G., Yoon, H., Boyett, D., Save, A., Petridis, P., Savage, W., Jackson, P., Hawkins-Daarud, A., Tran, N., et al. Biologically informed deep neural networks provide quantitative assessment of intratumoral heterogeneity in post treatment glioblastoma. *npj Digital Medicine*, 7(1):292, 2024.

Witten, D. M., Tibshirani, R., and Hastie, T. A penalized matrix decomposition, with applications to sparse principal components and canonical correlation analysis. *Biostatistics*, 10(3):515–534, 2009.

Wold, S., Esbensen, K., and Geladi, P. Principal component analysis. *Chemometrics and intelligent laboratory systems*, 2(1-3):37–52, 1987.

Ye, H., Zhao, H., Fan, W., Zhou, M., dan Guo, D., and Chang, Y. Drl: Decomposed representation learning for tabular anomaly detection. In *The Thirteenth International Conference on Learning Representations*, 2025.

Yeh, I.-C. and Lien, C.-h. The comparisons of data mining techniques for the predictive accuracy of probability of default of credit card clients. *Expert systems with applications*, 36(2):2473–2480, 2009.

Yin, J., Qiao, Y., Zhou, Z., Wang, X., and Yang, J. Mcm:  
Masked cell modeling for anomaly detection in tabular  
data. In *The Twelfth International Conference on Learn-  
ing Representations*, 2024.

Zhang, L., Goldstein, M., and Ranganath, R. Understanding  
failures in out-of-distribution detection with deep gener-  
ative models. In *International Conference on Machine  
Learning*, pp. 12427–12436. PMLR, 2021.

Zhang, Y., Sun, Y., Cai, J., and Fan, J. Deep orthogonal  
hypersphere compression for anomaly detection. In *The  
Twelfth International Conference on Learning Represen-  
tations*, 2024.

Zhao, Y., Nasrullah, Z., and Li, Z. Pyod: A python toolbox  
for scalable outlier detection. *Journal of machine learning  
research*, 20(96):1–7, 2019.

Zong, B., Song, Q., Min, M. R., Cheng, W., Lumezanu,  
C., Cho, D., and Chen, H. Deep autoencoding gaus-  
sian mixture model for unsupervised anomaly detection.  
In *International conference on learning representations*,  
2018.

## A. Definition of OOD Detection and Anomaly Detection

The goal of anomaly detection is to build a classifier that detects abnormal, out-of-distribution instances (Golan & El-Yaniv, 2018). In this sense, we follow the common view that anomaly detection and OOD detection share the same objective. While OOD detection assumes that anomalies follow a distribution different from the in-distribution, anomaly detection typically does not impose a specific distributional form. Since this distinction does not affect the fundamental objective we study, we treat the two tasks as equivalent in this work.

## B. Rigorous Formulation of Definition 3.3

**Definition B.1** (Occurrence of Counterintuitive Phenomenon). *Let  $\mathbf{x} \sim P$ , and let  $P_{\theta_0}$  denote a generative model that provides an approximately accurate likelihood estimate for  $\mathbf{x}$ . Let  $P_{\theta_k}$ , the comparison models, which do not necessarily provide likelihood estimates. We assume that all models are well trained.*

*Let  $\varphi_{P_{\theta_0}}(\mathbf{x})$  denote the likelihood estimate from the generative model  $P_{\theta_0}$ , and let  $\varphi_{P_{\theta_k}}(\mathbf{x})$  denote the test statistic (e.g., anomaly score) from the  $k$ -th comparison model. We then define the index set of comparison models that outperform  $P_{\theta_0}$*

$$R = \left\{ i \in [k] \mid \Pr(\varphi_{P_{\theta_0}}(\mathbf{x}) > \varphi_{P_{\theta_0}}(\mathbf{y})) < \Pr(\varphi_{P_{\theta_i}}(\mathbf{x}) > \varphi_{P_{\theta_i}}(\mathbf{y})) \right\}. \quad (6)$$

We say that a counterintuitive phenomenon occurs for  $\mathbf{y} \sim Q$  if the following two conditions hold:

1. A sufficiently large fraction of comparison models outperform the generative model:

$$\frac{1}{k} \sum_{i=1}^k \mathbb{1} \left\{ \Pr(\varphi_{P_{\theta_0}}(\mathbf{x}) > \varphi_{P_{\theta_0}}(\mathbf{y})) < \Pr(\varphi_{P_{\theta_i}}(\mathbf{x}) > \varphi_{P_{\theta_i}}(\mathbf{y})) \right\} > \beta. \quad (7)$$

2. The minimum performance gap between the generative model and the outperforming comparison models exceeds  $\gamma$ :

$$\min_{i \in R} \left( \Pr(\varphi_{P_{\theta_i}}(\mathbf{x}) > \varphi_{P_{\theta_i}}(\mathbf{y})) - \Pr(\varphi_{P_{\theta_0}}(\mathbf{x}) > \varphi_{P_{\theta_0}}(\mathbf{y})) \right) > \gamma. \quad (8)$$

## C. Additional Description from Section 5.1

In the following, we examine from a theoretical perspective why anomaly detection with normalizing flows can fail as dimensionality increases. To this end, we review concentration behavior of the Euclidean norm in high dimensions, which play a key role in understanding how normalizing flows distinguish between normal and anomalous data. This is because the normalizing flow model  $f$  is trained on normal data  $X$  such that  $f(X)$  follows a standard Gaussian distribution, i.e.,  $f(X) \sim N(0, I)$  and the training objective is to maximize the log-likelihood,  $\log P_{N(0, I)}(f(X) \mid \Theta) \propto -\|f(X)\|_2^2$ , where  $\Theta$  represents the parameters of the normalizing flow and  $\|\cdot\|_2$  denotes the Euclidean norm. Our analysis in Section C.1 & C.2 cannot directly analyze the volume term in models that do not preserve volume, such as RealNVP and Glow, but since Osada et al. (2024) shows that the volume term and the latent likelihood are positively correlated, we indirectly study the relationship with the volume term as a behavior of the latent vector. Additionally, in Section C.3 we show that dimension size has a negative impact on the likelihood test, regardless of the volume term.

### C.1. Euclidean Norm Gets More Concentrated as Dimension Increases

If  $Z \sim \mathcal{N}(0, I_d)$ , then  $\|Z\|_2^2$  concentrates near  $d$ . This means that the test statistic  $\|f(X)\|_2^2$  is close to  $d$  if  $X$  is normal data and the normalizing flow model  $f$  is well trained so that  $f(X)$  follows  $\mathcal{N}(0, I_d)$ . Thus, if the normalizing flow is well-trained, the transformed normal data  $f(X)$  concentrate on a sphere of radius  $\sqrt{d}$  (where  $d$  is the dimensionality of  $X$ ) due to the tail bound properties of sum of independent normal distributions. First, we prove Proposition C.1, which states that as the dimension increases, the Euclidean norm tends to concentrate near  $\sqrt{d}$ .

**Proposition C.1.** *If  $Z \sim \mathcal{N}(0, I_d)$ , then for all  $0 < t < d$ :*

$$\Pr \left( \left| \|Z\|_2^2 - d \right| \geq t \right) \leq 2e^{-\frac{t^2}{8d}} \quad (9)$$

*Proof.* Take a random variable  $Z \sim \mathcal{N}(0, I_d)$  in  $\mathbb{R}^d$ . Then for each  $Z_i \sim N(0, 1)$ ,  $\mathbb{E} \left[ e^{\lambda(Z_i^2 - 1)} \right] = \frac{e^{-\lambda}}{\sqrt{1-2\lambda}} \leq e^{4\lambda^2/2}$  for all  $|\lambda| < 1/4$ . Thus,  $\|Z\|_2^2$  is sub-exponential with parameters  $(2\sqrt{d}, 4)$  and by the properties of sub-exponential random variables, we obtain the concentration bound :  $\Pr \left( \left| \|Z\|_2^2 - d \right| \geq t \right) \leq 2e^{-\frac{t^2}{8d}}$  for  $0 < t < d$ .  $\square$

Since we can show by Proposition C.1 that  $\|Z\|_2^2$  is a sub-exponential random variable with parameter containing  $d$ , we can verify that the probability that the Euclidean norm is observed far from  $\sqrt{d}$  has a sub-exponential tail bound. Then, we prove that the variance of the Euclidean norm tends to concentrate more shrinks relative to the increase in dimensionality.

**Theorem C.2** (Klartag (2007); Fleury et al. (2007); Guédon (2014)).  *$X$  is a log-concave isotropic random variable in  $\mathbb{R}^d$ . If  $\exists \epsilon_d (\epsilon_d \rightarrow 0)$  such that  $\Pr \left( \left| \frac{\|X\|_2}{\sqrt{d}} - 1 \right| \geq \epsilon_d \right) \leq \epsilon_d$ , then  $\lim_{d \rightarrow \infty} \frac{\text{Var} \|X\|_2}{d} = 0$*

**Proposition C.3.** *If  $Z \sim \mathcal{N}(0, I_d)$ ,*

$$\lim_{d \rightarrow \infty} \frac{\text{Var} \|Z\|_2}{d} = 0 \quad (10)$$

*Proof.* From the Proposition C.1, take  $t = dt$ . Then  $\Pr \left( \left| \|Z\|_2^2 - d \right| \geq dt \right) \leq 2e^{-\frac{dt^2}{8}}$  for  $0 < t < 1$ . Since there exists  $\epsilon_d$  such that  $\max\{t, 2e^{-\frac{dt^2}{8}}\} < \epsilon_d$  and  $\epsilon_d \rightarrow 0$  and  $\Pr \left( \left| \frac{\|Z\|_2}{\sqrt{d}} - 1 \right| \geq t \right) = \Pr \left( \left| \frac{\|Z\|_2^2}{d} - 1 \right| \geq t \right)$ , there exists  $\epsilon_d (\epsilon_d \rightarrow 0)$  such that  $\Pr \left( \left| \frac{\|Z\|_2}{\sqrt{d}} - 1 \right| \geq \epsilon_d \right) \leq \epsilon_d$ . By Theorem C.2,  $\lim_{d \rightarrow \infty} \frac{\text{Var} \|Z\|_2}{d} = 0$ .  $\square$

Based on the Proposition C.3, as dimensionality increases, the Euclidean norm of a normal random variable tends to concentrate more quickly relative to the increase in dimensionality. The propositions show that the latent variable of normalizing flow following  $\mathcal{N}(0, I_d)$  has a variance that grows more slowly than the increase in dimension, and that its norm deviates from  $\sqrt{d}$ . This infers that as dimension increases, the latent variable of a normalizing flow corresponding to the normal data is concentrated in a sphere with radius  $\sqrt{d}$ .

Therefore, the model becomes more vulnerable to slight misestimation or error as dimension increases. Also, if the norm of the latent variable corresponding to anomalous data, after being passed through the flow model trained on high-dimensional data, is smaller than  $\sqrt{d}$ , the detection performance may degrade when using a simple likelihood-based test. As a result, outcomes may emerge that align with assumptions about counterintuitive phenomena.

## C.2. Euclidean Norm Is Almost Identical in High-dimensional Space

In high-dimensional spaces, the Euclidean norm becomes a less effective statistical measure, as data points from distinct distributions exhibit nearly identical norms. We summarize and demonstrate that all the isotropic and log-concave random variables become indistinguishable from normal distribution in terms of Euclidean norm as the dimensionality increases. Before starting the analysis, we assume that the distribution of latent vectors obtained when passing the anomaly data through the flow is not  $N(0, I_d)$  but is isotropic and log-concave, as the histograms shown in Appendix C.3 are almost similar.

**Theorem C.4** (Guédon & Milman (2011)). *For a log-concave and isotropic random variable  $X$  in  $\mathbb{R}^d$ , there exists a constant  $C$  such that for any  $t > 0$ ,*

$$\Pr \left( \|X\|_2 - \sqrt{d} \geq t\sqrt{d} \right) \leq Ce^{-c\sqrt{d} \min\{t^3, t\}}$$

**Conjecture C.5** (Thin-Shell Conjecture). *For a log-concave and isotropic random variable  $X$  in  $\mathbb{R}^d$ , there exists a constant  $C$  such that for any  $t > 0$ ,*

$$\Pr \left( \left| \|X\|_2 - \sqrt{d} \right| \geq t\sqrt{d} \right) \leq 2e^{-Ct\sqrt{d}}$$

Although the Thin-Shell conjecture has not yet been proven, there have been several breakthroughs by the works including Eldan (2013) and Chen (2021). As the Thin-Shell Conjecture and the results of Guédon & Milman (2011) show, all the log-concave and isotropic random variables have their Euclidean norm near  $\sqrt{d}$ . This makes it hard for normalizing flow model to distinguish various other log-concave distributions from normal distribution as dimension increases.

**Theorem C.6** (Anttila et al. (2003)).  $X$  is log-concave isotropic random variable in  $\mathbb{R}^d$ . If there exists  $\epsilon_d \rightarrow 0$  as  $d \rightarrow \infty$  such that  $\Pr\left(\left|\frac{\|X\|_2}{\sqrt{d}} - 1\right| \geq \epsilon_d\right) \leq \epsilon_d$ , then there exists  $\theta \in S^{d-1}$

$$\sup_{t>0} \left| \Pr\left(\sum_{i=1}^d \theta_i X_i \leq t\right) - \frac{1}{\sqrt{2\pi}} \int_{-\infty}^t e^{-v^2/2} dv \right| \leq \eta_d$$

, where  $\eta_d \rightarrow 0$

This theorem by Anttila et al. (2003) demonstrates that if the Euclidean norm of a random variable in  $\mathbb{R}^d$  concentrates near  $\sqrt{d}$ , there exists a linear functional of  $X$  that closely approximates a normal distribution. Klartag (2007) extended this result, showing that almost every linear functional of  $X$  becomes approximately normally distributed as  $d \rightarrow \infty$ . These results imply that in high-dimensional spaces, the concentration of the Euclidean norm is nearly identical across distributions, which reduces the effectiveness of hypothesis tests based on the Euclidean norm in distinguishing between distributions. In fact, as shown in the experimental results in Appendix C.3, the likelihood histograms reveal that although the normal and anomaly data are clearly derived from different distributions, the distributions of their likelihoods overlap as the dimensionality increases.

**Theorem C.7.** Let  $X, Y$  be random vectors with isotropic and log-concave density in  $\mathbb{R}^d$  and  $\sigma$  be the uniform probability measure on sphere  $\mathbb{S}^{d-1}$ . Then there exist  $\epsilon_d \rightarrow 0, \delta_d \rightarrow 0$  and subset  $\Theta$  in sphere  $\mathbb{S}^{d-1}$  such that  $\sigma(\Theta) > 1 - \delta_d$  and for any  $\theta, \phi \in \Theta$ ,

$$d_{TV}(\langle X, \theta \rangle, \langle Y, \phi \rangle) < \epsilon_d$$

It is straightforward to derive Theorem C.7 from the theorem in Klartag (2007). This theorem shows that two random vectors from isotropic and log-concave distributions are almost indistinguishable when we only compare their linear measurements. Specifically, since the directions  $\theta$  and  $\phi$  in the Theorem C.7 are drawn uniformly at random and belong to a subset  $\Theta$  with measure approaching 1, the likelihood ordering based on projections strongly correlates with that based on norms. So,

$$d_{TV}(\|X\|_2, \|Y\|_2) = d_{TV}(\langle X, \frac{X}{\|X\|_2} \rangle, \langle Y, \frac{Y}{\|Y\|_2} \rangle) < \epsilon_d \quad (11)$$

which holds with high probability under the assumptions of Theorem C.7. Since normalizing flow model uses Euclidean norm of latent vector, this explains the degraded performance of the normalizing flow model based anomaly detection for high-dimensional data.

### C.3. Experiments for Sections C.1 & C.2 Using Synthetic Data

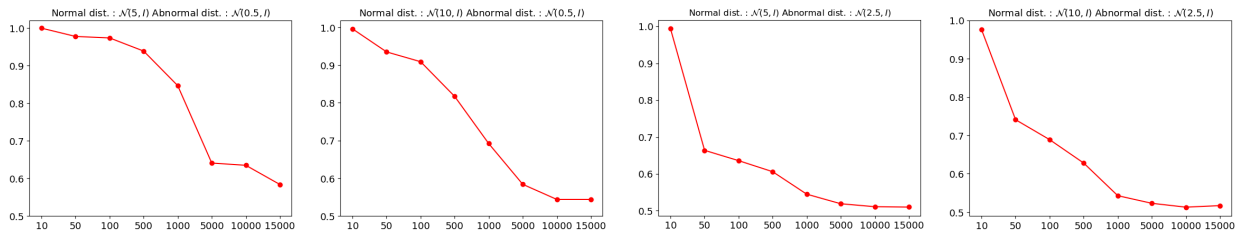


Figure 2. Performance of NF-SLT implemented by NICE across different dimensions. The y-axis represents AUROC, and the x-axis indicates the dimensionality of the data. The titles of each subplot specify distributions' parameters. Subplots 1 and 2 have a larger In/Out of Distribution difference than Subplots 3 and 4, and the speed of performance decay as the dimension increases becomes faster as the distribution difference becomes smaller.

In this section, we present experiments on synthetic data that exhibit behavior consistent with the results in Sections C.1 & C.2. Although those results hold trivially for zero-centered distributions, our analysis goes beyond this case by confirming that the Euclidean norms remain nearly identical even when the distributions are not centered at zero.

The normal and anomaly distributions are both Gaussian but have different parameters  $\mu$  and  $\Sigma$ . We first sample  $10^4$  data points from the normal Gaussian distribution and use them as the training set, training NICE and RealNVP networks with LeakyReLU activations. We then construct a test set by sampling  $10^4$  points from the normal distribution and  $10^4$  points

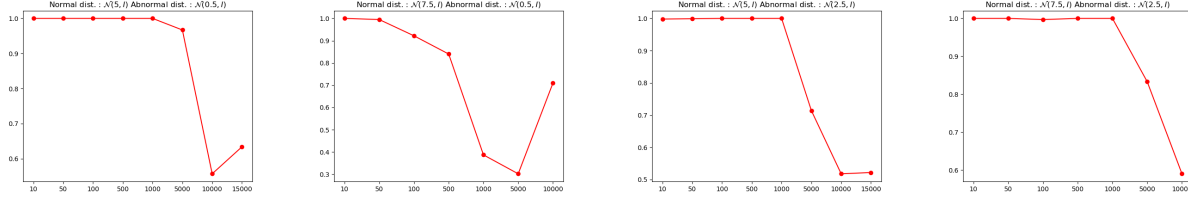


Figure 3. Performance of NF-SLT implemented by RealNVP across different dimensions. The y-axis represents AUROC, and the x-axis indicates the dimensionality of the data. The titles of each subplot specify distributions’ parameters.

from an abnormal Gaussian distribution whose mean differs from that of the normal distribution. A simple likelihood test is performed, and the resulting AUROC as a function of dimensionality is reported for NICE in Figure 2 and for RealNVP in Figure 3. The dimensionalities considered in the experiments are [10, 50, 100, 500, 1000, 5000, 10000, 15000]. Due to numerical stability issues, the RealNVP experiments were run with the in-distribution mean set to  $\mu = 7.5$  instead of  $\mu = 10$ , and for  $\mu = 7.5$  we did not run the experiment at dimension 15000.

As shown in Figure 2, which is the experimental result using NICE, the performance in the 1st and 2nd subfigures degrades significantly between dimensions 1000 and 5000. The 3rd and 4th subfigures begin to degrade in performance at a dimension of 50, smaller than the first two figures, and continue to degrade as the dimension increases. Also we conducted an experiment by changing the means of the in-distribution and out-of-distribution, and confirmed that the AUROC was measured as 1 in most cases. Hence, we found that this phenomenon does not occur symmetrically, similar to the OOD detection experiments on CIFAR-10 and SVHN. In addition, Figure 3, an experiment using RealNVP, shows a similar pattern to Figure 2 in that AUROC decreases rapidly as the dimension increases, except for the second subplot. In Figure 3, the second subplot exhibits an inconsistent trend as dimensionality increases. This instability is likely due to the significant mean difference between in-distribution and out-of-distribution, which introduces numerical stability challenges. This observation underscores the critical impact of distribution alignment on performance scaling.

Additionally, we present a histogram of the log-likelihood of normal and abnormal data along the dimensions from each experiment corresponding to Figure 2 in Figure 4 to 7. The title of each figure indicates the dimension, the x-axis indicates the log-likelihood, and the y-axis indicates the number of data corresponding to the bin. In addition, the orange and blue histograms represent abnormal data and normal data, respectively. In experiments on RealNVP, to see how the volume term affects the likelihood, we visualized the latent norm and volume as histograms in the experiments for the first and third subplots of Figure 3 in Figures 8 to 11.

According to Equation 1 for input data  $\mathbf{x}$ , the log-likelihood  $\log p(\mathbf{x})$  can be calculated with the log-likelihood of the latent  $\mathbf{z}$  corresponding to  $\mathbf{x}$  and the volume term for the distribution set as the prior of the flow. Through the histogram results, we can see that when the AUROC approaches 0.5 (i.e., dimension approaches to 10000), the latent norm becomes identical and the size of the volume term is reversed. This means that when calculating the log-likelihood with Equation 1, the volume term rather has a negative effect on the likelihood test, which is consistent with the results of Figure 4(a) and 4(b) of Nalisnick et al. (2019a). However, in Figures 8 to 11, we can see that the scale of the volume term is much smaller than the latent norm, which can be considered as the log-likelihood scale of the latent because  $\mathcal{N}(0, I_d)$  is set as the prior of the flow in general and the log-likelihood is proportional to  $-\|\mathbf{z}\|_2^2$ . Therefore, the phenomenon that AUROC approaches 0.5 when the dimension increases can be interpreted as the fact that in the case of a volume-preserving model such as NICE, the latent norms become identical, and in the case of a non-volume-preserving model such as RealNVP, the latent norms become identical and the volume term shows a behavior that actually hinders the performance, but the effect of the volume term is so small.

From another perspective, let’s express this case using Equation 4:

$$\begin{aligned} & \mathbb{E}_{\mathbf{x} \sim P} [\log P_\theta(\mathbf{x})] - \mathbb{E}_{\mathbf{x} \sim Q} [\log P_\theta(\mathbf{x})] \\ &= D_{KL}(Q||P_\theta) - D_{KL}(P||P_\theta) + \mathbb{H}(Q) - \mathbb{H}(P) \\ &= D_{KL}(Q||P_\theta) - D_{KL}(P||P_\theta) (\because \mathbb{H}(P) = \mathbb{H}(Q)) \end{aligned} \quad (12)$$

In this case, if  $P_\theta$  is a perfect model, the likelihood gap is guaranteed to be positive, so it can be argued that the reason the term becomes negative is because  $D_{KL}(P||P_\theta)$  eventually increases for high-dimensional data (i.e.,  $P_\theta$  is not a perfect

model). Therefore, it can be argued that this problem occurs because it is difficult to approximate  $P_\theta$  as a perfect model, such as in optimization problems in high-dimensional space. However, the important thing is that even this phenomenon does not occur symmetrically. Therefore, we argue that it is difficult to think that the reason for this phenomenon is simply an optimization problem that occurs in high dimensions.

Consequently, these results support the claim that the norm shown in Theorem C.7 of Section C.2 becomes almost identical in high dimensional space even when the distributions are not zero-centered. In addition, it can be confirmed that the phenomenon occurs regardless of whether the model has a constant volume term or not (i.e., whether the model is volume-preserving) so it can be thought that the presence or absence of a volume term does not help to alleviate the phenomenon. However, we did not observe this phenomenon in real data, and we confirmed that this phenomenon did not occur when the flow activation function was configured as a hyperbolic tangent rather than a ReLU-like function in flow. Therefore, we propose future research to investigate why norms become identical in certain cases when using ReLU-like functions in flow (or why anomalous data are mapped to isotropic and log-concave distributions based on Section 5.1) and to explore whether this phenomenon is reproduced in real data.

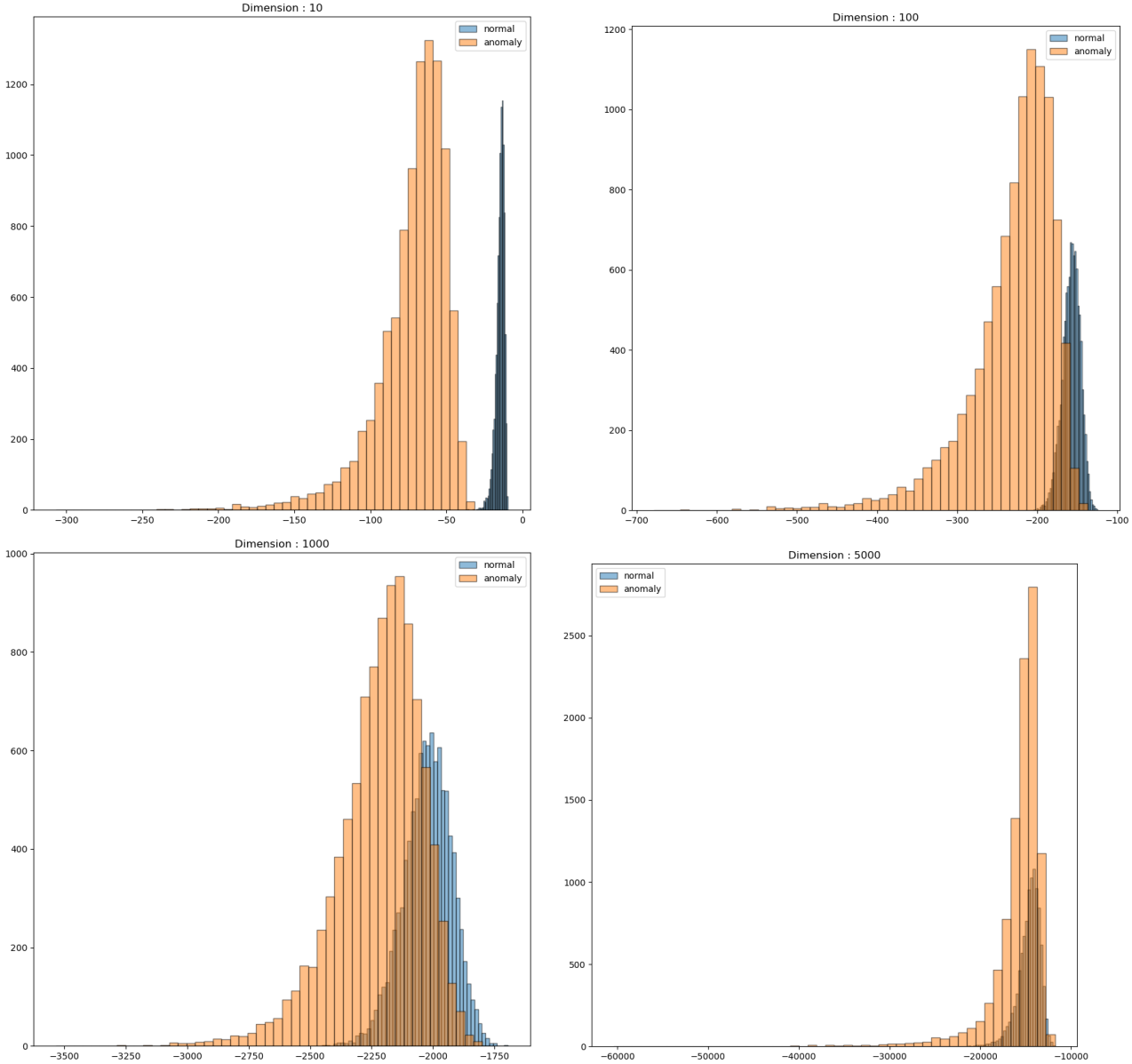


Figure 4. Histogram of log-likelihood values for the 1st subfigure in Figure 2

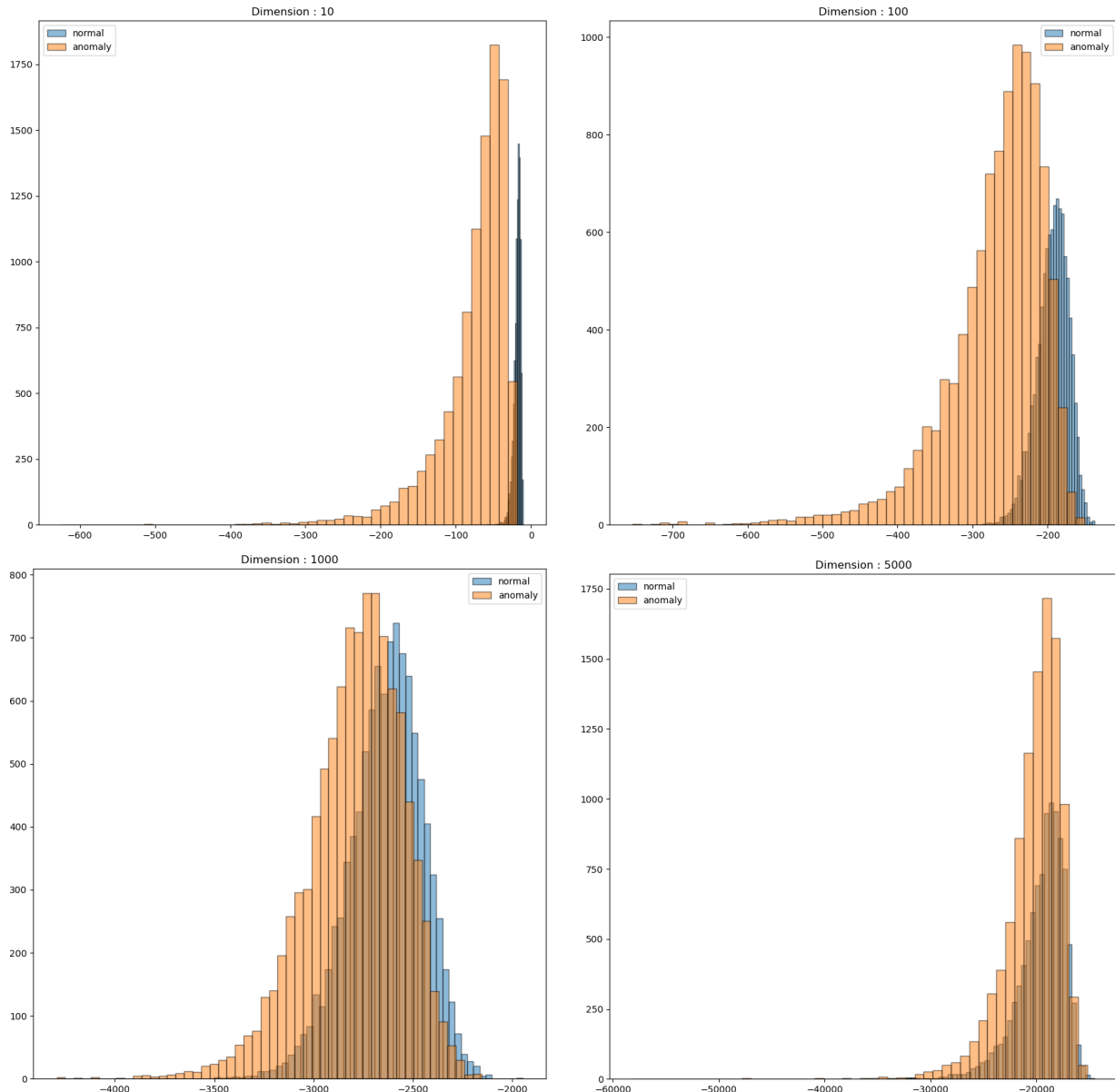


Figure 5. Histogram of log-likelihood values for the 2nd subfigure in Figure 2

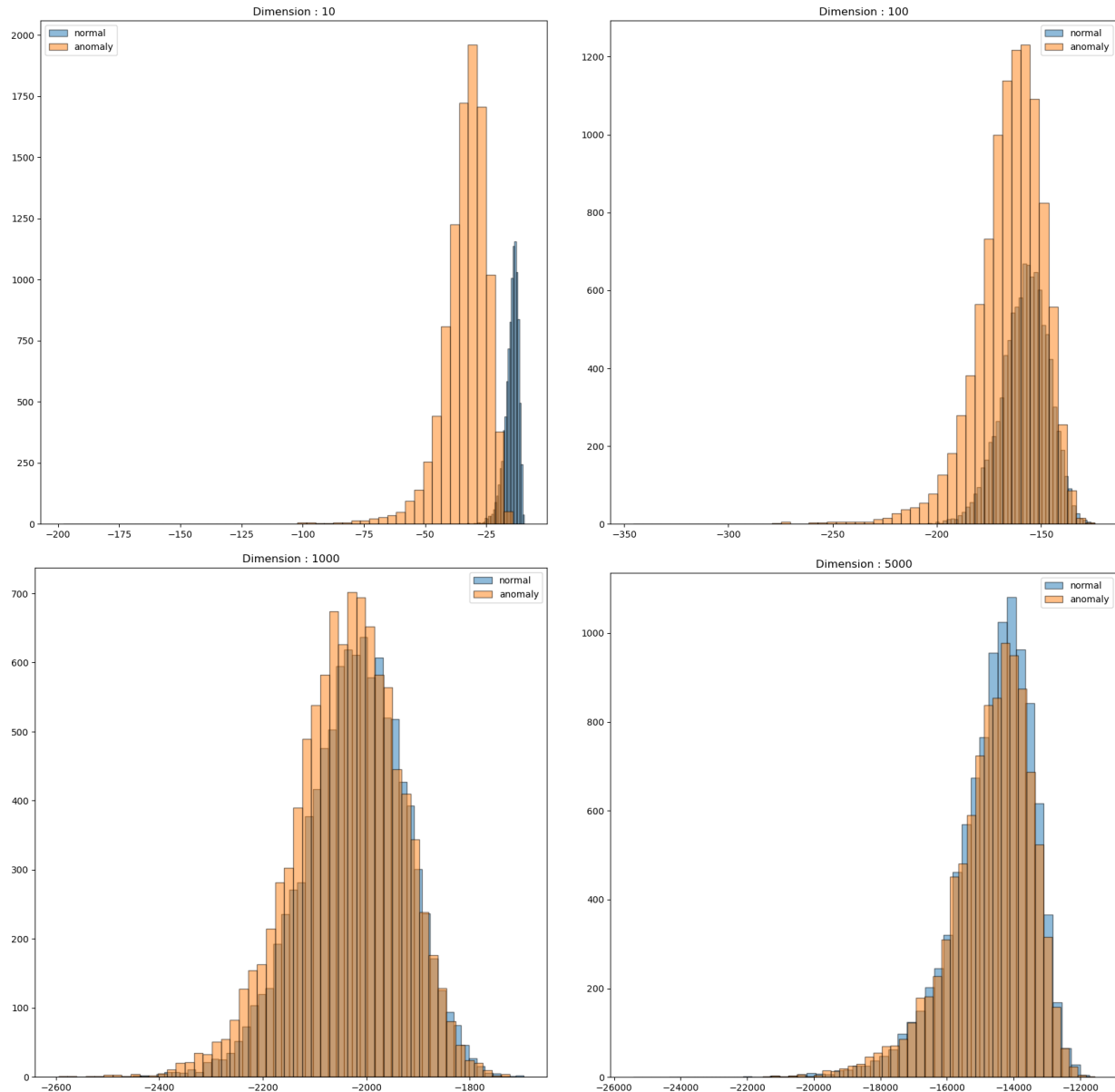


Figure 6. Histogram of log-likelihood values for the 3rd subfigure in Figure 2

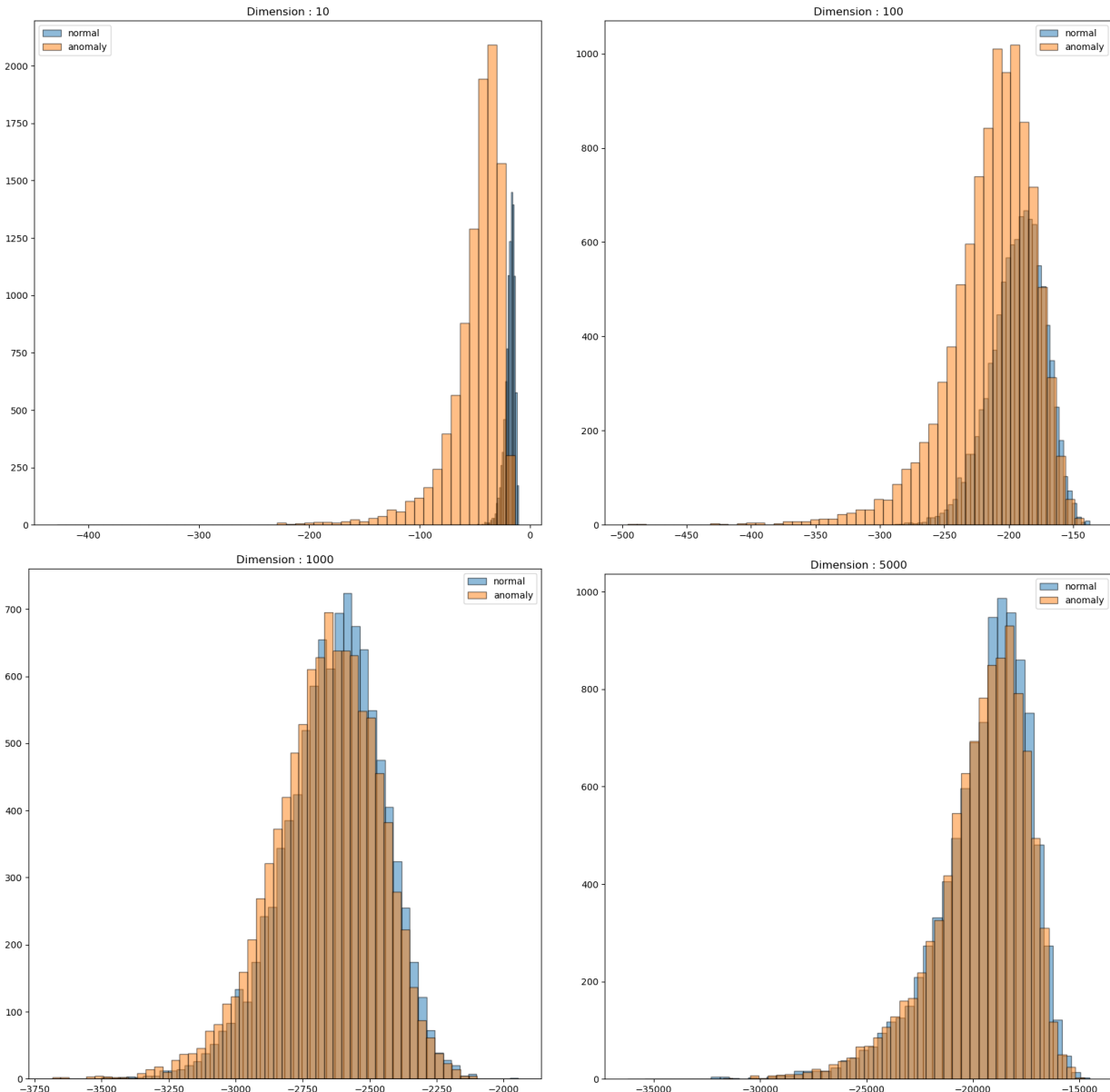


Figure 7. Histogram of log-likelihood values for the 4th subfigure in Figure 2

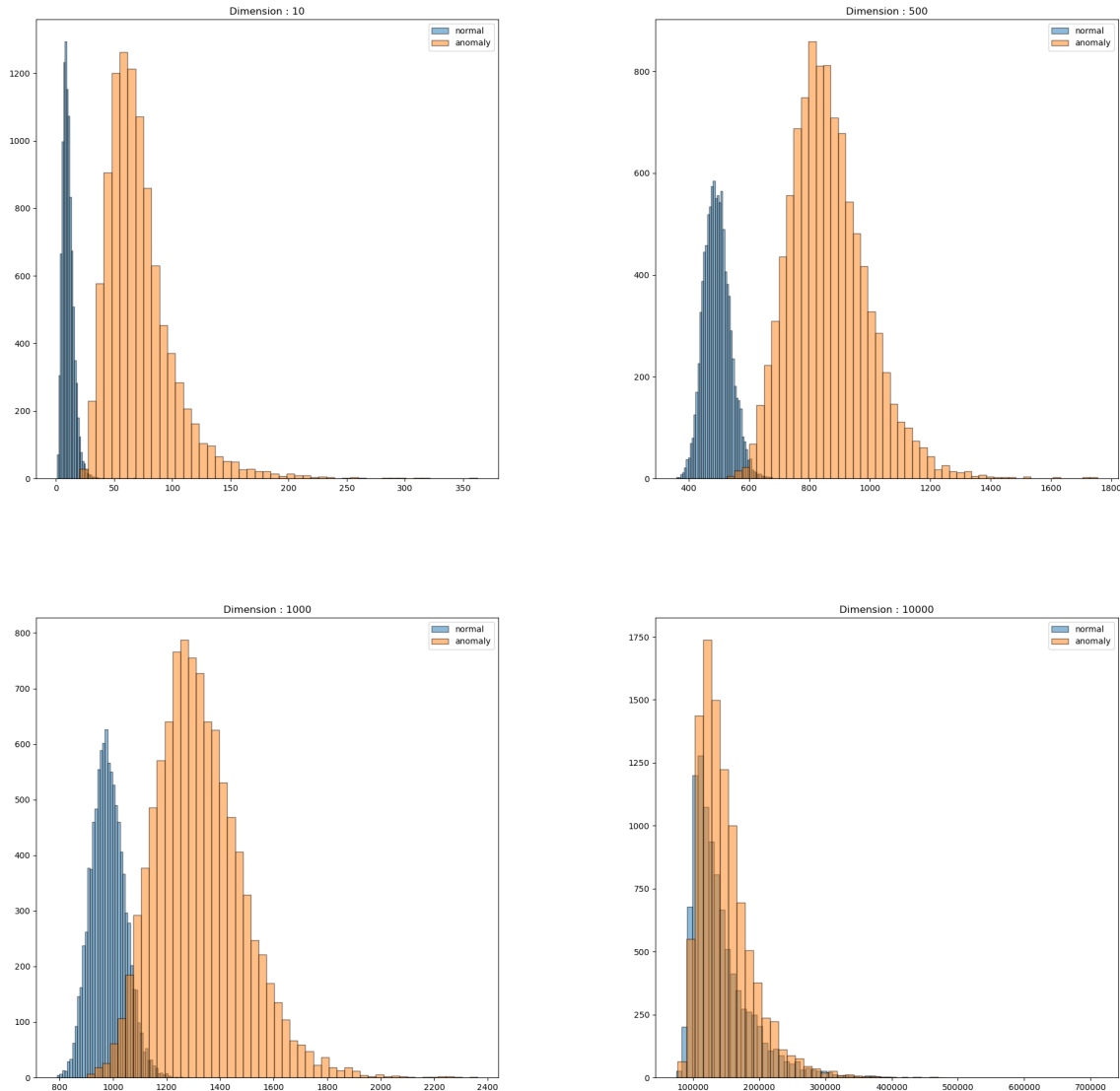


Figure 8. Histogram of latent norm values for the 1st subfigure in Figure 3

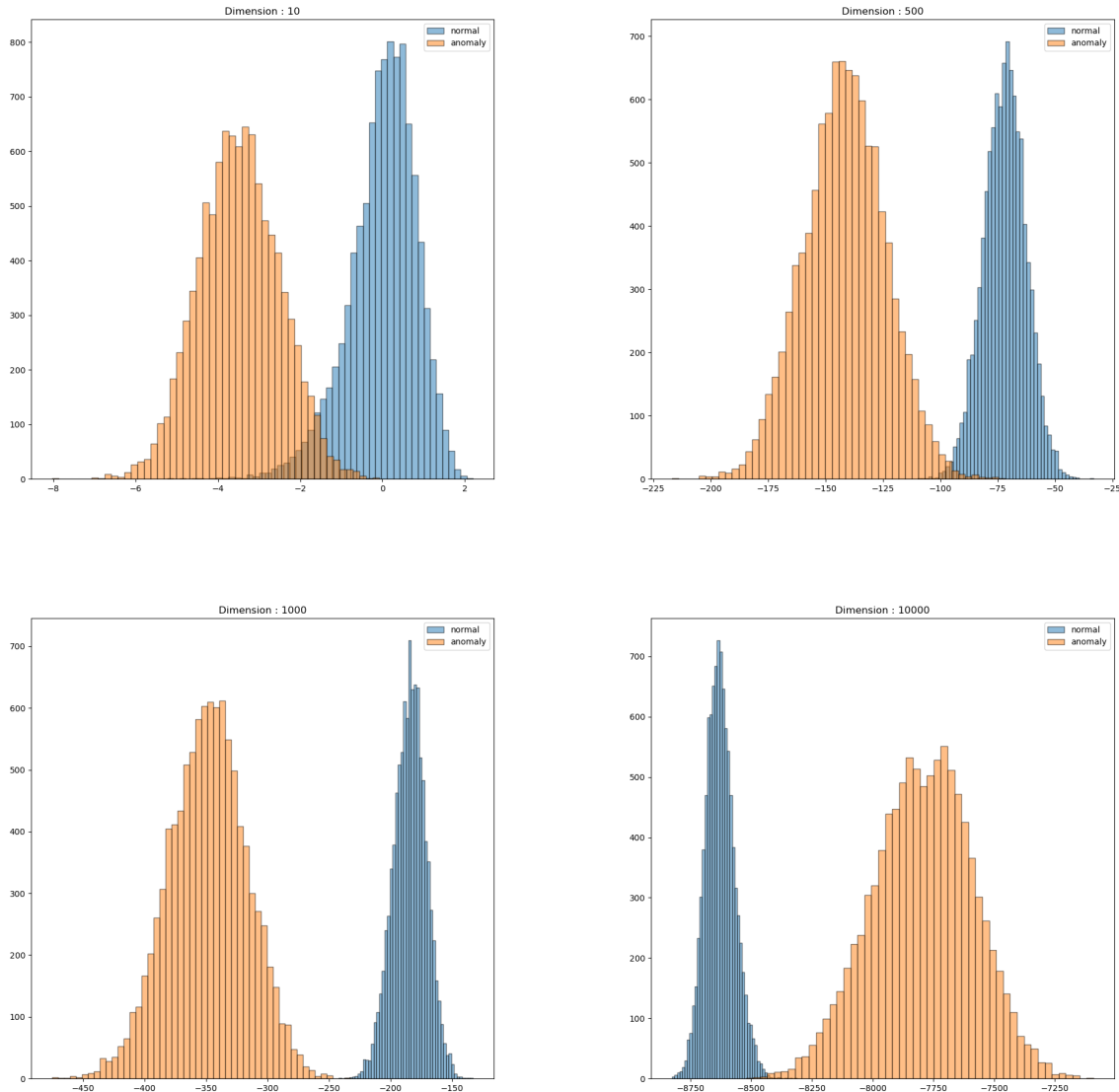


Figure 9. Histogram of volume values for the 1st subfigure in Figure 3

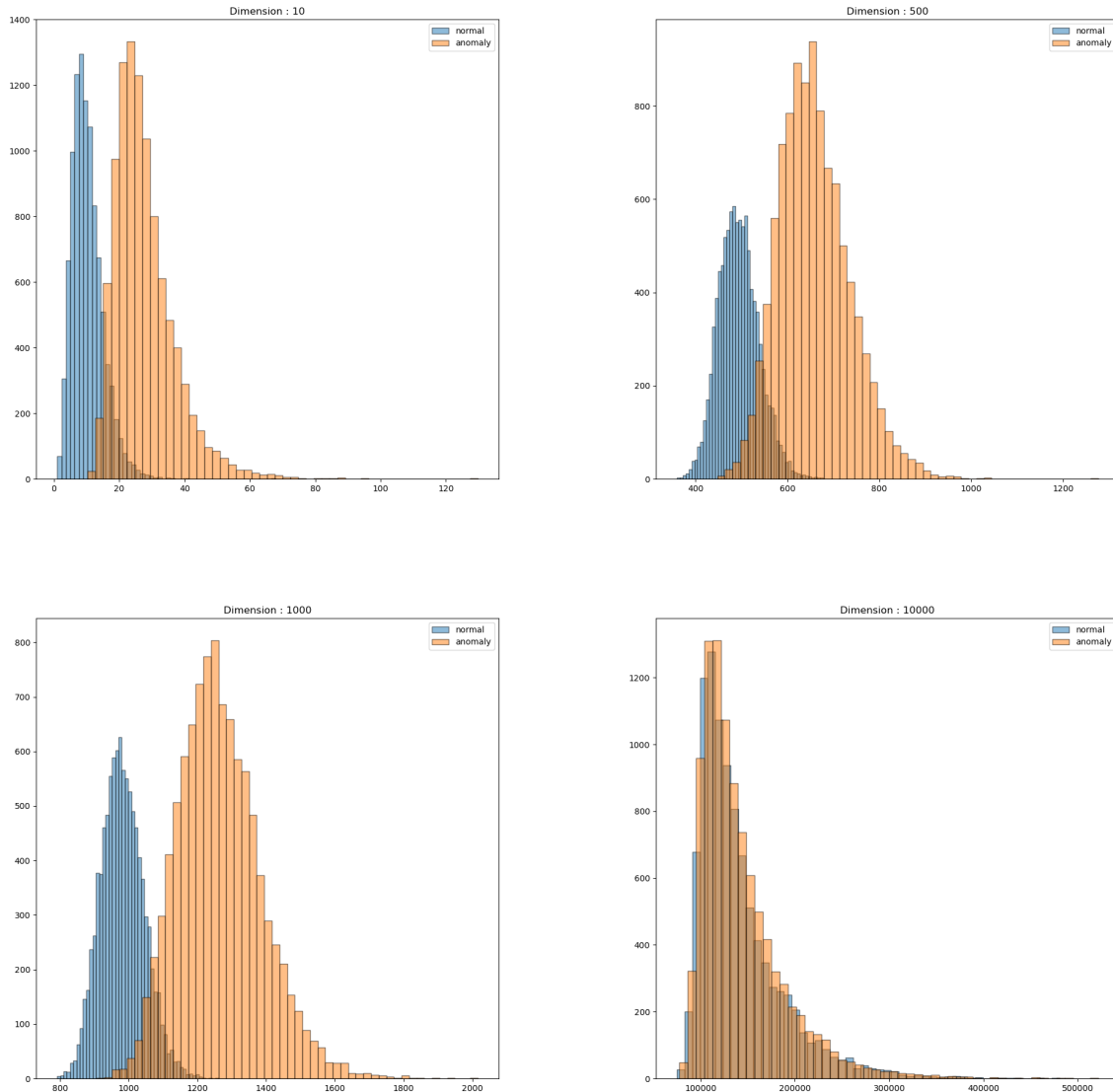


Figure 10. Histogram of latent norm values for the 3rd subfigure in Figure 3

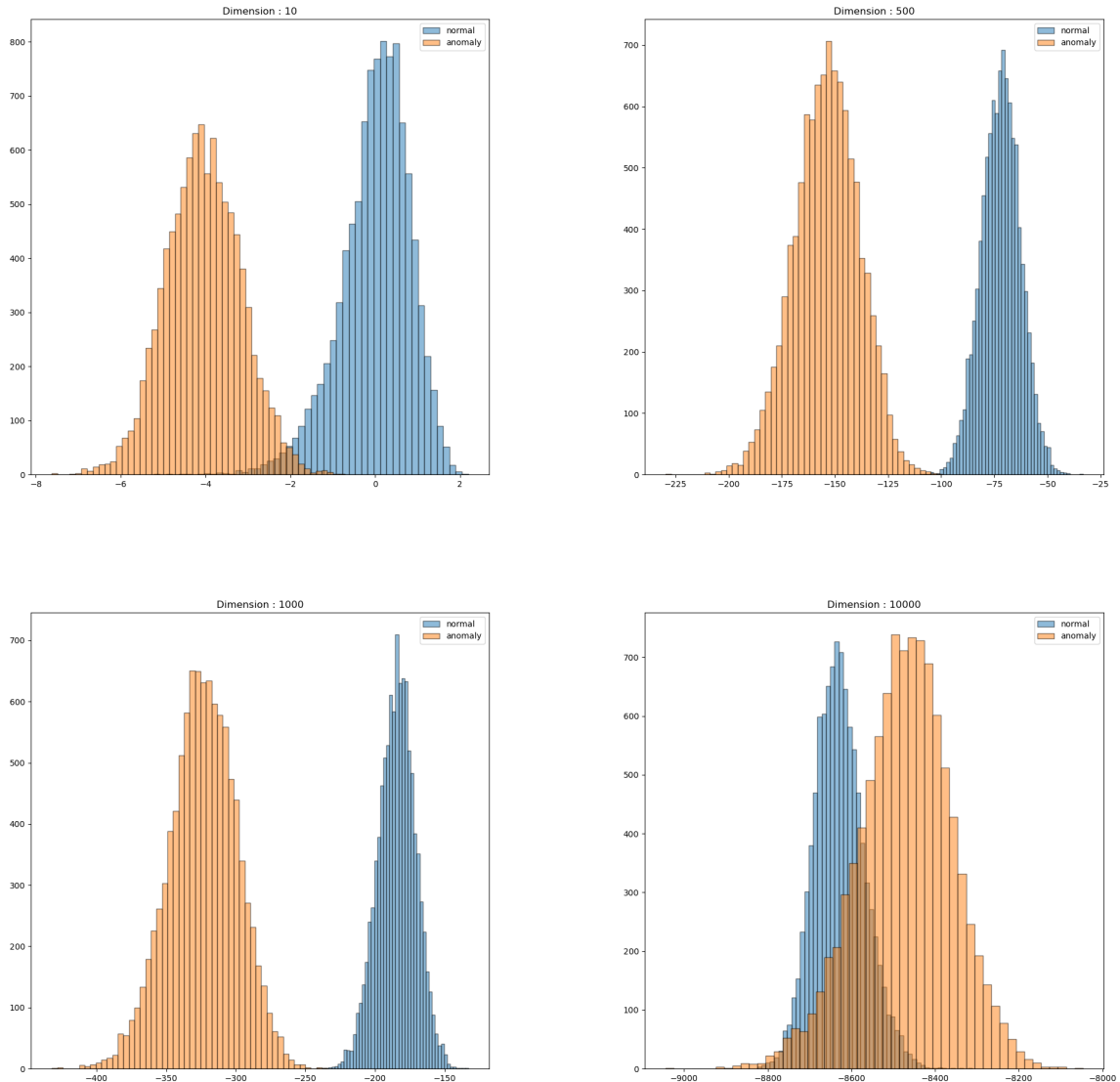


Figure 11. Histogram of volume values for the 3rd subfigure in Figure 3

#### C.4. Experiments of Section 5.1 with Real Data

Table 4. AUROC scores for likelihood tests as a function of dimensionality (number of PCs) using RealNVP with MLP (image preprocessed by PCA). The left block corresponds to  $\mathbb{H}(P) > \mathbb{H}(Q)$ , and the right block corresponds to  $\mathbb{H}(P) < \mathbb{H}(Q)$ .

In-dist ( $P$ ) / Out-dist ( $Q$ )	1024	512	256	30	In-dist ( $P$ ) / Out-dist ( $Q$ )	1024	512	256	30
CIFAR-10 / SVHN	0.1262	0.0950	0.1729	0.3547	SVHN / CIFAR-10	0.9932	0.9807	0.9460	0.8670
CIFAR-100 / SVHN	0.0668	0.0975	0.2015	0.3410	SVHN / CIFAR-100	0.9926	0.9783	0.9436	0.8723
CelebA / SVHN	0.1598	0.2179	0.2988	0.4728	SVHN / CelebA	0.9969	0.9857	0.9709	0.9389
CIFAR-100 / CIFAR-10	0.4804	0.5058	0.4982	0.5021	CIFAR-10 / CIFAR-100	0.5415	0.5287	0.5257	0.5630
CelebA / CIFAR-10	0.8424	0.8511	0.8344	0.6492	CIFAR-10 / CelebA	0.6350	0.5878	0.6747	0.7326

Table 5. AUROC scores for likelihood tests as a function of dimensionality (number of PCs) using RealNVP with MLP (image preprocessed by ICA). The left block corresponds to  $\mathbb{H}(P) > \mathbb{H}(Q)$ , and the right block corresponds to  $\mathbb{H}(P) < \mathbb{H}(Q)$ .

In-dist ( $P$ ) / Out-dist ( $Q$ )	1024	512	256	30	In-dist ( $P$ ) / Out-dist ( $Q$ )	1024	512	256	30
CIFAR-10 / SVHN	0.2311	0.2924	0.2984	0.3143	SVHN / CIFAR-10	0.9917	0.9843	0.9486	0.8520
CIFAR-100 / SVHN	0.0843	0.1160	0.2036	0.3490	SVHN / CIFAR-100	0.9933	0.9536	0.9137	0.8622
CelebA / SVHN	0.1207	0.1782	0.2745	0.4711	SVHN / CelebA	0.9976	0.9811	0.9722	0.9481
CIFAR-100 / CIFAR-10	0.5133	0.5169	0.5046	0.5037	CIFAR-10 / CIFAR-100	0.4970	0.5081	0.5146	0.5588
CelebA / CIFAR-10	0.8511	0.8501	0.8364	0.6515	CIFAR-10 / CelebA	0.3988	0.4041	0.4692	0.6725

First, we will explain the experimental settings in Table 2, 4, 5 for experiment on RealNVP. In both experiments, the model used RealNVP with 16 coupling layers, and each coupling layer consisted of 2 layers, and the hidden dimension of the corresponding layer was set to 256. AdamW was used as the optimizer, and the learning rate was set to 5e-4 and the weight decay was set to 1e-4. The batch size was 256, the scheduler was CosineAnnealingWarmRestarts, and the period was applied as the entire epoch. The epoch was set to 300 for entire cases. The train and test datasets used the train and test datasets specified in advance in torchvision for each dataset. The implementation of the model is referenced from [Stimper et al. \(2023b\)](#).

Although PCA does not satisfy the independence assumption of Theorem 5.4, as it does not preserve statistical independence across components, it remains a widely adopted dimensionality reduction method. Therefore, we evaluated the impact of dimensionality adjustment using PCA on AUROC, as presented in Tables 4. Additionally, Table 5 shows the additional result of Table 2. In this experiment, 16 Glow layer blocks were used, and a model consisting of 3 multi-scale layers was used. Other experimental settings are the same as Table 2.

In the results, it can be confirmed that the AUROC increases as the dimension decreases for the three case from the top above in Table 4 that satisfy the  $\mathbb{H}(P) > \mathbb{H}(Q)$  condition. However, the two cases below in Table 4 and 5 do not show any tendency, which can be interpreted as not showing any specific tendency because the difference in entropy between the two distributions is not large. The reason why the difference in entropy between the two distributions is not large is based on the fact that the complexity histograms of the two images in Figure 2 of [Serrà et al. \(2020\)](#) mostly overlap.

We also adjusted the dimension of the image using the bilinear interpolation resize method provided by torchvision ([Marcel & Rodriguez, 2010](#)) for the raw image, and performed a likelihood test after obtaining the likelihood of the image through Glow which is consist of a CNN, the results are included in Table 6. Since this experiment uses raw images, independence between pixels is not guaranteed, so the theorem presented in Appendix D cannot be applied. However, this experiment was conducted to check the performance trend according to dimension in a situation where there is no independence assumption.

Surprisingly, we can see that there are cases where the AUROC exceeds 0.5 when reducing the size of the two images in Table 6 (see CelebA vs SVHN case). In addition, when SVHN is set to in-distribution and CelebA is set to out-of-distribution, the performance tends to increase as the dimension decreases, which is a result that conflicts with the theorems in Appendix D. We argue that this is because resizing an image via bilinear interpolation strengthens the correlation between image pixels, which significantly reduces the entropy of the image distribution where each texture is complex (i.e., high entropy). Therefore, although it is difficult to confirm the effect of dimension on AUROC through the methodology, it can be seen that not only can the performance be improved by the simple image resize methodology for cases where likelihood inversion occurs, but also it is possible to increase the AUROC to more than 0.5.

Table 6. AUROC scores for likelihood tests as a function of image size using Glow (images resized by bilinear interpolation). The left block corresponds to  $\mathbb{H}(P) > \mathbb{H}(Q)$ , and the right block corresponds to  $\mathbb{H}(P) < \mathbb{H}(Q)$ .

In-dist ( $P$ ) / Out-dist ( $Q$ )	32×32	16×16	8×8	In-dist ( $P$ ) / Out-dist ( $Q$ )	32×32	16×16	8×8
CIFAR-10 / SVHN	0.0716	0.3586	0.4512	SVHN / CIFAR-10	0.9902	0.9777	0.9195
CIFAR-100 / SVHN	0.0846	0.4448	0.3918	SVHN / CIFAR-100	0.9900	0.9798	0.9481
CelebA / SVHN	0.1541	0.3056	0.7037	SVHN / CelebA	0.9850	0.9968	0.9982
CIFAR-100 / CIFAR-10	0.4857	0.4933	0.5016	CIFAR-10 / CIFAR-100	0.5259	0.5446	0.5567
CelebA / CIFAR-10	0.7481	0.7137	0.7557	CIFAR-10 / CelebA	0.5087	0.6181	0.6751

Table 7. AUROC on the InternetAds dataset for NF-SLT and MCM as a function of the retained dimensionality. The ratio denotes the fraction of principal components retained out of 500 PCs (after PCA reduction to 500 dimensions).

Ratio	1.00	0.95	0.90	0.85	0.80	0.75
NF-SLT	0.8180	0.8561	0.8579	0.8377	0.8246	0.8240
MCM	0.7242	0.7217	0.7189	0.7161	0.7158	0.6978

Furthermore, we performed dimension reduction using PCA on the InternetAds dataset, which has the largest dimension ( $d = 1555$ ) in ADBench, and checked the trend of performance changes. The results are included in Table 7.

Through the results in Table 7, we can see that MCM’s performance decreases due to information loss as the dimension decreases. However, NF-SLT’s performance increases when the dimension is reduced, and even when the ratio is reduced to 0.75, the performance is higher than when the entire PC is used. Surely, it is correct according to the theorem that when the dimension decreases, the performance increases and when the gap of entropy is large, it approaches 0.5. However, since it is possible for entropy to be generated from various distributions that are larger or smaller than the normal sample, we explain in Table 7 that not only the AUROC may exceed 0.5, but the performance trend may not increase steadily. This is the basis for the claim that performance degradation can occur even in tabular datasets when the dimension is large, and that performance can be good and counterintuitive phenomenon can rarely occur because the dimension of the tabular dataset is small.

In practice, extremely high-dimensional tabular datasets, such as genomic or metagenomic data, often contain tens of thousands of features. However, these datasets present specific challenges for anomaly detection (AD) due to their inherent feature homogeneity and extreme dimensional complexity. Unlike general tabular data, which typically includes heterogeneous features (e.g., categorical, continuous, nominal), genomic data is characterized by a large number of biologically similar variables with high mutual correlation and tightly constrained value distributions. This fundamental difference means that directly applying standard AD methods to raw genomic or metagenomic data is generally impractical without substantial preprocessing. For instance, metagenomic datasets often include tens of thousands of microbial species abundances or gene expression profiles, where each feature can be highly correlated with others due to shared biological pathways or taxonomic hierarchies. This extreme feature homogeneity can lead to severe overfitting and degraded AD performance if handled without prior dimensionality reduction. Therefore, standard bioinformatics workflows commonly incorporate domain-specific dimensionality reduction techniques, such as sparse Canonical Correlation Analysis (CCA) (Witten et al., 2009), Gene Set Variation Analysis (GSVA) (Hänelmann et al., 2013), or biologically-informed network modeling (Wang et al., 2024), to project these high-dimensional inputs into lower-dimensional, interpretable representations. For example, Hänelmann et al. (2013) demonstrated the use of GSVA to condense over 25,000 genes into biologically meaningful gene sets, significantly reducing the feature space and improving downstream analysis.

Additionally, a recent study by Wang et al. (2024) on BioNet highlighted that even deep learning models for high-dimensional biological data often rely on domain-specific preprocessing to improve interpretability and reduce overfitting. This approach integrates biological knowledge to guide feature selection, effectively reducing the dimensional complexity of the input data. Such preprocessing steps are critical for achieving meaningful predictions and robust model performance, as demonstrated in the context of glioblastoma heterogeneity assessment (Wang et al., 2024). Given these domain-specific preprocessing requirements, our study focuses on heterogeneous tabular data that include diverse feature types such as categorical, continuous, and nominal variables, rather than directly addressing raw, extremely high-dimensional genomic

or metagenomic datasets. This choice aligns with the practical constraints observed in bioinformatics, where specialized preprocessing is essential for effective analysis of such data. Lastly, if there are heterogeneous high-dimensional tabular datasets that do not require such specialized preprocessing, we would be open to exploring them as part of future work, as our current study aims to provide a broadly applicable approach for anomaly detection across diverse real-world datasets.

## D. Proof of Theorems

First, we prove that when the entropy of a normal distribution  $P$  is larger than the entropy of an abnormal distribution  $Q$  and  $P, Q$  are  $d$ -dimensional i.i.d. distributions, the expectation gap of likelihood estimated by the density estimation model  $P_\theta$  trained on data sampled from the normal distribution  $P$  increases as  $d$  increases.

**Lemma 5.1.** *Let  $P, P_\theta, Q$  be continuous probability distributions with its bounded probability distribution function  $p, p_\theta, q$ . If  $p_\theta(x)$  converges to  $p(x)$  pointwisely as  $\theta \rightarrow \theta_0$ ,  $Q$  has bounded support on the intersection of supports of  $P$  and  $P_{\theta_0}$ , then  $\lim_{\theta \rightarrow \theta_0} D_{KL}(Q||P_\theta) = D_{KL}(Q||P)$*

*Proof.*

$$\begin{aligned} D_{KL}(Q||P_\theta) &= \int q(x) \log \frac{q(x)}{p_\theta(x)} dx \\ &= \int q(x) \log \frac{q(x)}{p(x)} dx + \int q(x) \log \frac{p(x)}{p_\theta(x)} dx \\ &= D_{KL}(Q||P) + \int q(x) \log \frac{p(x)}{p_\theta(x)} dx \end{aligned} \quad (13)$$

Thus, it suffices to show  $\int q(x) \log \frac{p(x)}{p_\theta(x)} dx$  converges to 0 when  $\theta$  converges to  $\theta_0$ .

Since  $p, p_\theta$  are bounded and  $Q$  has support on the intersection of supports of  $P$  and  $P_\theta$ , there is constant  $M$  such that  $e^{-M} p_\theta(x) < p(x) < e^M p_\theta(x)$  for every  $x \in \text{Supp}(Q)$ . Thus,  $\{\log \frac{p(x)}{p_\theta(x)}\}$  is uniformly integrable on the support of  $Q$  as  $|\log \frac{p(x)}{p_\theta(x)}| < M$ . Thus,  $\lim_{\theta \rightarrow \theta_0} \int q(x) \log \frac{p(x)}{p_\theta(x)} dx = \int \lim_{\theta \rightarrow \theta_0} q(x) \log \frac{p(x)}{p_\theta(x)} dx$  by Vitali convergence theorem. Since  $p_\theta(x)$  converges to  $p(x)$  pointwisely,  $\lim_{\theta \rightarrow \theta_0} \log \frac{p(x)}{p_\theta(x)} = 0$  and  $\lim_{\theta \rightarrow \theta_0} \int q(x) \log \frac{p(x)}{p_\theta(x)} dx = 0$

□

**Theorem 5.2** (Impact of Dimensionality on Likelihood Gap: i.i.d Case). *Let  $P = \prod_{i=1}^d p(x_i)$  and  $Q = \prod_{i=1}^d q(x_i)$  be identical and independent  $d$ -dimensional continuous probability density models in  $\mathbb{R}^d$  with same conditions as Lemma 5.1. Let  $P_\theta$  is well-trained density estimation model approximates  $P$  (i.e.,  $p_\theta(x) \rightarrow p(x)$  pointwisely). If  $\mathbb{H}(p) - \mathbb{H}(q) > D_{KL}(q||p)$ , gap between the expectation of the likelihood for  $P$  and  $Q$  decreases linearly with respect to  $d$ .*

*Proof.* Gap between the expectation of the likelihood for  $P$  and  $Q$  can be defined as follows as expressed in Caterini & Loaiza-Ganem (2022).

$$\mathbb{E}_{\mathbf{x} \sim P}[\log p_\theta(\mathbf{x})] - \mathbb{E}_{\mathbf{x} \sim Q}[\log p_\theta(\mathbf{x})] \quad (14)$$

Let  $\mathbb{H}(P)$  be entropy of distribution  $P$  and  $D_{KL}(P||Q)$  be KL-divergence between  $P$  and  $Q$ . Then, each term can be decomposed as follows:

$$\begin{aligned} \mathbb{E}_{\mathbf{x} \sim P}[\log P_\theta(\mathbf{x})] &= -D_{KL}(P||P_\theta) - \mathbb{H}(P) \\ \mathbb{E}_{\mathbf{x} \sim Q}[\log P_\theta(\mathbf{x})] &= -D_{KL}(Q||P_\theta) - \mathbb{H}(Q) \end{aligned} \quad (15)$$

So, we can derive as follow:

$$\begin{aligned} &\mathbb{E}_{\mathbf{x} \sim P}[\log P_\theta(\mathbf{x})] - \mathbb{E}_{\mathbf{x} \sim Q}[\log P_\theta(\mathbf{x})] \\ &= -D_{KL}(P||P_\theta) - \mathbb{H}(P) + D_{KL}(Q||P_\theta) + \mathbb{H}(Q) \\ &= D_{KL}(Q||P_\theta) - D_{KL}(P||P_\theta) + \mathbb{H}(Q) - \mathbb{H}(P) \\ &\approx D_{KL}(Q||P_\theta) + \mathbb{H}(Q) - \mathbb{H}(P) \quad (\because p_\theta(x) \rightarrow p(x) \text{ p.w.}) \end{aligned} \quad (16)$$

Then, since  $P$  and  $Q$  are distributed i.i.d.,

$$\begin{aligned}
 & D_{KL}(Q||P_\theta) + \mathbb{H}(Q) - \mathbb{H}(P) \\
 &= D_{KL}(Q||P_\theta) + \mathbb{E}_{\mathbf{x} \sim Q}[-\log Q(\mathbf{x})] - \mathbb{E}_{\mathbf{x} \sim P}[-\log P(\mathbf{x})] \\
 &= D_{KL}(Q||P_\theta) + \mathbb{E}_{\mathbf{x} \sim Q}[-\log Q(x_1, x_2, \dots, x_n)] - \mathbb{E}_{\mathbf{x} \sim P}[-\log P(x_1, x_2, \dots, x_n)] \\
 &= D_{KL}(Q||P_\theta) + \mathbb{E}_{\mathbf{x} \sim Q}[-\log \prod_{i=1}^d q(x_i)] - \mathbb{E}_{\mathbf{x} \sim P}[-\log \prod_{i=1}^d p(x_i)] \\
 &= D_{KL}(Q||P_\theta) + \mathbb{E}_{\mathbf{x} \sim Q}[-\sum_{i=1}^d \log q(x_i)] - \mathbb{E}_{\mathbf{x} \sim P}[-\sum_{i=1}^d \log p(x_i)] \\
 &= D_{KL}(Q||P_\theta) + d(\mathbb{E}_{x \sim q}[-\log q(x)] - \mathbb{E}_{x \sim p}[-\log p(x)]) \\
 &\approx D_{KL}(Q||P) + d(\mathbb{E}_{x \sim q}[-\log q(x)] - \mathbb{E}_{x \sim p}[-\log p(x)]) \quad (\because \text{Lemma 5.1}) \\
 &= d(D_{KL}(q||p) + \mathbb{E}_{x \sim q}[-\log q(x)] - \mathbb{E}_{x \sim p}[-\log p(x)]) \\
 &= d(D_{KL}(q||p) - (\mathbb{E}_{x \sim p}[-\log p(x)] + \mathbb{E}_{x \sim q}[-\log q(x)]))
 \end{aligned} \tag{17}$$

□

Then, if  $\mathbb{H}(p) - \mathbb{H}(q) > D_{KL}(q||p)$ , gap between the expectation of the likelihood for  $P$  and  $Q$  decreases linearly with respect to  $d$ . Through Theorem 5.2, even if the generative model approximates the actual model well, the likelihood inversion phenomenon can occur if the difference in the entropy of  $q$  and  $p$  is larger than the KL-divergence of  $q$  and  $p$ , and this issue escalates with an increase in dimensionality.

**Proposition 5.3** ( $\mathbb{H}(P) - \mathbb{H}(Q) > D_{KL}(Q||P)$  for Gaussian Case). *Let  $P$  and  $Q$  be  $\mathcal{N}(\mu_P, \sigma_P^2 I)$ ,  $\mathcal{N}(\mu_Q, \sigma_Q^2 I)$  such that  $\sigma_P, \sigma_Q$  are non-zero constant. Then,  $\mathbb{H}(P) - \mathbb{H}(Q) > D_{KL}(Q||P)$  holds if  $\|\mu_P - \mu_Q\|^2 < d(\sigma_P^2 - \sigma_Q^2)$ .*

*Proof.* Entropy of  $P$  and  $Q$  can be expressed as follows:

$$\begin{aligned}
 \mathbb{H}(P) &= \frac{d}{2} \log(2\pi e \sigma_P^2) \\
 \mathbb{H}(Q) &= \frac{d}{2} \log(2\pi e \sigma_Q^2)
 \end{aligned} \tag{18}$$

Therefore, we can derive entropy gap of  $P$  and  $Q$  below:

$$\mathbb{H}(P) - \mathbb{H}(Q) = \frac{d}{2} \log \left( \frac{\sigma_P^2}{\sigma_Q^2} \right) \tag{19}$$

Also, since the KL divergence of  $Q$  and  $P$  is known to be in closed form in the case of Gaussian, it can be expressed as follows:

$$\begin{aligned}
 D_{KL}(Q||P) &= \frac{1}{2} \left[ \sigma_P^{-2} (\mu_P - \mu_Q)^T (\mu_P - \mu_Q) + \log \left( \frac{\det \sigma_P^2 I}{\det \sigma_Q^2 I} \right) + \text{tr}(\sigma_P^{-2} \sigma_Q^2 I) - d \right] \\
 &= \frac{1}{2} \left[ \frac{\|\mu_P - \mu_Q\|^2}{\sigma_P^2} + 2d \log \left( \frac{\sigma_P}{\sigma_Q} \right) + \frac{d\sigma_Q^2}{\sigma_P^2} - d \right]
 \end{aligned} \tag{20}$$

Then, we can derive:

$$\begin{aligned}
 D_{KL}(Q||P) - \mathbb{H}(P) + \mathbb{H}(Q) &= \frac{1}{2} \left[ \frac{\|\mu_P - \mu_Q\|^2}{\sigma_P^2} + 2d \log \left( \frac{\sigma_P}{\sigma_Q} \right) + \frac{d\sigma_Q^2}{\sigma_P^2} - d \right] - \frac{d}{2} \log \left( \frac{\sigma_P^2}{\sigma_Q^2} \right) \\
 &= \frac{1}{2} \left[ \frac{\|\mu_P - \mu_Q\|^2}{\sigma_P^2} + 2d \log \left( \frac{\sigma_P}{\sigma_Q} \right) + \frac{d\sigma_Q^2}{\sigma_P^2} - d - 2d \log \left( \frac{\sigma_P}{\sigma_Q} \right) \right] \\
 &= \frac{1}{2} \left[ \frac{\|\mu_P - \mu_Q\|^2}{\sigma_P^2} + \frac{d\sigma_Q^2}{\sigma_P^2} - d \right] \\
 &= \frac{1}{2} \left[ \frac{\|\mu_P - \mu_Q\|^2}{\sigma_P^2} + d \left( \frac{\sigma_Q^2}{\sigma_P^2} - 1 \right) \right]
 \end{aligned} \tag{21}$$

Therefore, if  $\|\mu_P - \mu_Q\|^2 < d(\sigma_P^2 - \sigma_Q^2)$ ,  $D_{KL}(Q||P) - \mathbb{H}(P) + \mathbb{H}(Q) < 0$   $\square$

Proposition 5.3 refers that if the variance of  $P$  is sufficiently larger than the variance of  $Q$  so that the difference between the variances of  $P$  and  $Q$  is greater than the norm of the mean difference, the inequality holds and likelihood inversion can happen. This is consistent with experimental results of Figure 5(a) of Nalisnick et al. (2019a) because for the CIFAR-10 vs SVHN case where likelihood inversion occurs, we can confirm that SVHN is concentrated on the pixel mean of CIFAR-10. Since it is impossible to accurately estimate entropy and KL divergence for the actual data distribution, it is not possible to confirm whether the inequality really holds, but it can be indirectly confirmed that the inequality is satisfied. Additionally, we extend Theorem 5.2 by relaxing the identically assumption.

**Theorem 5.4** (Impact of Dimensionality on Likelihood Gap). *Let  $P = \prod_{i=1}^d p_i(x_i)$  and  $Q = \prod_{i=1}^d q_i(x_i)$  be independent  $d$ -dimensional continuous probability density models in  $\mathbb{R}^d$  with same conditions as Lemma 5.1. Let  $P_\theta$  is well-trained density estimation model approximates  $P$  (i.e.,  $p_\theta(x) \rightarrow p(x)$  pointwisely as  $\theta \rightarrow \theta_0$ ). If  $\mathbb{H}(P) - \mathbb{H}(Q) > D_{KL}(Q||P)$ , the lower bound of gap between the expectation of the likelihood for  $P$  and  $Q$  decreases linearly with respect to  $d$ .*

*Proof.* Similarly proof of Theorem 5.2, we can derive as follow:

$$\begin{aligned}
 &\mathbb{E}_{\mathbf{x} \sim P}[\log P_\theta(\mathbf{x})] - \mathbb{E}_{\mathbf{x} \sim Q}[\log P_\theta(\mathbf{x})] \\
 &= -D_{KL}(P||P_\theta) - \mathbb{H}(P) + D_{KL}(Q||P_\theta) + \mathbb{H}(Q) \\
 &= D_{KL}(Q||P_\theta) - D_{KL}(P||P_\theta) + \mathbb{H}(Q) - \mathbb{H}(P) \\
 &\approx D_{KL}(Q||P_\theta) + \mathbb{H}(Q) - \mathbb{H}(P) \quad (\because p_\theta(x) \rightarrow p(x) \text{ p.w.}) \\
 &= D_{KL}(Q||P_\theta) + \mathbb{E}_{\mathbf{x} \sim Q}[-\log Q(\mathbf{x})] - \mathbb{E}_{\mathbf{x} \sim P}[-\log P(\mathbf{x})] \\
 &= D_{KL}(Q||P_\theta) + \mathbb{E}_{\mathbf{x} \sim Q}[-\log Q(x_1, x_2, \dots, x_n)] - \mathbb{E}_{\mathbf{x} \sim P}[-\log P(x_1, x_2, \dots, x_n)] \\
 &= D_{KL}(Q||P_\theta) + \mathbb{E}_{\mathbf{x} \sim Q}[-\log \prod_{i=1}^d q(x_i)] - \mathbb{E}_{\mathbf{x} \sim P}[-\log \prod_{i=1}^d p(x_i)] \\
 &= D_{KL}(Q||P_\theta) + \mathbb{E}_{\mathbf{x} \sim Q}[-\sum_{i=1}^d \log q(x_i)] - \mathbb{E}_{\mathbf{x} \sim P}[-\sum_{i=1}^d \log p(x_i)] \\
 &= D_{KL}(Q||P_\theta) + \mathbb{E}_{\mathbf{x} \sim Q}[-\sum_{i=1}^d \log q(x_i)] - \mathbb{E}_{\mathbf{x} \sim P}[-\sum_{i=1}^d \log p(x_i)] \\
 &= D_{KL}(Q||P_\theta) + \sum_{i=1}^d (\mathbb{E}_{x_i \sim q_i}[-\log q_i(x_i)] - \mathbb{E}_{x_i \sim p_i}[-\log p_i(x_i)]) \\
 &\approx D_{KL}(Q||P) + \sum_{i=1}^d (\mathbb{E}_{x_i \sim q_i}[-\log q_i(x_i)] - \mathbb{E}_{x_i \sim p_i}[-\log p_i(x_i)]) \quad (\because \text{Lemma 5.1})
 \end{aligned} \tag{22}$$

Then, we define  $k$  as follows:

$$k = \operatorname{argmin}_{i \in [d]} \mathbb{E}_{x_i \sim q_i} [-\log q_i(x_i)] - \mathbb{E}_{x_i \sim p_i} [-\log p_i(x_i)] \quad (23)$$

Because of  $\mathbb{H}(P) - \mathbb{H}(Q) > D_{KL}(Q||P) \geq 0$ ,  $\mathbb{H}(Q) - \mathbb{H}(P)$  has negative value. Therefore, there exists  $\exists j \in [d]$  such that  $\mathbb{E}_{x_j \sim q_j} [-\log q_j(x_j)] - \mathbb{E}_{x_j \sim p_j} [-\log p_j(x_j)]$  is negative. So,

$$\begin{aligned} 0 &> \mathbb{E}_{x_j \sim q_j} [-\log q_j(x_j)] - \mathbb{E}_{x_j \sim p_j} [-\log p_j(x_j)] \\ &\geq \mathbb{E}_{x_k \sim q_k} [-\log q_k(x_k)] - \mathbb{E}_{x_k \sim p_k} [-\log p_k(x_k)] \end{aligned} \quad (24)$$

In conclusion, Equation 24 gives us the following lower bound:

$$\begin{aligned} 0 &> D_{KL}(Q||P) + \sum_{i=1}^d (\mathbb{E}_{x_i \sim q_i} [-\log q_i(x_i)] - \mathbb{E}_{x_i \sim p_i} [-\log p_i(x_i)]) \\ &\geq \sum_{i=1}^d (\mathbb{E}_{x_i \sim q_i} [-\log q_i(x_i)] - \mathbb{E}_{x_i \sim p_i} [-\log p_i(x_i)]) \\ &\geq d(\min_{i \in [d]} \mathbb{E}_{x_i \sim q_i} [-\log q_i(x_i)] - \mathbb{E}_{x_i \sim p_i} [-\log p_i(x_i)]) \\ &= d(\mathbb{E}_{x_k \sim q_k} [-\log q_k(x_k)] - \mathbb{E}_{x_k \sim p_k} [-\log p_k(x_k)]) \end{aligned} \quad (25)$$

□

Through Theorem 5.4, if  $\mathbb{H}(P) - \mathbb{H}(Q) > D_{KL}(Q||P)$  is satisfied, we can see that the lower bound of the gap of the likelihood estimated by  $p_\theta$  for  $\mathbf{x}$  that follows  $P$  and  $Q$  decreases linearly with the dimension. Furthermore, we show in Corollary 5.6 that the upper bound of the likelihood gap can be made smaller in dimension proportional to Theorem 5.4 by making additional assumptions.

**Corollary 5.5** (Special Case of Theorem 5.4: Guaranteed Negative Difference). *Let  $P = \prod_{i=1}^d p_i(x_i)$  and  $Q = \prod_{i=1}^d q_i(x_i)$  be independent  $d$ -dimensional continuous probability density models in  $\mathbb{R}^d$  with same conditions as Lemma 5.1. Let  $P_\theta$  is well-trained density estimation model approximates  $P$  (i.e.,  $p_\theta(x) \rightarrow p(x)$  pointwisely as  $\theta \rightarrow \theta_0$ ). If  $\forall i \in [d]$   $\mathbb{H}(p_i) - \mathbb{H}(q_i) > D_{KL}(q_i||p_i)$ , the lower and upper bound of gap between the expectation of the likelihood for  $P$  and  $Q$  decreases linearly with respect to  $d$ .*

*Proof.* We define  $k$  as follows:

$$k = \operatorname{argmax}_{i \in [d]} \mathbb{E}_{x_i \sim q_i} [-\log q_i(x_i)] - \mathbb{E}_{x_i \sim p_i} [-\log p_i(x_i)] \quad (26)$$

Because of  $\mathbb{H}(p_i) - \mathbb{H}(q_i) > D_{KL}(q_i||p_i) \geq 0$  for  $\forall i \in [d]$ ,  $\mathbb{H}(q_i) - \mathbb{H}(p_i) + D_{KL}(q_i||p_i)$  has negative value. So,

$$\begin{aligned} 0 &> D_{KL}(q_k||p_k) + \mathbb{E}_{x_k \sim q_k} [-\log q_k(x_k)] - \mathbb{E}_{x_k \sim p_k} [-\log p_k(x_k)] \\ &\geq D_{KL}(q_j||p_j) + \mathbb{E}_{x_j \sim q_j} [-\log q_j(x_j)] - \mathbb{E}_{x_j \sim p_j} [-\log p_j(x_j)] \end{aligned} \quad (27)$$

Then, we can derive:

$$\begin{aligned} &\mathbb{E}_{\mathbf{x} \sim P} [\log P_\theta(\mathbf{x})] - \mathbb{E}_{\mathbf{x} \sim Q} [\log P_\theta(\mathbf{x})] \\ &\approx D_{KL}(Q||P) + \sum_{i=1}^d (\mathbb{E}_{x_i \sim q_i} [-\log q_i(x_i)] - \mathbb{E}_{x_i \sim p_i} [-\log p_i(x_i)]) \\ &= \sum_{i=1}^d (D_{KL}(q_i||p_i) + \mathbb{E}_{x_i \sim q_i} [-\log q_i(x_i)] - \mathbb{E}_{x_i \sim p_i} [-\log p_i(x_i)]) \\ &\leq d(\max_{i \in [d]} D_{KL}(q_i||p_i) + \mathbb{E}_{x_i \sim q_i} [-\log q_i(x_i)] - \mathbb{E}_{x_i \sim p_i} [-\log p_i(x_i)]) \\ &= d(D_{KL}(q_k||p_k) + \mathbb{E}_{x_k \sim q_k} [-\log q_k(x_k)] - \mathbb{E}_{x_k \sim p_k} [-\log p_k(x_k)]) \\ &< 0 \end{aligned} \quad (28)$$

□

The results of Corollary 5.5 confirm that the lower and upper bounds of the expectation gap decrease with dimension, and we show in Corollary 5.6 that the upper bound of AUROC can decrease with dimension if we include additional assumption on moment.

**Corollary 5.6** (Dimensionality and AUROC Upper Bound). *Building on the assumptions of Corollary 5.5, suppose the  $n$ -th absolute central moment of the log-likelihood difference,  $\log p_\theta(Y) - \log p_\theta(X)$ , scales as  $\mathcal{O}(d^k)$  for some  $n > 1$  and  $k < n$ . In this case, if the average log-likelihood gap becomes negative, the maximum achievable AUROC for distinguishing samples from  $P$  and  $Q$  is inversely related to the dimensionality  $d$ . This indicates that as the dimension increases, the likelihood test becomes fundamentally less effective at separating normal and abnormal samples.*

*Proof.* By Zhang et al. (2021), AUROC of likelihood test is defined by

$$\text{AUROC} = \Pr(\log p_\theta(X) > \log p_\theta(Y)), X \sim P, Y \sim Q \quad (29)$$

Let  $\mu = \mathbb{E}_{X \sim P, Y \sim Q}[\log p_\theta(Y) - \log p_\theta(X)] > 0$ . Then we can derive:

$$\begin{aligned} 1 - \text{AUROC} &= \Pr(\log p_\theta(X) < \log p_\theta(Y)) \\ &= \Pr(\log p_\theta(Y) - \log p_\theta(X) > 0) \\ &= \Pr(\mu - (\log p_\theta(Y) - \log p_\theta(X)) < \mu) \\ &\geq \Pr(|\mu - (\log p_\theta(Y) - \log p_\theta(X))| < \mu) \\ &\geq 1 - \frac{\mathbb{E}[|\log p_\theta(Y) - \log p_\theta(X) - \mu|^n]}{\mu^n} \quad (\because \text{polynomial Markov inequality}) \end{aligned} \quad (30)$$

So, AUROC bounded above:

$$\text{AUROC} \leq \frac{\mathbb{E}[|\log p_\theta(Y) - \log p_\theta(X) - \mu|^n]}{\mu^n} \quad (31)$$

Since we know from Corollary 5.5 that upper bound of  $-\mu = \mathbb{E}_{X \sim P, Y \sim Q}[\log p_\theta(X) - \log p_\theta(Y)]$  decreases linearly in  $d$ , we can derive the following inequality:

$$\begin{aligned} \mu &= \mathbb{E}_{X \sim P, Y \sim Q}[\log p_\theta(Y) - \log p_\theta(X)] \\ &\geq -d(\max_{i \in [d]} D_{KL}(q_i || p_i) + \mathbb{E}_{x_i \sim q_i}[-\log q_i(x_i)] - \mathbb{E}_{x_i \sim p_i}[-\log p_i(x_i)]) \\ &= d(\min_{i \in [d]} \mathbb{E}_{x_i \sim p_i}[-\log p_i(x_i)] - \mathbb{E}_{x_i \sim q_i}[-\log q_i(x_i)] - D_{KL}(q_i || p_i)) \\ &> 0 \end{aligned} \quad (32)$$

Then, we can obtain inequality below:<sup>4</sup>

$$\frac{1}{\mu^n} \leq \frac{1}{d^n(\min_{i \in [d]} \mathbb{E}_{x_i \sim p_i}[-\log p_i(x_i)] - \mathbb{E}_{x_i \sim q_i}[-\log q_i(x_i)] - D_{KL}(q_i || p_i))^n} \quad (33)$$

Therefore,  $\exists M \in \mathbb{R}$  such that

$$\begin{aligned} \text{AUROC} &\leq \frac{\mathbb{E}[|\log p_\theta(Y) - \log p_\theta(X) - \mu|^n]}{d^n(\min_{i \in [d]} \mathbb{E}_{x_i \sim p_i}[-\log p_i(x_i)] - \mathbb{E}_{x_i \sim q_i}[-\log q_i(x_i)] - D_{KL}(q_i || p_i))^n} \\ &= \frac{\mathcal{O}(d^k)}{d^n(\min_{i \in [d]} \mathbb{E}_{x_i \sim p_i}[-\log p_i(x_i)] - \mathbb{E}_{x_i \sim q_i}[-\log q_i(x_i)] - D_{KL}(q_i || p_i))^n} \\ &\leq \frac{d^{k-n}|M|}{(\min_{i \in [d]} \mathbb{E}_{x_i \sim p_i}[-\log p_i(x_i)] - \mathbb{E}_{x_i \sim q_i}[-\log q_i(x_i)] - D_{KL}(q_i || p_i))^n} \end{aligned} \quad (34)$$

Because  $k - n < 0$ , upper bound of AUROC is inversely proportional to dimension.  $\square$

We note that the assumption that absolute  $n$ -th central moment of  $\log p_\theta(Y) - \log p_\theta(X)$  is  $\mathcal{O}(d^k)$  such that  $k < n$  is not a strong assumption. For example,  $X$  and  $Y$  are isotropic Gaussian,  $\log p_\theta(X)$  is a form that adds a constant to a variable that follows a Chi-square distribution with  $d$  degrees of freedom. Then, the second central moment of Chi-square distribution with  $d$  degrees of freedom, so second moment of  $\log p_\theta(Y) - \log p_\theta(X)$  satisfies  $\mathcal{O}(d)$  ( $\because \text{Var}(X - Y) = \text{Var}(X) + \text{Var}(Y)$ ), and most distributions satisfy this condition. In this example, it is possible to satisfy the assumption of Corollary 5.6 because the variance increases less than  $\mathcal{O}(d^2)$  with respect to dimension. In addition, the assumption is satisfied if at least one of the  $n$ -th absolute central moments the growth is slower than  $\mathcal{O}(d^n)$ . Therefore, using this assumption does not impose many restrictions, since it is satisfied except in extreme cases (e.g., when a term in the distribution function includes  $d$ ).

## E. Ablation Study of Anomaly Detection

Table 8. Anomaly detection performance across various anomaly types for deep models.

Type	Metric	GOAD	DeepSVDD	NeutraLAD	ICL	MCM	DRL	NF-SLT
Local	AUROC	0.7297	0.9605	0.9664	0.9646	<b>0.9948</b>	0.9545	0.9919
	AUPRC	0.7922	0.9678	0.9702	0.9697	<b>0.9953</b>	0.9635	0.9926
Clustered	AUROC	<b>1</b>	<b>1</b>	0.9174	<b>1</b>	<b>1</b>	<b>1</b>	<b>1</b>
	AUPRC	<b>1</b>	<b>1</b>	0.8620	<b>1</b>	<b>1</b>	<b>1</b>	<b>1</b>
Global	AUROC	<b>1</b>	<b>1</b>	<b>1</b>	<b>1</b>	<b>1</b>	<b>1</b>	<b>1</b>
	AUPRC	<b>1</b>	<b>1</b>	<b>1</b>	<b>1</b>	<b>1</b>	<b>1</b>	<b>1</b>
Dependency	AUROC	0.9986	0.9960	0.9974	0.9997	0.9990	0.9997	<b>0.9999</b>
	AUPRC	0.9983	0.9953	0.9966	0.9996	0.9983	0.9997	<b>1</b>

We apply the protocol for generating four types of anomalies suggested in Han et al. (2022) to the real dataset Satellite to verify whether NF-SLT can detect various types of anomalies well. Descriptions of the four types of anomalies and how synthetic anomaly data were generated are as follows:

- **Local anomalies** are data points that significantly differ from others in their immediate surroundings. After generating normal data using Gaussian Mixture Model (GMM, Milligan (1985); Steinbuss & Böhm (2021)), local anomalies are generated by multiplying the covariance by the scaling factor  $\alpha = 5$ .
- **Global anomalies** are data points distributed widely across the space but remain distinctly separate from the normal data distribution. Normal data is created in the same way as when creating local anomalies, and global anomalies are sampled from uniform distribution  $\text{Unif}(\alpha \cdot \min(X^k), \alpha \cdot \max(X^k))$  with the scaling factor  $\alpha$  set to 1.1.  $X^k$  refers to the  $k$ -th feature and creates anomalies by adjusting the maximum and minimum boundary values of the feature.
- **Dependency anomalies** are data points that fail to conform to the usual relationships or dependencies observed in normal data. Create normal data by capturing the dependency between features of normal data using Vine Copula (Aas et al., 2009). By estimating the probability density function of each feature through Kernel Density Estimation (KDE, Hastie (2009)) and dependency anomalies with independent features are created.
- **Clustered anomalies** are groups of similar data points that collectively differ greatly from the normal data distribution. Normal data is created in the same way as when creating local anomalies, clustered anomalies are generated by multiplying the mean vector estimated through GMM by the scaling factor  $\alpha = 5$ .

The comparison models were tested using the seven deep models used as comparison models in the main experiment of the paper, and the performance was measured using AUROC and AUPRC. According to the results of Table 8, it can be confirmed that NF-SLT has the best detection performance among deep models in all anomaly types except for local anomaly types. In addition, since it shows performance next to MCM even for local anomaly types, the results verify the performance of NF-SLT in detecting various anomaly types.

Additionally, we evaluated NF-SLT on datasets with a significant categorical composition using simple preprocessing techniques (e.g., one-hot encoding). We conducted experiments on categorical-rich datasets from ADBench (InternetAds,

campaign, census) and ODDs (nsl-kdd; [Rayana \(2016\)](#)). For the ADBench datasets, the input data were scaled using RobustScaler from Scikit-learn for all models except NeuTraLAD, which was trained without feature scaling due to performance degradation observed when scaling was applied. For the nsl-kdd dataset, no feature scaling was applied for any model, except for DRL, which employed the StandardScaler in accordance with the preprocessing configuration of the official implementation. The results of this experiment are reported in Table 9, demonstrating that NF-SLT maintains strong performance even on datasets dominated by categorical features.

*Table 9.* AUROC on datasets with mostly categorical features. The number after the slash indicates the relative rank among the seven deep models.

Dataset	DeepSVDD	GOAD	NeuTraLAD	ICL	MCM	DRL	NF-SLT
InternetAds	0.6013 / 7	0.7356 / 5	0.7112 / 6	<b>0.8815 / 1</b>	0.7973 / 3	0.7603 / 4	0.8746 / 2
campaign	0.7929 / 3	0.2837 / 7	0.7814 / 4	0.6933 / 6	0.7987 / 2	0.7525 / 5	<b>0.8059 / 1</b>
census	0.6421 / 3	0.4140 / 6	0.4991 / 5	0.3917 / 7	<b>0.7478 / 1</b>	0.5646 / 4	0.7186 / 2
nsl-kdd	0.8951 / 5	0.9026 / 4	0.9374 / 3	0.8798 / 6	0.8757 / 7	0.9459 / 2	<b>0.9598 / 1</b>

We additionally conducted a data contamination sensitivity test for NF-SLT. For this experiment, we selected the annthyroid, cardio, and letter datasets from ADBench. NF-SLT was trained on datasets consisting primarily of normal samples with a small proportion of anomaly samples intentionally mixed into the training data. After training, anomaly detection was performed, and the resulting performance was evaluated using AUROC, which is reported in Table 10. In Table 10, the contamination ratio denotes the proportion of anomaly samples relative to the number of normal samples in the training set.

*Table 10.* Contamination sensitivity analysis of NF-SLT.

Contamination Ratio	annthyroid	cardio	letter
1%	0.9048	0.9032	0.9195
3%	0.8806	0.8797	0.9126
5%	0.8752	0.8621	0.9005

Despite a relatively high contamination level of up to 5%, the observed degradation in AUROC remained limited to approximately 2–4%. These results demonstrate that NF-SLT exhibits strong robustness to data contamination, maintaining stable anomaly detection performance even in the presence of non-negligible anomalous samples during training.

## F. Robustness of Intrinsic Dimension Estimator

We further assess the robustness of our intrinsic-dimension (ID) analysis along four axes: (i) estimator choice, (ii) sub-sampling, (iii) feature scaling, and (iv) categorical-feature handling.

**Alternative ID estimator beyond TwoNN and MLE** To evaluate estimator dependence, we additionally estimate intrinsic dimension using IPCA (Fan et al., 2010) and compare it with TwoNN and MLE on representative tabular datasets:

Table 11. ID estimates from an alternative estimator IPCA alongside TwoNN and MLE on representative tabular datasets.

Method	magicgamma	satellite	landsat	waveform	Wilt	annthyroid	breastw	cover	fault	fraud
TwoNN	7	15	14	17	5	3	4	3	5	4
MLE	5	9	11	16	4	3	4	4	5	8
IPCA	3	2	2	2	1	1	3	1	5	4

IPCA yields systematically smaller ID estimates than TwoNN/MLE, whereas TwoNN and MLE remain broadly consistent with each other. Since our analysis relies on qualitative ID trends rather than the absolute scale of a particular estimator, we use TwoNN as the primary estimator throughout the paper, with the cross-estimator agreement serving as supporting evidence.

**Robustness to sub-sampling** We next estimate ID using TwoNN under different sub-sampling ratios:

Table 12. Stability of TwoNN ID estimates under different sub-sampling ratios on representative tabular datasets.

Ratio	magicgamma	satellite	landsat	waveform	Wilt	annthyroid	breastw	fault
100%	7	15	14	17	5	3	4	5
90%	7	15	14	17	5	3	4	5
80%	7	14	14	17	5	3	4	5
50%	7	14	13	16	5	4	4	4

The estimated IDs remain nearly unchanged across ratios, indicating that TwoNN is stable under sub-sampling at the levels considered.

**Robustness to different feature scalings** We also examine the sensitivity of TwoNN ID estimates to standard feature scaling choices:

Table 13. Sensitivity of TwoNN ID estimates to common feature-scaling choices on representative tabular datasets.

Ratio	magicgamma	satellite	landsat	waveform	Wilt	annthyroid	breastw	fault
No Scaler	7	15	14	17	5	3	4	5
Standard Scaler	7	15	14	16	4	5	4	5
Minmax Scaler	7	15	14	17	4	4	5	4

TwoNN produces comparable ID estimates across scaling schemes, suggesting that our ID characterization is not driven by a particular normalization choice.

**Categorical variables and one-hot encoding** Finally, using the Credit Card Client dataset with categorical features from (Yeh & Lien, 2009), we compare label encoding (default) and one-hot encoding. TwoNN returns the same intrinsic dimension (ID = 6) under both preprocessing choices, indicating that the estimate is not sensitive to the categorical-feature encoding strategy.

Overall, these results suggest that the ID-based characterization used in the paper is stable across estimator choice, sub-sampling, feature scaling, and categorical preprocessing.

## G. Model Details and Hyperparameter Searching Space

Anomaly detection in tabular data has garnered significant attention due to its relevance in various real-world applications, such as fraud detection, medical diagnosis, etc. (Yin et al., 2024). Anomaly detection tasks often suffer from imbalance

problems; hence several unsupervised methods have been worked because they have the advantage of not having from this problem. The learning method of anomaly detection varies depending on the presence of a label; however, this section only introduces unsupervised methods that learn without having information about the label. Because existing approaches can be broadly categorized into shallow models and deep models, it is divided into two categories and explained in the corresponding sections.

**Shallow Models** Principal Component Analysis (PCA, [Wold et al. \(1987\)](#)) is a dimension reduction method that projects data to a lower dimension than the original using Singular Value Decomposition (SVD). This algorithm can also be utilized as an anomaly detection method by using the reconstruction error when the latent vector projected in low dimensions is reconstructed to the original data as an anomaly score ([Shyu et al., 2003](#)). The Local Outlier Factor (LOF, [\(Breunig et al., 2000\)](#)) is a method that adopts neighbors to determine anomaly scores from a local perspective. Isolation forest (IF, [\(Liu et al., 2008\)](#)) uses the concept that normal data is easier to isolate than outliers, one-class SVM(OCSVM, [\(Schölkopf et al., 1999\)](#)) determines the decision boundary by determining a support vector that can sufficiently explain the given training data well, and determines that data that exist outside this boundary are outliers. COPOD ([Li et al., 2020](#)) and ECOD ([Li et al., 2022](#)) are similar anomaly detection algorithms that utilizing the Empirical Cumulative Distribution Function (ECDF), and measure anomaly scores using the extremeness of input data under ECDF.

**Deep Models** DAGMM ([Zong et al., 2018](#)) utilizes a deep autoencoder to generate a low-dimensional representation and reconstruction error for each input data point, which is further fed into a Gaussian Mixture Model (GMM). DeepSVDD ([Ruff et al., 2018](#)) trains to bring the input data representation closer to the predefined center using a neural network, sets the boundary of the hypersphere and determines that data existing outside this are outliers. GOAD ([Bergman & Hoshen, 2020](#)) is a model that generalizes the transformation-based self-supervised method used in the image domain and applies it to the tabular domain. NeuTraLAD ([Qiu et al., 2021](#)) and ICL ([Shenkar & Wolf, 2022](#)) applied the contrastive learning method, one of the self-supervised methods, to the tabular domain to improve performance. DO2HSC ([Zhang et al., 2024](#)) improves the limitations of DeepSVDD with a hypersphere assumption through orthogonal projection and double hypersphere decision boundary. MCM ([Yin et al., 2024](#)) performs anomaly detection by extending the masking self-supervised method adopted in the NLP or image domain to the tabular domain. In addition, DO2HSC ([Zhang et al., 2024](#)) was excluded from the experiment because, after checking their implementation code, it was confirmed that the model uses the statistics of the test data when performing orthogonal projection, which was judged to be biased when compared to other models. NPT-AD ([Thimonier et al., 2024](#)) was excluded from the experiments due to its excessively long training time for high-dimensional datasets with numerous data points.

Additionally, we provide details of the 13 models we implemented and the hyperparameter search space for each of them. Because it is impractical to search over every possible hyperparameter, we selected a small set of hyperparameters that we consider important for each model. For each search space, we chose commonly used values, ran all hyperparameter combinations 10 times on the 47 tabular datasets from ADBench, and then selected the combination with the highest average AUROC across datasets as the representative setting for that model. In Table 14, we record the hyperparameter search space used in our experiments, and in Table 15, we record the optimal hyperparameter combination finally selected from the hyperparameter search space. In the description of the deep model where the implementation code resides, we only specify the hyperparameters we modified.

**PCA** We implemented PCA via the PyOD library, and chose `n_component_ratio` as the hyperparameter to explore. `n_component_ratio` is a hyperparameter for what percentage of the dimensionality of the original input data should be reduced.

**LOF** We implemented LOF via the PyOD library and chose  $N$  as the hyperparameter to explore.  $N$  is a hyperparameter for how many neighbors to consider.

**IF** We implemented IF via the PyOD library and chose  $N$  as the hyperparameter to explore.  $N$  is the hyperparameter for how many trees to ensemble.

**OCSVM** We have implemented OCSVM via the scikit-learn library and have chosen `kernel` as the hyperparameter to explore. `Kernel` is the hyperparameter for which function to choose as the kernel function of OCSVM.

**COPOD** We implemented COPOD via the PyOD library and did not set a hyperparameter searching space because the model is hyperparameter-free.

**ECOD** We implemented ECOD via the PyOD library and did not set a hyperparameter searching space because the model

is hyperparameter-free like COPOD.

**DAGMM** We ran DAGMM experiments based on the model implemented in <https://github.com/mperezcarrasco/PyTorch-DAGMM>. We set the batch size to 512, the epoch to 200. We chose  $n_{gmm}$ ,  $\lambda_{energy}$ , and  $\lambda_{cov}$  as hyperparameters to explore.  $n_{gmm}$  is the hyperparameter for how many Gaussian mixture components to assume,  $\lambda_{energy}$  is the weight of the sample energy term in the loss function, and  $\lambda_{cov}$  is the weight of the regularization term on the covariance to avoid the singularity problem. Additionally, we set the hyperparameters that we thought were important in DAGMM as follows, but got nearly the same performance from all combinations.

**DeepSVDD** We implemented DeepSVDD ourselves using A as a reference. First, we pretrain using Autoencoder for 100 epochs and define the average value of the latent vector obtained by encoding the train data using the corresponding encoder part as the center. Then, we implemented DeepSVDD by training the encoder for 200 epochs with the loss function of the MSE (Mean Squared Error) of the center. The encoder consists of 3 layers with the same hidden size, the batch size is 512, the learning rate is 1e-3, the optimizer is AdamW (Loshchilov & Hutter, 2019), activation function to ReLU, the weight decay is 1e-4, and the learning rate scheduler is CosineAnnealingWarmRestarts (Loshchilov & Hutter, 2017). We set learning rate and latent dimension as the hyperparameters to search for (latent dimension and hidden size are the same).

**GOAD** We ran GOAD experiments based on the model implemented in <https://github.com/lironber/GOAD>. We set the batch size to 512, the epoch to 200. We chose  $n_{rot}$ ,  $d_{latent}$ , and  $d_{out}$  as hyperparameters to explore.  $n_{rot}$  is a hyperparameter for how many transformations to perform, and  $d_{latent}$  and  $d_{out}$  represent the latent dimension and the dimension after transforming the input data, respectively.

**NeuTraLAD** We ran NeuTraLAD experiments based on the model implemented in <https://github.com/boschresearch/NeuTraL-AD>. We set the batch size to 512, the epoch to 200, number of transformation to 11. The hidden and latent dimensions were selected using the automatic dimension selection implemented in the implementation code. We chose  $n_{enclayer}$ ,  $n_{translayer}$ , and  $trans\_methods$  hyperparameters to explore.  $n_{enclayer}$  represents the number of encoder layers, and  $n_{translayer}$  represents the number of layers in the block that performs the transformation. Finally,  $trans\_method$  is a hyperparameter for how we want to perform the transformation.

**ICL** We ran ICL experiments based on author's official supplementary at [https://openreview.net/forum?id=\\_hszzbt46bT](https://openreview.net/forum?id=_hszzbt46bT). We set the batch size 512. We chose  $\tau$  and  $d_{latent}$  as hyperparameters to explore. Since earlystopping is implemented in the implementation code, epoch used 2000 as it was specified in the implementation code.  $\tau$  represents the softmax temperature,  $d_{latent}$  represents the latent dimension.

**MCM** We ran MCM experiments based on author's official supplementary at <https://openreview.net/forum?id=1NZJyEDxy4>. According to the paper, the authors tuned only  $\lambda$  and learning rate per dataset, so we set these two hyperparameters to explore.  $\lambda$  represent the weight of mask diversity loss.

**DRL** We ran DRL experiments based on author's official supplementary at <https://openreview.net/forum?id=CJnceDksRd>. We adopted the hyperparameters used in the loss function directly from the official implementation. In contrast, we tuned the architectural hyperparameters, including the number of predefined bases in the latent space ( $n_{basis}$ ), the number of encoder layers ( $n_{enclayer}$ ), and the dimensionality of the latent representation ( $d_{latent}$ ).

**NF-SLT** We implemented NICE based on <https://github.com/DakshIdnani/pytorch-nice>. The coupling layer block was set to 10, the epoch was set to 200, and the weight decay was set to 1e-4. The optimizer was AdamW, and the learning rate scheduler was CosineAnnealingWarmRestarts. The batch size was set to 512. The prior distribution of the latent vector was set to  $\mathcal{N}(0, I_d)$ , and then trained to minimize the negative log-likelihood over the training latent vector. Additionally, due to the implementation structure of the coupling layer, it cannot be implemented when an odd-dimensional vector is input, which was solved by simply adding a single zero padding. We chose learning rate,  $d_{latent}$ , and  $n_{layer}$  as hyperparameters to explore.  $d_{latent}$  represents the latent dimension of the coupling layer block, and  $n_{layer}$  represents the number of layers in the coupling layer block.

In addition, we quantify the hyperparameter sensitivity of NF-SLT by comparing the metrics in Table 20 (dataset-wise tuned) and Table 1 (globally tuned), and report their differences in Table 16. We adopt this benchmark-level comparison because deep models have heterogeneous hyperparameter search spaces (Table 14), which makes sensitivity analysis with respect to a common set of hyperparameters impractical. Under this setup, a larger AUROC difference indicates higher sensitivity, while negative changes in the average-rank index and fail-ratio index indicate a deterioration in relative performance. Table 16 shows that even when using the dataset-wise optimal configuration from Table 15, NF-SLT exhibits only a marginal AUROC

improvement relative to other methods, and its relative indices (average-rank and fail-ratio) in fact worsen.

Table 14. Hyperparameter search space for each model.  $\eta$  denotes the learning rate.

Model	Hyperparameter search space
PCA	$n_{\text{component\_ratio}} \in \{0.75, 0.8, 0.85, 0.9, 0.95\}$
LOF	$N \in \{1, 3, 5, 10, 20\}$
IF	$N \in \{30, 50, 100, 200, 400\}$
OCSVM	$\text{kernel} \in \{\text{linear}, \text{rbf}\}$
COPOD	None
ECOD	None
DAGMM	$n_{\text{gmm}} \in \{3, 4, 5\}$ $\lambda_{\text{energy}} \in \{0.1, 0.5, 1\}$ $\lambda_{\text{cov}} \in \{5e-3, 1e-2, 5e-2\}$
DeepSVDD	$\eta \in \{1e-4, 5e-4, 1e-3\}$ $d_{\text{latent}} \in \{64, 128, 256\}$
GOAD	$n_{\text{rot}} \in \{16, 32, 64\}$ $d_{\text{latent}} \in \{8, 16, 32\}$ $d_{\text{out}} \in \{4, 8, 16\}$
NeuTraLAD	$n_{\text{enclayer}} \in \{5, 6, 7\}$ $n_{\text{translayer}} \in \{2, 3, 4\}$ $\text{trans\_method} \in \{\text{mul}, \text{residual}\}$
ICL	$\tau \in \{1e-2, 1e-1, 1\}$ $d_{\text{latent}} \in \{100, 200, 300\}$
MCM	$\lambda \in \{1e-2, 1e-1, 1, 10\}$ $\eta \in \{1e-4, 5e-4, 1e-3, 5e-3, 1e-2\}$
DRL	$n_{\text{basis}} \in \{5, 9, 13\}$ $n_{\text{enclayer}} \in \{3, 4, 5\}$ $d_{\text{latent}} \in \{64, 128, 256\}$
NF-SLT	$\eta \in \{1e-4, 5e-3, 1e-3\}$ $d_{\text{latent}} \in \{64, 128, 256\}$ $n_{\text{layer}} \in \{2, 3, 4\}$

Table 15. Optimal hyperparameter combination for each model.

Model	Optimal hyperparameter
PCA	$n_{\text{component\_ratio}} = 0.8$
LOF	$N = 20$
IF	$N = 400$
OCSVM	<code>kernel = linear</code>
COPOD	None
ECOD	None
DAGMM	$n_{\text{gmm}} = 3$ $\lambda_{\text{energy}} = 0.1$ $\lambda_{\text{cov}} = 5e-3$
DeepSVDD	$\eta = 1e-4$ $d_{\text{latent}} = 256$
GOAD	$n_{\text{rot}} = 32$ $d_{\text{latent}} = 32$ $d_{\text{out}} = 4$
NeuTraLAD	$n_{\text{enclayer}} = 5$ $n_{\text{translayer}} = 3$ <code>trans_method = mul</code>
ICL	$\tau = 1e-1$ $d_{\text{latent}} = 300$
MCM	$\lambda = 0.1$ $\eta = 5e-3$
DRL	$n_{\text{basis}} = 9$ $n_{\text{enclayer}} = 3$ $d_{\text{latent}} = 256$
NF-SLT	$\eta = 1e-3$ $d_{\text{latent}} = 256$ $n_{\text{layer}} = 2$

*Table 16.* Hyperparameter sensitivity of deep models. The columns that represent differences represent the differences between the indicators in Table 20 and Table 1. If it is sensitive to changes in hyperparameters, there will be a large difference in performance when experiments are performed with the optimal hyperparameter combination in the hyperparameter searching space for each dataset, compared to when experiments are performed with the same hyperparameter combination for all datasets.

Method	AUROC Diff	Avg Rank Diff	Fail Ratio Diff
DeepSVDD	0.0366	-1.02	-0.21
GOAD	0.1124	-0.68	-0.04
NeuTraL AD	0.0310	-0.53	-0.06
ICL	0.0284	-0.40	-0.15
MCM	0.0302	-0.96	-0.04
DRL	0.0233	-0.32	-0.02
NF-SLT	<b>0.0116</b>	<b>0.15</b>	<b>0.04</b>

## H. Performance Comparison of NF-SLT Across Normalizing Flow Models

In this section, we set the flow model used for NF-SLT to RealNVP instead of NICE, and then compared the performance with NICE. RealNVP’s implementation method replaced by the additive coupling layer used in NICE with an affine coupling layer. We set the hyperparameters of RealNVP to be the same as those of NICE, which recorded the performance in Table 1, except for the learning rate. We set the learning rate to 1e-3, 5e-3, and 1e-4, and selected 5e-3, the learning rate that recorded the highest AUROC performance, to record the performance in Table 17. Table 17 shows that RealNVP underperformed on all metrics compared to NICE. From this, we can conclude that affine coupling layers, which have higher expressive power than additive coupling layers, are not effective in tabular anomaly detection.

In this section, we replace the flow model in NF-SLT with RealNVP instead of NICE and compare its performance to that of NICE. In RealNVP, the additive coupling layers used in NICE are replaced with affine coupling layers. We match the hyperparameters of RealNVP to those of NICE used in Table 1, except for the learning rate. We try learning rates of 1e-3, 5e-3, and 1e-4, and report in Table 17 the results for 5e-3, which yields the highest AUROC. Table 17 shows that RealNVP underperforms NICE on all metrics, suggesting that affine coupling layers, although more expressive than additive ones, do not necessarily provide an advantage for tabular anomaly detection.

We do not include the Glow architecture as an additional comparison model for the following reasons. The main components of Glow are Actnorm and permutations implemented via 1x1 convolutions. First, we do not use batch normalization in our NICE and RealNVP implementations, and Actnorm is primarily designed to address situations where large batch sizes are unavailable, so its benefits are limited in our setting. Second, in our preliminary experiments, applying 1x1 convolution permutations led to worse performance than RealNVP. For these reasons, we omit Glow from our main comparisons.

*Table 17.* Performance comparison between NICE and RealNVP

Model	AUROC $\uparrow$	AUPRC $\uparrow$	Avg. Rank $\downarrow$	Top2 Cum. Ratio $\uparrow$	Fail Ratio $\downarrow$
NICE	0.8575	0.6398	3.74	0.40	0.06
RealNVP	0.8480	0.6385	4.45	0.30	0.09

Surely, Draxler et al. (2024) showed that a volume-preserving model like NICE is not a universal approximator. However, the biased density estimation of NICE is not the reason for its strong performance (i.e., the architecture itself is not a universal approximator). This is evidenced by the fact that RealNVP generally performs better than most models, although it still performs worse than NICE. This can also be considered as a new research direction in the future, and researchers can determine the future research direction by relating the reason why the performance of NICE slightly decreases compared to RealNVP in the tabular domain despite its higher expressive power to the theoretical background of the flow model.

*Table 18.* Performance comparison between NICE and MAF

Model	Ionosphere	Lymphography	WPBC	thyroid	yeast	glass	pendigits
NICE	<b>0.9581</b>	0.9746	0.5051	<b>0.9840</b>	<b>0.4652</b>	<b>0.8867</b>	<b>0.9930</b>
MAF	0.8406	<b>0.9908</b>	<b>0.5070</b>	0.9752	0.4359	0.7677	0.9926

Additionally, we attempted to run anomaly detection experiments with Masked Autoregressive Flow (MAF, Papamakarios

et al. (2017)) on all datasets. However, due to numerical stability issues during MAF training, we were unable to obtain reliable convergence on every benchmark. We therefore report AUROC scores only on the seven datasets where MAF trained stably. Each AUROC value is the mean over 10 independent runs. All experiments followed exactly the same protocol as in our main paper, using a latent dimension of 128, a learning rate of 1e-4, a batch size of 100, and 10 coupling layers. Our implementation was based on the reference code from Stimper et al. (2023a). As shown in Table 18, NICE achieves higher AUROC than MAF on the majority of the tested datasets, supporting our observation that a more advanced or expressive architecture does not necessarily yield better anomaly detection performance in the tabular domain.

## I. Typicality Test Performance

Anomaly detection via the typicality test builds on the observation that normal data may occupy a small region in input space while still lying in a high-probability typical set (Nalisnick et al., 2019b). In this approach, we decide whether a given  $\mathbf{x} \in \mathbb{R}^d$  is anomalous based on whether it belongs to the  $(\epsilon, N)$ -typical set  $\mathcal{A}_\epsilon^N[p(\mathbf{x})]$ , where  $p(\mathbf{x})$  is a generative model trained on  $\mathbf{x}_{train} \in \mathcal{D}_{train}$ . Following Zhang et al. (2021), the anomaly score  $s$  is computed as in Equation 35.

$$s = \left| -\log p(\mathbf{x}) - \hat{H}_p \right| \text{ s.t. } \hat{H}_p = -\frac{1}{|\mathcal{D}_{train}|} \sum_{\mathbf{x} \in \mathcal{D}_{train}} \log p(\mathbf{x}) \quad (35)$$

To assess whether the typicality test provides any benefit in the tabular domain, where counterintuitive phenomena rarely occur, we applied the typicality test using the final selected hyperparameters of NF-SLT in Table 1 and report the results in Table 19.

Table 19. Performance comparison between SLT and the typicality test

Model	AUROC $\uparrow$	AUPRC $\uparrow$	Avg. Rank $\downarrow$	Top2 Cum. Ratio $\uparrow$	Fail Ratio $\downarrow$
SLT	0.8575	0.6398	3.74	0.40	0.06
Typicality Test	0.8184	0.6270	5.83	0.26	0.30

Table 19 shows that the typicality test yields lower values than the simple likelihood test on all aggregate performance metrics. For almost all datasets, the performance either changes little or degrades noticeably. The only exception is the “yeast” dataset, where the simple likelihood test fails, on which the AUROC of the typicality test improves by about 8%. Although this dataset does not satisfy our definition of a counterintuitive case, it illustrates that the typicality test can occasionally outperform simple likelihood testing on specific datasets.

## J. Additional Experiment Results

In this section, we reported the additional experimental results. Table 20 records the AUROC and AUPRC performance per-dataset optimal hyperparameter selection. Table 21 records the AUROC for the shallow model and Table 22 records the AUROC for the deep model. Table 23 shows the AUPRC for the shallow model and Table 24 shows the AUPRC for the deep model. Table 25 shows standard deviation of the AUROC for the shallow model and Table 26 shows standard deviation of the AUROC for the deep model.

Table 20. AUROC and AUPRC performance per-dataset optimal hyperparameter selection.

Method	AUROC $\uparrow$	AUPRC $\uparrow$	Avg. Rank $\downarrow$	Top2 Cum. Ratio $\uparrow$	Fail Ratio $\downarrow$
PCA	0.7752	0.5240	7.60	0.09	0.51
LOF	0.8447	0.5979	6.15	0.23	0.36
IF	0.8036	0.5099	6.85	0.17	0.36
OCSVM	0.6651	0.3895	10.51	0.04	0.77
COPOD	0.7471	0.4419	9.06	0.06	0.66
ECOD	0.7425	0.4530	9.45	0.04	0.70
DAGMM	0.6468	0.3473	12.19	0.00	0.96
DeepSVDD	0.8053	0.5840	6.72	0.15	0.28
GOAD	0.7210	0.5225	9.91	0.06	0.57
NeuTralAD	0.8391	0.6262	5.64	0.28	0.23
ICL	0.8492	0.6551	5.30	0.19	0.11
MCM	0.8166	0.5988	6.38	0.21	0.32
DRL	0.8596	0.6607	4.72	0.26	<b>0.06</b>
NF-SLT	<b>0.8691</b>	<b>0.6749</b>	<b>3.89</b>	<b>0.36</b>	0.11

Table 21. AUROC performance of shallow models.

Dataset	PCA	LOF	IF	OCSVM	COPOD	ECOD
ALOI	0.5494	0.7571	0.5418	0.5038	0.5153	0.5304
Cardiotocography	0.8285	0.7784	0.8150	0.7349	0.6625	0.7856
Hepatitis	0.8165	0.8249	0.7753	0.5905	0.7986	0.7473
InternetAds	0.7012	0.8975	0.4842	0.3755	0.6764	0.6770
Ionosphere	0.9059	0.9550	0.9141	0.5439	0.7975	0.7328
Lymphography	0.9923	0.9843	0.9979	0.8761	0.9986	0.9974
PageBlocks	0.9324	0.9667	0.9284	0.8506	0.8768	0.9149
Pima	0.7058	0.7083	0.7337	0.5874	0.6564	0.5965
SpamBase	0.8073	0.6875	0.8406	0.7484	0.6896	0.6578
Stamps	0.9255	0.9063	0.9312	0.8522	0.9290	0.8717
WBC	0.9936	0.9737	0.9970	0.9949	0.9959	0.9959
WDBC	0.9955	0.9959	0.9951	0.8539	0.9957	0.9748
WPBC	0.4914	0.5642	0.5136	0.5852	0.5116	0.4679
Waveform	0.6495	0.7558	0.7354	0.6529	0.7312	0.6019
Wilt	0.2959	0.9218	0.4776	0.9567	0.3440	0.3935
annthyroid	0.8071	0.8794	0.9151	0.7075	0.7756	0.7888
backdoor	0.6440	0.6941	0.7659	0.7588	0.7891	0.8459
breastw	0.9877	0.9561	0.9946	0.9921	0.9938	0.9904
campaign	0.7678	0.6713	0.7400	0.6838	0.7828	0.7695
cardio	0.9649	0.9088	0.9508	0.7003	0.9216	0.9348
celeba	0.7997	0.5231	0.7177	0.5923	0.7505	0.7569
census	0.7073	0.5954	0.6289	0.7198	0.6741	0.6596
cover	0.9595	0.9899	0.8597	0.6924	0.8840	0.9203
donors	0.8947	0.9888	0.9008	0.8762	0.8151	0.8886
fault	0.5463	0.7073	0.6593	0.4821	0.4557	0.4693
fraud	0.9537	0.8706	0.9502	0.9288	0.9475	0.9496
glass	0.7099	0.8423	0.8041	0.2892	0.7605	0.7136
http	0.9994	0.9405	0.9928	0.7980	0.9916	0.9786
landsat	0.4452	0.7768	0.6139	0.4463	0.4197	0.3670
letter	0.5388	0.8572	0.6419	0.4499	0.5592	0.5718
magicgamma	0.7032	0.8355	0.7749	0.8143	0.6814	0.6387
mammography	0.8983	0.8508	0.8806	0.6572	0.9056	0.9064
mnist	0.9060	0.7707	0.8735	0.7149	0.7763	0.7484
musk	1.0000	1.0000	0.9817	0.1856	0.9458	0.9555
optdigits	0.5740	0.9601	0.8448	0.7722	0.6819	0.6037
pendigits	0.9500	0.9968	0.9706	0.6706	0.9051	0.9274
satellite	0.6761	0.8614	0.8060	0.8220	0.6339	0.5836
satimage-2	0.9783	0.9958	0.9935	0.5883	0.9745	0.9649
shuttle	0.9932	0.9979	0.9967	0.9869	0.9945	0.9929
skin	0.6027	0.9384	0.8911	0.4353	0.4702	0.4881
smtp	0.8659	0.8541	0.9126	0.2851	0.9117	0.8801
speech	0.4687	0.8048	0.4689	0.5275	0.4901	0.4687
thyroid	0.9811	0.9344	0.9898	0.6363	0.9402	0.9777
vertebral	0.4698	0.5921	0.4401	0.3849	0.3515	0.4337
vowels	0.6781	0.9649	0.7857	0.3771	0.4955	0.5919
wine	0.9357	0.9620	0.9175	0.8058	0.8725	0.7415
yeast	0.4356	0.5004	0.4259	0.3535	0.3828	0.4447
Avg AUROC	0.7752	0.8447	0.8036	0.6562	0.7471	0.7425
Avg.Rank	7.13	6.11	6.23	10.34	8.40	8.74
Top1 Ratio	0.09	0.06	0.09	0.04	0.02	0.02
Top2 Ratio	0.06	0.11	0.11	0.02	0.09	0.04
Top1,2 Cum Ratio	0.15	0.17	0.19	0.06	0.11	0.06
Fail Ratio	0.45	0.26	0.21	0.77	0.57	0.68

Table 22. AUROC performance of deep models.

Dataset	DAGMM	DeepSVDD	GOAD	NeuTralAD	ICL	MCM	DRL	NF-SLT
ALOI	0.5024	0.5653	0.5319	0.5700	0.5892	0.4831	0.5858	0.5479
Cardiotocography	0.6067	0.6759	0.3689	0.7626	0.6221	0.5713	0.6862	0.7558
Hepatitis	0.6167	0.6844	0.6054	0.6516	0.6070	0.7985	0.7735	0.7475
InternetAds	0.5590	0.6013	0.7356	0.7112	0.8815	0.7973	0.7603	0.8746
Ionosphere	0.6580	0.9597	0.9459	0.9708	0.9556	0.9574	0.9660	0.9581
Lymphography	0.8643	0.9756	0.9847	0.9779	0.9624	0.9934	0.9847	0.9746
PageBlocks	0.7966	0.8866	0.9345	0.9803	0.9691	0.8828	0.9556	0.9656
Pima	0.5759	0.5899	0.4432	0.5414	0.6547	0.6891	0.7036	0.7219
SpamBase	0.5564	0.5074	0.3366	0.6406	0.8037	0.7379	0.8416	0.7724
Stamps	0.7417	0.8361	0.6627	0.8836	0.8122	0.8720	0.9037	0.9327
WBC	0.8804	0.9873	0.5576	0.8944	0.9696	0.9254	0.9751	0.9726
WDBC	0.8121	0.9932	0.7814	0.9970	0.9856	0.9680	0.9827	0.9785
WPBC	0.4724	0.4579	0.3565	0.4216	0.4328	0.5068	0.4876	0.5051
Waveform	0.5135	0.6609	0.4180	0.8186	0.6172	0.6641	0.7146	0.7357
Wilt	0.4790	0.6008	0.7298	0.7527	0.8043	0.8655	0.8486	0.9066
annthyroid	0.8361	0.7689	0.5206	0.6685	0.8732	0.8640	0.7896	0.9181
backdoor	0.4535	0.9473	0.2805	0.9456	0.9767	0.9222	0.9541	0.9343
breastw	0.8740	0.9825	0.8402	0.9505	0.9835	0.9900	0.9771	0.9842
campaign	0.5948	0.7929	0.2837	0.7814	0.6933	0.7987	0.7525	0.8059
cardio	0.6091	0.9139	0.5964	0.7367	0.8456	0.8093	0.8888	0.9174
celeba	0.5308	0.3604	0.5204	0.6888	0.4595	0.6400	0.7811	0.7340
census	0.4619	0.6421	0.4140	0.4991	0.3917	0.7478	0.5646	0.7186
cover	0.7412	0.6819	0.2571	0.9096	0.9859	0.8949	0.6940	0.9658
donors	0.6243	0.9970	0.4472	0.9985	0.9630	0.9987	0.9439	0.9990
fault	0.5491	0.7146	0.7028	0.7680	0.7991	0.5955	0.7564	0.7518
fraud	0.8141	0.9517	0.4119	0.9448	0.9524	0.8488	0.9533	0.9564
glass	0.5561	0.4046	0.4495	0.8305	0.9027	0.8783	0.9064	0.8867
http	0.9966	0.9996	0.7812	0.9380	0.9999	0.9925	0.9999	1.0000
landsat	0.4874	0.6759	0.6427	0.7582	0.7075	0.5724	0.7842	0.6543
letter	0.5177	0.7565	0.6528	0.8227	0.9312	0.3674	0.9040	0.9258
magicgamma	0.6099	0.7267	0.5677	0.7317	0.7453	0.8143	0.8307	0.8863
mammography	0.5903	0.7263	0.8477	0.6377	0.8108	0.8321	0.8818	0.8761
mnist	0.6168	0.5940	0.7840	0.9700	0.8931	0.8631	0.8095	0.9015
musk	0.7128	0.9868	0.9999	1.0000	1.0000	0.9972	1.0000	1.0000
optdigits	0.4249	0.7386	0.2742	0.8566	0.8192	0.9279	0.9142	0.9205
pendigits	0.6830	0.9510	0.2513	0.9701	0.9619	0.9913	0.9689	0.9930
satellite	0.6913	0.8275	0.7789	0.8186	0.8190	0.8008	0.8902	0.8276
satimage-2	0.9234	0.9971	0.9960	0.9987	0.9974	0.9913	0.9957	0.9966
shuttle	0.6404	0.9980	0.3801	0.9994	0.9998	0.9979	0.9993	0.9984
skin	0.7063	0.7270	0.8856	0.9128	0.8954	0.8175	0.8827	0.9675
smtp	0.7976	0.8855	0.6588	0.8583	0.8805	0.9268	0.9124	0.9201
speech	0.5008	0.4688	0.5138	0.5123	0.5888	0.4110	0.5495	0.5795
thyroid	0.9408	0.9256	0.4299	0.9619	0.9653	0.9584	0.9523	0.9840
vertebral	0.4778	0.4794	0.5692	0.6381	0.5621	0.3544	0.5347	0.5483
vowels	0.5295	0.9377	0.9316	0.7861	0.9914	0.6873	0.9775	0.9852
wine	0.7212	0.9533	0.9430	0.9680	0.9575	0.4924	0.9415	0.9497
yeast	0.5442	0.6315	0.5979	0.5438	0.5574	0.4654	0.4431	0.4652
Avg AUROC	0.6467	0.7687	0.6086	0.8081	0.8208	0.7864	0.8363	0.8575
Avg.Rank	11.45	7.74	10.60	6.17	5.70	7.34	5.04	3.74
Top1 Ratio	0.00	0.02	0.00	0.19	0.17	0.06	0.11	0.21
Top2 Ratio	0.00	0.00	0.04	0.06	0.13	0.04	0.11	0.19
Top1,2 Cum. Ratio	0.00	0.02	0.04	0.26	0.30	0.11	0.21	0.40
Fail Ratio	0.89	0.49	0.62	0.30	0.26	0.36	0.09	0.06

Table 23. AUPRC performance of shallow models.

Dataset	PCA	LOF	IF	OCSVM	COPOD	ECOD
ALOI	0.0711	0.1334	0.0649	0.0592	0.0607	0.0637
Cardiotocography	0.7324	0.6321	0.7085	0.5931	0.5516	0.6598
Hepatitis	0.6398	0.6612	0.5448	0.4062	0.5783	0.4707
InternetAds	0.5689	0.7937	0.2782	0.2448	0.6206	0.6216
Ionosphere	0.9223	0.9609	0.9252	0.7024	0.7988	0.7743
Lymphography	0.8923	0.8121	0.9741	0.6735	0.9830	0.9717
PageBlocks	0.7340	0.8497	0.6965	0.7058	0.5254	0.6602
Pima	0.6961	0.6776	0.7268	0.6157	0.6852	0.6323
SpamBase	0.8427	0.7184	0.8696	0.8003	0.7039	0.6819
Stamps	0.5743	0.5235	0.5807	0.4142	0.5632	0.4716
WBC	0.9427	0.7288	0.9719	0.9510	0.9556	0.9556
WDBC	0.9110	0.8804	0.9002	0.4891	0.9283	0.6830
WPBC	0.3681	0.4122	0.3839	0.4560	0.3742	0.3492
Waveform	0.0861	0.2901	0.1132	0.1099	0.1047	0.0771
Wilt	0.0665	0.4182	0.0876	0.5389	0.0708	0.0799
annthyroid	0.5127	0.5591	0.6231	0.3465	0.2944	0.4058
backdoor	0.0783	0.0989	0.0942	0.1223	0.1275	0.1677
breastw	0.9832	0.9181	0.9944	0.9919	0.9936	0.9906
campaign	0.4878	0.3429	0.4645	0.3628	0.5141	0.4994
cardio	0.8454	0.6653	0.7977	0.3625	0.7103	0.7070
celeba	0.2083	0.0358	0.1306	0.0524	0.1656	0.1697
census	0.2012	0.1174	0.1403	0.2093	0.1610	0.1547
cover	0.1925	0.8391	0.0827	0.0534	0.1214	0.1865
donors	0.3618	0.7986	0.4125	0.3834	0.3353	0.4142
fault	0.5726	0.6218	0.6542	0.5049	0.4751	0.4906
fraud	0.2661	0.0287	0.2209	0.3929	0.3669	0.3339
glass	0.1791	0.2206	0.2177	0.0633	0.2001	0.2535
http	0.9156	0.1117	0.5033	0.4461	0.4636	0.2534
landsat	0.3169	0.6913	0.4300	0.3179	0.2977	0.2799
letter	0.1466	0.4482	0.1661	0.1108	0.1284	0.1432
magicgamma	0.7480	0.8612	0.8051	0.8429	0.7225	0.6807
mammography	0.4513	0.3563	0.3854	0.0753	0.5459	0.5516
mnist	0.6753	0.3479	0.5455	0.3116	0.3560	0.3045
musk	1.0000	0.9995	0.7037	0.2154	0.4869	0.6140
optdigits	0.0591	0.3212	0.1714	0.1326	0.0807	0.0650
pendigits	0.4162	0.8520	0.5394	0.0763	0.2930	0.3924
satellite	0.7711	0.8815	0.8455	0.8505	0.6957	0.6596
satimage-2	0.8823	0.9305	0.9371	0.1132	0.8349	0.7419
shuttle	0.9615	0.9784	0.9863	0.9732	0.9773	0.9474
skin	0.3585	0.7164	0.6368	0.3285	0.2958	0.3030
smtp	0.4636	0.4138	0.0088	0.0007	0.0081	0.5760
speech	0.0361	0.0440	0.0389	0.0404	0.0377	0.0385
thyroid	0.7791	0.6215	0.8265	0.3331	0.3077	0.6362
vertebral	0.1922	0.2003	0.1971	0.1892	0.1680	0.2015
vowels	0.1949	0.6011	0.2576	0.0839	0.0660	0.1421
wine	0.7044	0.7307	0.6605	0.5416	0.5629	0.3364
yeast	0.4707	0.5043	0.4787	0.4277	0.4696	0.4998
Avg AUPRC	0.5209	0.5606	0.5060	0.3833	0.4419	0.4530
Avg.Rank	7.45	6.34	6.66	10.11	9.00	8.98
Top1 Ratio	0.06	0.11	0.11	0.04	0.02	0.02
Top2 Ratio	0.04	0.09	0.06	0.02	0.09	0.04
Top1,2 Cum Ratio	0.11	0.19	0.17	0.06	0.11	0.06
Fail Ratio	0.45	0.28	0.32	0.74	0.62	0.62

Table 24. AUPRC performance of deep models.

Dataset	DAGMM	DeepSVDD	GOAD	NeuTralAD	ICL	MCM	DRL	NF-SLT
ALOI	0.0589	0.1186	0.0749	0.0937	0.1058	0.0578	0.1163	0.0831
Cardiotocography	0.4520	0.6307	0.3829	0.6679	0.5864	0.5245	0.6272	0.6742
Hepatitis	0.4622	0.5382	0.4831	0.3848	0.3773	0.5708	0.5664	0.5310
InternetAds	0.3792	0.4077	0.5967	0.4142	0.8345	0.7551	0.6564	0.8399
Ionosphere	0.7007	0.9702	0.9615	0.9761	0.9673	0.9705	0.9731	0.9676
Lymphography	0.5683	0.7607	0.8225	0.7839	0.7166	0.9187	0.8244	0.7691
PageBlocks	0.5661	0.7479	0.8474	0.9072	0.8890	0.6263	0.8532	0.8644
Pima	0.5831	0.6349	0.5237	0.5611	0.6805	0.6922	0.6713	0.7117
SpamBase	0.6143	0.6307	0.5289	0.6962	0.8289	0.7449	0.8710	0.8063
Stamps	0.3846	0.4953	0.3601	0.5896	0.4683	0.4703	0.5356	0.6273
WBC	0.6306	0.8947	0.1882	0.5681	0.7894	0.7778	0.8169	0.7923
WDBC	0.3081	0.8617	0.4889	0.9632	0.8215	0.7424	0.7713	0.6770
WPBC	0.3795	0.3655	0.3177	0.3349	0.3449	0.4092	0.3802	0.3727
Waveform	0.0607	0.1041	0.0460	0.2014	0.1301	0.1196	0.3720	0.1743
Wilt	0.1019	0.1150	0.2689	0.2147	0.3039	0.3129	0.4195	0.3903
annthyroid	0.5478	0.4005	0.3897	0.3503	0.5520	0.5679	0.4093	0.6227
backdoor	0.0461	0.6203	0.0527	0.9027	0.8968	0.3615	0.8937	0.5688
breastw	0.8930	0.9821	0.8605	0.9442	0.9790	0.9887	0.9692	0.9797
campaign	0.2771	0.5130	0.1368	0.5227	0.4218	0.5070	0.4510	0.5213
cardio	0.2816	0.7979	0.4940	0.4121	0.6640	0.6778	0.7576	0.7557
celeba	0.0548	0.0317	0.0426	0.0887	0.0400	0.0663	0.1256	0.0955
census	0.1036	0.1589	0.0909	0.1163	0.0898	0.2249	0.1368	0.2084
cover	0.0998	0.0483	0.0120	0.4044	0.7338	0.4159	0.0401	0.7204
donors	0.1729	0.9754	0.0994	0.9853	0.7310	0.9783	0.5842	0.9879
fault	0.5743	0.7123	0.7061	0.7222	0.7884	0.6307	0.7388	0.7412
fraud	0.0515	0.7615	0.1315	0.6194	0.6445	0.6662	0.6138	0.7082
glass	0.1362	0.1954	0.1929	0.2957	0.4677	0.4202	0.3840	0.3655
http	0.7535	0.9956	0.3368	0.8768	0.9894	0.5124	0.9846	0.9917
landsat	0.3407	0.5269	0.3988	0.5465	0.6609	0.3967	0.5849	0.4795
letter	0.1360	0.2934	0.2592	0.3964	0.6395	0.0893	0.6073	0.6673
magicgamma	0.6468	0.7545	0.6289	0.7665	0.8042	0.8549	0.8631	0.9094
mammography	0.0888	0.0964	0.3818	0.1382	0.3841	0.3291	0.5107	0.3885
mnist	0.2500	0.2424	0.5855	0.8695	0.6798	0.5856	0.5094	0.7080
musk	0.3674	0.7550	0.9980	1.0000	1.0000	0.9918	1.0000	1.0000
optdigits	0.0485	0.1621	0.0360	0.2009	0.1563	0.2755	0.3410	0.2725
pendigits	0.1507	0.3583	0.0283	0.5856	0.6152	0.8148	0.6390	0.8073
satellite	0.7369	0.8576	0.7973	0.8667	0.8632	0.8446	0.8943	0.8658
satimage-2	0.4356	0.9706	0.9641	0.9735	0.9586	0.8117	0.9284	0.8984
shuttle	0.2613	0.9818	0.2937	0.9944	0.9972	0.9608	0.9868	0.9695
skin	0.5066	0.4875	0.6741	0.7835	0.6725	0.5557	0.7323	0.9226
smtp	0.1050	0.6110	0.2985	0.4615	0.5455	0.3936	0.6302	0.4675
speech	0.0409	0.0312	0.0395	0.0362	0.0507	0.0316	0.0432	0.0529
thyroid	0.6545	0.6129	0.2536	0.6164	0.5694	0.6664	0.6526	0.7108
vertebral	0.2437	0.2224	0.2879	0.3645	0.3090	0.1731	0.2733	0.2617
vowels	0.0798	0.5534	0.6197	0.1764	0.9254	0.1425	0.8255	0.8755
wine	0.4028	0.7368	0.7695	0.8384	0.7650	0.1736	0.7375	0.7601
yeast	0.5627	0.5992	0.5863	0.5513	0.5573	0.4973	0.4796	0.5052
Avg AUPRC	0.3468	0.5388	0.4114	0.5694	0.6170	0.5383	0.6124	0.6398
Avg. Rank	11.28	7.23	9.98	5.96	5.72	7.17	4.87	4.15
Top1 Ratio	0.00	0.06	0.00	0.21	0.09	0.02	0.11	0.17
Top2 Ratio	0.00	0.09	0.04	0.09	0.17	0.04	0.06	0.17
Top1,2 Cum Ratio	0.00	0.15	0.04	0.30	0.26	0.06	0.17	0.34
Fail Ratio	0.85	0.40	0.60	0.32	0.26	0.38	0.11	0.06

Table 25. Standard deviation of the AUROC for shallow models.

Dataset	PCA	LOF	IF	OCSVM	COPOD	ECOD
ALOI	0.0012	0.0031	0.0025	0.0007	0.0009	0.0008
Cardiotocography	0.0055	0.0208	0.0114	0.0106	0.0046	0.0051
Hepatitis	0.0137	0.0284	0.0341	0.0431	0.0275	0.0373
InternetAds	0.0334	0.0070	0.0526	0.0094	0.0045	0.0044
Ionosphere	0.0153	0.0106	0.0162	0.0667	0.0217	0.0161
Lymphography	0.0061	0.0072	0.0036	0.1011	0.0028	0.0031
PageBlocks	0.0032	0.0037	0.0030	0.0346	0.0032	0.0026
Pima	0.0143	0.0119	0.0147	0.0381	0.0151	0.0163
SpamBase	0.0079	0.0183	0.0063	0.0126	0.0062	0.0060
Stamps	0.0251	0.0237	0.0210	0.0500	0.0159	0.0175
WBC	0.0034	0.0074	0.0015	0.0014	0.0023	0.0023
WDBC	0.0038	0.0036	0.0035	0.1023	0.0020	0.0042
WPBC	0.0319	0.0283	0.0371	0.0563	0.0332	0.0323
Waveform	0.0043	0.0116	0.0082	0.1012	0.0057	0.0067
Wilt	0.0508	0.0070	0.0154	0.0069	0.0029	0.0033
anmthyroid	0.0192	0.0221	0.0078	0.0752	0.0024	0.0025
backdoor	0.0031	0.0268	0.0115	0.0013	0.0009	0.0009
breastw	0.0045	0.0080	0.0016	0.0021	0.0016	0.0019
campaign	0.0022	0.0058	0.0105	0.0029	0.0008	0.0008
cardio	0.0021	0.0083	0.0063	0.0175	0.0045	0.0041
celeba	0.0004	0.0040	0.0103	0.0008	0.0004	0.0005
census	0.0009	0.0025	0.0122	0.0009	0.0007	0.0007
cover	0.0003	0.0006	0.0107	0.0030	0.0004	0.0002
donors	0.0088	0.0006	0.0110	0.0182	0.0003	0.0002
fault	0.0186	0.0243	0.0151	0.0147	0.0059	0.0052
fraud	0.0003	0.0230	0.0013	0.0009	0.0001	0.0001
glass	0.0466	0.0287	0.0263	0.1472	0.0228	0.0248
http	0.0000	0.0060	0.0012	0.3882	0.0002	0.0003
landsat	0.0067	0.0056	0.0121	0.0139	0.0061	0.0049
letter	0.0062	0.0082	0.0148	0.0167	0.0106	0.0096
magicgamma	0.0019	0.0026	0.0054	0.0015	0.0025	0.0025
mammography	0.0046	0.0143	0.0025	0.0134	0.0012	0.0012
mnist	0.0027	0.0160	0.0051	0.0109	0.0016	0.0019
musk	0.0000	0.0000	0.0126	0.0000	0.0026	0.0021
optdigits	0.0089	0.0077	0.0188	0.0124	0.0028	0.0028
pendigits	0.0025	0.0015	0.0037	0.0137	0.0029	0.0023
satellite	0.0022	0.0051	0.0082	0.0296	0.0033	0.0026
satimage-2	0.0004	0.0008	0.0007	0.1826	0.0006	0.0009
shuttle	0.0006	0.0005	0.0002	0.0013	0.0001	0.0001
skin	0.0006	0.0048	0.0029	0.2456	0.0007	0.0008
smtp	0.0421	0.0454	0.0019	0.0136	0.0005	0.0003
speech	0.0042	0.0036	0.0075	0.0368	0.0052	0.0044
thyroid	0.0012	0.0130	0.0015	0.2706	0.0023	0.0012
vertebral	0.0315	0.0250	0.0453	0.0832	0.0189	0.0209
vowels	0.0268	0.0039	0.0174	0.1791	0.0068	0.0073
wine	0.0196	0.0184	0.0336	0.1725	0.0100	0.0095
yeast	0.0177	0.0130	0.0125	0.0116	0.0098	0.0102

Table 26. Standard Deviation of the AUROC for deep Models

Dataset	DAGMM	DeepSVDD	GOAD	NeuTralAD	ICL	MCM	DRL	NF-SLT
ALOI	0.0182	0.0085	0.0030	0.0096	0.0158	0.0063	0.0131	0.0017
Cardiotocography	0.0939	0.0109	0.0144	0.0157	0.0314	0.0141	0.0336	0.0169
Hepatitis	0.0835	0.0753	0.0582	0.0815	0.0963	0.0200	0.0664	0.0787
InternetAds	0.0430	0.0213	0.0442	0.0179	0.0150	0.0013	0.0181	0.0114
Ionosphere	0.0788	0.0075	0.0164	0.0054	0.0082	0.0011	0.0072	0.0085
Lymphography	0.1437	0.0111	0.0087	0.0210	0.0150	0.0020	0.0099	0.0120
PageBlocks	0.0454	0.0105	0.0123	0.0044	0.0049	0.0056	0.0204	0.0027
Pima	0.0464	0.0191	0.0349	0.0311	0.0203	0.0131	0.0136	0.0163
SpamBase	0.0646	0.0191	0.0228	0.0157	0.0232	0.0055	0.0172	0.0200
Stamps	0.1480	0.0776	0.1259	0.0495	0.0875	0.0089	0.0225	0.0243
WBC	0.0968	0.0047	0.1129	0.0460	0.0142	0.0091	0.0106	0.0118
WDBC	0.1513	0.0031	0.1144	0.0027	0.0095	0.0095	0.0123	0.0107
WPBC	0.0589	0.0314	0.0347	0.0475	0.0217	0.0144	0.0508	0.0270
Waveform	0.0560	0.0173	0.0395	0.0061	0.0186	0.0213	0.0814	0.0224
Wilt	0.1216	0.0185	0.0418	0.1231	0.0649	0.0185	0.0265	0.0140
annthyroid	0.1246	0.0202	0.0940	0.0251	0.0332	0.0090	0.0251	0.0097
backdoor	0.1457	0.0035	0.0149	0.0050	0.0044	0.0070	0.0142	0.0070
breastw	0.0886	0.0049	0.1070	0.0260	0.0041	0.0019	0.0079	0.0033
campaign	0.0401	0.0283	0.0628	0.0134	0.0157	0.0028	0.0288	0.0024
cardio	0.1023	0.0114	0.0385	0.0518	0.0326	0.0123	0.0221	0.0102
celeba	0.0658	0.0786	0.0742	0.0140	0.0869	0.0349	0.0344	0.0284
census	0.0499	0.0463	0.0455	0.0064	0.0146	0.0034	0.0882	0.0094
cover	0.1598	0.0197	0.0697	0.1051	0.0051	0.0187	0.0286	0.0067
donors	0.1132	0.0025	0.0824	0.0023	0.0398	0.0004	0.0473	0.0010
fault	0.0606	0.0136	0.0299	0.0160	0.0104	0.0084	0.0086	0.0167
fraud	0.0656	0.0045	0.1054	0.0069	0.0024	0.0110	0.0088	0.0011
glass	0.1455	0.0382	0.0865	0.0594	0.0378	0.0161	0.0194	0.0532
http	0.0029	0.0002	0.3625	0.1784	0.0001	0.0030	0.0001	0.0000
landsat	0.0855	0.0105	0.0193	0.0085	0.0054	0.0058	0.0259	0.0127
letter	0.0548	0.0087	0.0121	0.0143	0.0102	0.0038	0.0248	0.0083
magicgamma	0.0627	0.0049	0.0233	0.0148	0.0177	0.0035	0.0157	0.0027
mammography	0.1788	0.0139	0.0181	0.0321	0.0435	0.0059	0.0094	0.0067
mnist	0.0637	0.0095	0.0318	0.0022	0.0103	0.0277	0.0592	0.0042
musk	0.2378	0.0046	0.0002	0.0000	0.0000	0.0005	0.0000	0.0000
optdigits	0.1469	0.0255	0.0434	0.0225	0.0681	0.0091	0.0701	0.0147
pendigits	0.1647	0.0104	0.0807	0.0124	0.0541	0.0029	0.0235	0.0034
satellite	0.0745	0.0044	0.0185	0.0030	0.0032	0.0022	0.0074	0.0034
satimage-2	0.0296	0.0004	0.0012	0.0002	0.0008	0.0026	0.0020	0.0009
shuttle	0.2304	0.0003	0.0570	0.0004	0.0001	0.0005	0.0003	0.0009
skin	0.1689	0.0095	0.0143	0.0220	0.0509	0.0215	0.0124	0.0113
smtp	0.0649	0.0039	0.0525	0.0584	0.0185	0.0195	0.0070	0.0108
speech	0.0241	0.0221	0.0375	0.0467	0.0387	0.0057	0.0399	0.0228
thyroid	0.0434	0.0132	0.1317	0.0121	0.0075	0.0038	0.0101	0.0028
vertebral	0.0745	0.0316	0.0817	0.1008	0.0590	0.0471	0.0576	0.0484
vowels	0.0895	0.0066	0.0149	0.0502	0.0055	0.0510	0.0119	0.0049
wine	0.2031	0.0288	0.0493	0.0223	0.0264	0.0693	0.0482	0.0544
yeast	0.0241	0.0219	0.0217	0.0190	0.0179	0.0124	0.0283	0.0150